Thomas Grehl

Improvement in TOF-SIMS Instrumentation for Analytical Application and Fundamental Research

2003

Experimentelle Physik

Improvements in TOF-SIMS Instrumentation for Analytical Application and Fundamental Research

Inaugural-Dissertation
zur Erlangung des Doktorgrades
der Naturwissenschaften im Fachbereich Physik
der Mathematisch-Naturwissenschaftlichen Fakultät
der Westfälischen-Wilhelms Universität Münster

vorgelegt von
Thomas Grehl
aus Delmenhorst

– 2003 –

Dekan: Prof. Dr. H. Zacharias
Erster Gutachter: Prof. Dr. A. Benninghoven
Zweiter Gutachter: Prof. Dr. H. F. Arlinghaus
Tag der mündlichen Prüfungen: 10. + 14. 4. 2003
Tag der Promotion: 14. 4. 2003

Table of Contents

1 Introduction

Currently, nano-technology is one of the most active areas of applied academic and industrial research, documenting the ongoing trend to sub-µm scale technology. In the last decade, structures of this size have been mainly produced for semiconductor devices. But in recent years, also flat panel (LC[1]/TFT[2]-) displays, MEMS[3], magnetic media, innovative coatings etc. have been developed with smaller and thinner devices and layers with increasing demand for reproducibility, reliability, high production yield and reduced cost. Apart from production, the understanding of small-scale devices and thin layer systems, in particular the influence of the chemical composition on their physical and chemical properties, is of strong interest.

In all stages of research, development, production and quality control, the analysis of µm areas and volumes is mandatory. This includes topography (AFM[4], STM[5]), structure (SEM[6], FIB[7]) and local chemical composition with (EDX[8], AES[9], XPS[10]).

In many respects TOF-SIMS is a complementary technique to the ones mentioned above: It gives elemental and molecular information from surfaces with sub-µm lateral resolution. Its ability to acquire this chemical information as well as its surface sensitivity is unrivaled, and together with depth profiling capabilities it can also analyze the depth distribution of elements with sub-nm depth resolution. The ability to gather a large amount of information has made it a widely and successfully applied technique in a broad range of industry and

---

[1] LCD: Liquid crystal
[2] TFT: Thin film transistor
[3] MEMS: Micro electro-mechanical systems
[4] AFM: Atomic force microscopy
[5] STM: Scanning tunneling microscopy
[6] SEM: Scanning electron microscopy
[7] FIB: Focussed ion beam
[8] EDX: Energy dispersive X-ray analysis
[9] AES: Auger electron spectroscopy
[10] XPS: X-ray photoelectron spectroscopy

research laboratories, both in analytical applications as well as in basic and applied research.

Sputter depth profiling of thin layers with high depth resolution requires very low sputter energies. When this work was started, TOF-SIMS depth profiling – especially in the energy range below 500 eV – was strongly limited by the weak performance of the sputter ion guns, which were usually operated in the 1 – 10 keV range. For the application of MCs^+ cluster profiling, even at 500 eV the Cs surface concentration became too high and caused an unacceptable sensitivity loss, rendering it impossible to further decrease the energy without any means of reduction in Cs surface concentration. Both the low sputter current and the limited repetition rate of the analysis gun in dual beam mode led to time consuming measurements that were not practical on a routine basis.

A strong compromise in imaging of molecular distribution with TOF-SIMS was the trade-off between lateral resolution (possible only with liquid metal ion sources) and molecular sensitivity (employing molecular primary ions like SF_5^+), while users were demanding a combination of these capabilities.

In order to extend the usefulness of the technique and to overcome existing limitations of TOF-SIMS instrumentation for both areas – basic research and analytical applications – some of these limitations have been addressed and overcome during this work. While doing this, it has been considered important not to take care of individual subjects and compromise others, but to solve several problems simultaneously. One example is the optimization of sputter and analysis gun for depth profiling, which consists of several individual improvements which together have proved beneficial.

In basic research, several subjects are currently under investigation and urgently request for improvements in the instrumentation. A very important issue is the understanding of the ion formation process mainly for – but not limited to – SIMS. For example, the formation of MCs^+ clusters is strongly influenced by the Cs surface concentration. Being able to vary it while keeping all other experimental parameters constant will allow deeper insight into ion formation. Another concern is the atomic mixing at extremely low sputter energies, as well as the concurrent mixing by two beams of different energies (sputter and analysis beam in the dual beam mode). This topic can only be investigated with improved ion guns, e. g. with respect to higher beam currents at lower energies, and different ion species such as Au cluster ions.

Progress in analytical applications, especially in depth profiling and 3D micro analysis, molecular mapping and quantification of depth profiles requires challenging instrumental developments: Increase in the speed of analysis by higher sputter currents and repetition rates while reducing the sputter energy to further increase the depth resolution, the use of Au cluster ions to enhance the sensitivity for molecular species while maintaining the sub-µm lateral resolution of the primary ion gun, or the adjustment of the Cs surface concentration by Cs-Xe co-sputtering over a wide range independently from the sputter energy and angle for optimized MCs^+ emission.

The first part of results (chapter 4) of this work deals with the instrumental developments that were necessary to improve the usability of TOF-SIMS for analytical applications and fundamental research. In the second part (chapter 5), the improvements are applied to some of the issues mentioned above. Each individual subject has a high level of complexity, so the investigations described here do not cover all possible aspects, but focus on some important facets of each topic.

2 Sputtering and Secondary Ion Emission

The essentials of sputtering and secondary ion formation are the basis of the understanding of the more fundamental experiments and results, which are going to be presented in chapter 5, and the motivation for some of the developments described in chapter 4. Therefore, a brief introduction to this field will be given in the first two sections of this chapter. A more comprehensive discussion and experimental data can be found in [1, 2, 3, 4, 5, 6].

In section 2.3, an explanation of the concept of sputter depth profiling and the quantification of the data will conclude this general chapter, leading to the more (TOF-)SIMS specific topics.

2.1 Sputtering

The elemental process of every ion-solid interaction is the sputter process, the removal of target atoms, resulting from the energy transfer from the ion impinging on the surface to the bulk of the material. The energy – at least in the energy range from a few 100 up to 10.000 eV – is mainly transferred via nuclear interactions. The interaction of the primary ions with the electrons of the solid is comparatively weak. When a primary ion strikes the surface of a solid, it transfers energy to the first atom which is hit. The amount of energy and momentum transferred is depending on the angle of incidence and mass ratio of ion and atom. After the interaction, both ion and the first target atom hit (*primary recoil*) will interact with more atoms, leading to the development of the so called collision cascade.

During the collision cascade, the primary ion looses its energy completely and stops somewhere in the material. The average distance the ions travel within the substrate is called the *range*, which is the path length integrated over all directions. The length of this path projected on the direction of the incident ion is the *projected range* and is shorter than the path length due to the numerous deflections the primary ion undergoes until it comes to rest. The projected range is proportional to $E^{2/3}$ (E: ion energy) [3].

At the beginning of the collision cascade, the momentum of the moving particles is mainly in the general direction of the momentum of the incident ion. But due to many binary collisions taking place, some fraction of the momentum is also directed back to the surface. Some atoms or molecules at the surface will receive enough momentum pointing outwards to overcome the binding energy and leave the solid material (*sputtering*). The vast majority of the sputtered particles originate from the first very few monolayers, resulting in an information or sampling depth for subsequent analysis of the sputtered material of below 1 nm.

The development of the collision cascade into a series of displacements greatly changes the constitution of the material. The crystal structure is locally destroyed (amorphization), and the movement of primary and higher recoils in the upper monolayers changes the chemical composition of the target (*atomic mixing*). Even in pure materials, the implantation of ions into the bulk changes the chemical composition. The sum of these effects has a strong impact on subsequent collision cascades and sputtering events, since the material properties (binding energy, distribution of different elements, density, etc.) change significantly. The zone where the material properties are changed by amorphization and atomic mixing is called the *altered layer*, and its depth is correlated to the component of the projected range vertical to the surface (*penetration depth*). Most authors define the depth of the altered layer as two times the projected range, but the boundary between altered layer and unmodified target material is indistinct and the angle of primary ion incidence has to be considered as well.

The number of sputtered particles per incident ion is defined as the *sputter yield* Y_{sp}. The total sputter yield Y_{tot} is the sum of the sputter yields Y_i of individual species, which can differ according to e. g. different mass and binding energy.

$$Y_{tot} = \sum_i Y_i$$

A universal model both for the value of the sputter yield itself as well as its angular dependence is still not available, but several semi-empirical models exist [7, 8], some of which are reaching a high complexity.

Below a threshold energy E_{th}, depending both on target material and bombardment conditions, sputtering does not occur, because the binding energy in the solid is higher than the energy transferred by the collision cascade. Above E_{th}, the sputter yield sharply rises and goes through a maximum at medium energies (some 10 keV). The energy dependence in a practical model valid for low energy sputtering as in SIMS is given by

$$Y(E) = Q \cdot S_n \cdot \left[1 - \left(\frac{E_{th}}{E}\right)^{2/3}\right] \cdot \left(1 - \frac{E_{th}}{E}\right)^2$$

where S_n is the dimensionless *nuclear stopping power* and Q a fitting parameter, combining physical properties which are difficult to measure and therefore summarized into one experimental parameter. Q is tabulated for many ion-target combinations [7, 9].

In general, the sputter yield increases with the angle of incidence[11] because the collision cascade and therefore the energy of the primary ion is deposited in a shallower layer. The most simple approach to describe the angular dependence is only valid for angles α up to about 45° and proposes an increase in sputter yield proportional to $\cos^{-b}\alpha$. The parameter b is in the range 1 – 2, depending on the atomic masses of ion and target atoms [3]. Between 60° and 80°, the sputter yield goes through a maximum and decreases rapidly towards zero at 90°. More sophisticated models are referenced in [3] and described by Yamamura [10]. For single crystals, the orientation relative to the crystallographic axes influences the sputter yield additionally to the angle of incidence.

If the partial sputter yields Y_i do not reflect the concentration of all species contained in the target material, the composition within the altered layer changes because of *preferential sputtering*. If for example species i has a high sputter yield, its concentration in the uppermost layer is lowered due to preferential sputtering. The depletion of species i reduces the chance of it being sputtered and therefore reduces its sputtered flux. The reduction in concentration continues until some reduced value of the surface concentration of species i. At this stationary state, the flux of sputtered atoms represents the composition of the bulk material and

$$\frac{Y_i}{Y_j} = \frac{c_i}{c_j},$$

where Y_i, Y_j are the partial sputter yields of any species i and j contained in the target, and c_i, c_j their concentrations.

---

[11] The angle of incidence is measured relative to the surface normal.

In the altered layer, a gradient exists for all species from the concentration caused by the preferential sputtering to the unchanged bulk concentration. This implies that also the chemical state of the surface can be modified by preferential sputtering, since e. g. oxygen is sputtered efficiently in many oxides, reducing the oxidation state of the surface.

Since each single ion hitting the surface randomly removes a few target atoms and the impact position of the ions are statistically distributed over the irradiated area, the removal of material is also a statistical process. Starting with a perfectly flat sample, the statistics of sputtering will introduce a certain surface topography, which on single crystals is extended over some monolayers. Together with the structural and chemical changes, this statistical roughness leads to a change in sputter yield during the formation of the altered layer [11, 12]

Additionally, under certain bombardment conditions and depending on the bombarded material, a sputter induced topography is formed that exceeds the statistical roughness. Often ripples with a period of some µm and a growing amplitude form perpendicular to the plane defined by the incoming beam and the surface normal. In general, the tendency of ripple formation increases with the angle of incidence of the ion beam. The onset of ripple formation is dose dependent and can change the sputter yield of the target significantly [3, 13, 14], since the surface binding energy and the angle of incidence, which are globally defined for flat surfaces, change locally.

Ripple formation is especially pronounced on polycrystalline targets, where the local crystal orientation is statistically distributed and therefore the sputter yield varies for each grain of the target. Depending on the angle of incidence and the primary ion species, the ripple amplitude can differ strongly. The only way to avoid roughness on polycrystalline targets at oblique incidence is to rotate the target during sputtering [15]. Sample rotation equals out the differences in sputter yield for different grains, because the average incidence angle is the same for grains of different orientation.

But not only polycrystalline materials tend to form ripples. Other effects, like local variations in sputter yield caused by small variations in the oxidation state during oxygen sputtering of Si [16, 17], can lead to ripple formation after a specific sputter dose. The critical dose can vary over orders of magnitude for different experimental set-ups and materials.

The depth over which all the changes of sputter yield (due to topography and amorphization) and chemical state of the surface take place is called the *transient width* (see also Fig. 2). Quantification of information obtained during the transient regime is generally difficult, since it is a non-equilibrium situation and many parameters are changing simultaneously.

2.2 Secondary Ion Formation

Sputtered particles emitted from a surface are mostly neutral, usually only a small fraction of less than one percent is in a charged state. This fraction, the ionization probability P_A of species *A*, is strongly dependent on the nature of the species. It varies over several orders of magnitude for different sputtered species from the same target.

Additionally, the chemical state of the surface causes variations of P_A over some orders of magnitude, even for the same combination of bombarding species and target material. This makes the prediction of the ionization probability impossible without the use of standard samples very similar to the target of interest. The strong dependence of the ionization probability on the chemical state of the emitting surface is named *matrix effect* [1].

The number of secondary ions of species *A* generated per primary ion is the secondary ion yield

$$Y(A) \propto Y_{sp} \cdot P_A \cdot c_A$$

proportional to the partial sputter yield Y_{sp} of the species, the ionization probability P_A and c_A, the surface concentration of *A*. Since for most instruments the transmission and the detection efficiency is not known as an absolute number, a parameter including this analyzer dependence is the useful yield $Y_u(A)$ defined as the number of secondary ions *detected* per sputtered particle. It describes the efficiency of the ion generation and detection. Only if sputter yield and ionization probability are constant, the yield is a measure for the concentration of a certain species at the surface (cf. 2.3.2).

If the target is bombarded with a high dose of chemically reactive ions, the implanted ions alter the state of the surface. This effect can be used to specifically influence the secondary ion yield of certain species. After the altered layer has been formed, the chemical state is defined and stabilized by the implanted reactive ions. Their concentration is dependent on the total sputter yield, because in steady state, the flux of sputter ions impinging on the surface must be compensated by the same amount of sputter ions leaving it. Only the implantation depth and the sputter rate determine the concentration of the reactive species in the altered layer. As a rule of thumb, their concentration is given by

$$c = \frac{1}{1 + Y_{sp}}$$

if sputtering is the only mechanism removing the implanted ions from the surface. Segregation towards the surface or into the bulk and evaporation/outgasing can significantly influence the surface concentration of the implanted ions.

It is well known [1] that the formation of negative secondary ions is greatly enhanced by the presence of Cs at the surface, while the yield of electropositive secondary ions is improved by oxidation of the surface. Oxidation can be achieved by oxygen bombardment and/or by oxygen flooding (increasing the partial pressure of oxygen within the analysis chamber).

In order to understand these enhancement effects, one has to consider some of the ionization models. Below, only the most common ones are briefly described [18, 19].

2.2.1 Electron Tunneling Model

Sputtering from metal surfaces and ionization of the sputtered particle can be considered as an interaction between the particle and the electron continuum (valence band) in the metal [20, 21]. During the removal of the particle, while it is still in the vicinity of the surface, the atomic levels of the sputtered atom overlap with the electronic levels of the metal. The Fermi Level E_F of the metal can be higher or lower than the atomic level after the sputtered atom has reached a minimum distance from the surface, and therefore an exchange of an electron is energetically possible (Fig. 1). The direction of the charge transfer is depending on the values of the work function Φ of the metal and the ionization potential I (or the electron affinity A, respectively) of the sputtered particle.

A potential barrier between the electronic states inhibits the charge transfer, but tunneling of the electron to the atom is possible with a probability that is exponentially dependent on the distance where the energy levels become equal (determined by the work function Φ of the metal) and on the normal component of the velocity v_n of the sputtered particle (determining the time for interaction). The ionization probability P for positive (P^+) and negative (P^-) ion formation can be described by

$$P^{\pm} \propto \exp\left(-\frac{2\Delta(z_c)}{\hbar \gamma v_n(z_c)}\right) \cdot \begin{cases} \exp\left(-\dfrac{I-\Phi}{\varepsilon_p}\right) & \text{tunneling of electron towards surface} \\ \exp\left(-\dfrac{\Phi-A}{\varepsilon_n}\right) & \text{tunneling of electron towards sputtered atom} \end{cases}$$

where $\Delta(z_c)$ is a function describing the broadening of the atomic level at the distance z_c, where the Fermi level crosses the atomic level E_a. $v_n(z_c)$ is the normal component of the velocity at distance z_c; ε_n, ε_p are proportional to the normal component of the velocity, and γ is a characteristic length parameter.

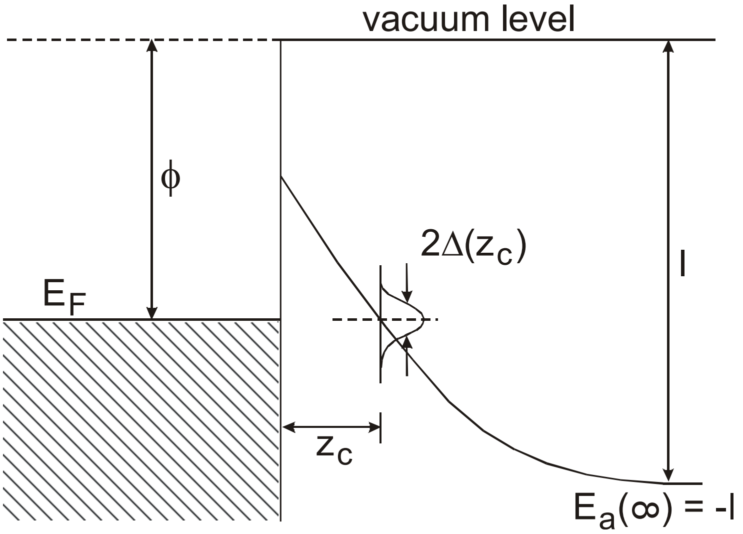

Fig. 1: Energy diagram of a particle leaving a metal surface (from [19]). At the distance z_c, the atomic level crosses the Fermi level of the metal and charge exchange is possible. The probability depends on the distance of the atom and the interaction period (or the velocity of the atom, respectively).

One way to make use of the exponential dependence of the ionization probability on the work function of the surface is to lower the work function as much as possible to enable charge transfer to the sputtered atom at low distances z_c. This increases the probability for negative ion generation by several orders of magnitude. It can be obtained by covering the surface with a submonolayer of Cs, e. g. from a Cs sputter ion gun performing a depth profile. From the formula for P^-, an exponential increase of the ionization probability with Cs surface concentration is expected. P^- levels off when all sputtered atoms are ionized or when the work function has reached its minimum value.

For the emission of positive ions, a low work function can be detrimental. If for example a positive ion is leaving the surface, the first unoccupied atomic level can be lower than the Fermi level, making an electron transfer from the surface to the ion possible, which re-neutralizes the emitted ion. This is illustrated by the Cs^+ intensity during Cs sputtering, which increases at low Cs coverage according to the increase in Cs concentration. As soon as the work function is lowered significantly, the Cs^+ intensity decreases again. At this stage, re-neutralization starts to overcompensate the increase in concentration and therefore sputtered Cs atoms [22, 23]. Typically, this is the case as soon as the work function is only about 0.5 eV higher than the ionization potential of Cs. Whether or not the decrease of the positive ionization probability is observed with increasing Cs coverage under Cs bombardment is depending on the sputter yield of the target material at the given energy and angle of incidence, which determines the maximum Cs concentration and hence the minimum work function.

2.2.2 Bond Breaking Model

For oxides (and halides), which are present on almost all elemental targets or can be formed by bombardment or chemisorption, the bond breaking model [24, 25] describes the ionization as a consequence from the breakup of an ionic or covalent bond. An electropositive atom leaving the surface is ionized by breaking its bond to another surface atom and leaving one electron behind.

A very concise discussion of this model is given in [3], including all fundamental references. The practical result of this discussion is an expected exponential decrease of the ionization probability with increasing ionization potential I. Electropositive elements in an oxide or halide environment will effectively be ionized by breaking the surface bonds, which is utilized when a surface is bombarded or flooded with oxygen to incorporate it into the altered layer. Thus the ionization probability for electropositive species is increased by up to three orders of magnitude [19]. Oxygen bombardment and/or oxygen flooding is extensively used for all kinds of materials. Unfortunately, the oxidation of the matrix can also have detrimental effects, like enhanced segregation either caused by the structural changes during sputtering or by the oxide formation [26, 27, 28]. Also changes in sputter yield depending on the degree of oxidation are observed [16, 17].

2.2.3 Recombination Model

In contrast to the two models described above, the recombination model is specifically valid for cluster ions of matrix species with one or two Cs atoms originating from the sputter beam. Basically, the model assumes the emission of Cs^+ ions together with sputtered neutrals M that (re)combine above the surface to form MCs^+ or MCs_2^+ cluster ions. The clusters may also be formed directly in the sputter process, since Cs^+ ions are also present at the surface [29].

Although the strong emission of these clusters has been known longer [30], their importance for some application like detection of rare gases [31] and the quantification of matrix compounds [32, 33] was recognized only about 15 years ago.

As already mentioned in 2.2.1, a surface covered with a submonolayer of Cs emits Cs^+ ions with a very high degree of ionization. This high degree of ionization is virtually independent of the matrix, since the work function is mainly defined by the Cs overlayer itself. Only if the Cs concentration becomes very high, the degree of ionization is reduced and becomes dependent on the surface concentration.

The composition of the flux of sputtered particles from the target is representative of the concentrations in the bulk as soon as the sputter equilibrium has been reached (cf. 2.1). The yield of cluster ions formed by combining Cs^+ ions with sputtered neutrals

$$Y_{MCs^+} \propto Y_{Cs^+} \cdot \underbrace{Y_{tot} \cdot c_M}_{Y_{M^o}} \cdot f_{MCs}$$

should therefore be independent of the chemical state of the surface. If at all, only a weak matrix effect is observed. Apart from f_{MCs} (the formation probability for the cluster ion), all factors are constant and rather well understood. For quantification purposes, the formation probability is assumed to be constant, and the yield Y_{MCs^+} divided by the Cs^+ intensity should be directly proportional to the concentration c_M of M.

2.3 Sputter Depth Profiling

Independent of the type of analyzer used, there are basic principles that hold true for all types of sputter depth profiling experiments [4, 5]. Consequently, they are also valid for depth profiles acquired with other analytical techniques like AES or XPS.

Principally, a sputter crater is formed by a beam of primary ions which is rastered over an area larger than the beam diameter. From the flat region in the center of the crater, either secondary ions (dynamic SIMS) or neutrals (SNMS[12]) emitted during sputtering or electrons/photons generated by a second probing beam are detected in order to gather information about the sample at the receding surface.

The different probing techniques collect complementary information about the sample, such as the elemental composition or the chemical state. Their *information depth*, the depth interval from which the information about the temporary surface originates, differs between < 1 nm to about 10 nm. This is strongly dependent on the type of signal used: Electrons (AES, XPS) have an escape depth of a few nm, while ions originate predominantly from the first monolayer, and the probability that an ion originates from the third monolayer is already negligible[13].

---

[12] SNMS: Secondary neutral mass spectrometry

[13] For XPS, the use of electrons with a high off-normal take-off angle decreases the escape depth measured perpendicular to the surface.

Identical for all sputter depth profiling techniques is the prerequisite of a flat crater bottom, with respect to both macroscopic curvature and to roughness on a micro scale. The information detected from the analyzed area is assigned to the depth of the crater, integrated over the crater bottom topography.

2.3.1 Depth Calibration

All sputter depth profiling techniques record the intensity of one or more signals versus the sputter time. Before these intensities can be quantified in terms of concentration, the time scale has to be converted into a depth scale. In most cases, a constant sputter rate S, typically measured in nm/s, is assumed to convert the sputter time t_{sp} into a depth z:

$$z = S \cdot t_{sp}$$

The sputter rate can be calculated from the known sputter yield under the specific conditions applied, the density of the target, the crater size and the sputter current. Alternatively, it is determined via a depth measurement of the crater. This measurement can either be accomplished by a surface profiler (optical or mechanical), or by an intrinsic marker in the sample like an interface of known depth. If different sputter rates are known for different layers, a multi-layer calibration can be applied, but the definition of the interfaces and the transition from one layer to the other is difficult.

Since the sputter yield can be significantly different (usually higher) during the formation of the altered layer compared to the bulk value, an apparent *shift* of the profile can result from the assumption of constant sputter rate [17]. This *surface shift* is more pronounced, the larger the fraction of the transient regime on the total depth of the sputter crater is. The deeper the crater is, the higher is the relative accuracy of the depth scale. Reducing the transient width e. g. by reducing the sputter energy or – for the case of Cs sputtering – by reducing the steady state Cs concentration on the surface is a means of reducing the shift of the profile.

If the sputter rate varies significantly during the depth profile, e. g. in a multilayer system, a constant sputter rate cannot be assumed. In this case, the depth scale has to be established in sections.

2.3.2 Concentration Calibration

Depth profiles acquired with SIMS are intensity profiles that have to be converted to concentration profiles. The intensity

$$I(A) = I_p \cdot Y_{tot} \cdot P(A) \cdot T \cdot D \cdot c_A$$

of species A is – besides its concentration c_A – dependent on the primary ion current I_p, total sputter yield Y_{tot}, ionization probability $P(A)$, transmission T and detection efficiency D of the instrument. As a result, absolute count rates are unreliable for concentration determination. Several of the factors mentioned above can change significantly with small variations in the instrumental setup. To overcome this, the intensity of an impurity is normalized to the intensity of a matrix signal at each point in depth (point-to-point normalization). Afterwards, it is scaled by a *relative sensitivity factor* (RSF) that has to be measured under identical experimental conditions using a standard sample of the same matrix-impurity combination. If MCs^+ or MCs_2^+ clusters are used, the intensity of the cluster ions are normalized to the Cs^+ or Cs_2^+ signals, respectively, to account for variations in sputter yield.

The RSF is – like the sputter rate – usually assumed to be constant throughout the whole profile. In multilayer samples this is not the case, but even in single layers the RSF changes within the transient region due to changes in oxidation state or Cs concentration. These changes lead, if the species of interest is located within the transient region, to errors in the concentration scale. Several attempts have been made to correct the profiles both for the sputter rate changes (giving rise to the surface shift) and for the changes in RSF especially for oxygen or noble gas sputtering [34, 16, 35, 36, 37]. In all cases, secondary ion signals are used to determine the oxidation state of the surface. By varying the oxidation state, and measuring sputter yield and RSF under these conditions, correction functions have been established. Unfortunately, all of these attempts are only applicable to particular sample systems (mostly Si), and up to now no way of correcting the sputter rate for varying Cs concentrations has been presented.

2.3.3 Depth Resolution and Response Function

The in-depth distribution of a substance measured during a depth profile does in most cases not represent the true distribution exactly. The measurement is a convolution of the true profile with a resolution function [38]. The resolution function can be calculated by deconvolution or measured directly by profiling an atomically sharp and thin layer (delta layer, Fig. 2) [39].

As a model function, a three parameter resolution function (a superposition of two exponentials with a gaussian) is widely accepted, defining the upslope λ_u, decay length λ_d and full width at half maximum (FWHM) σ. The MRI (mixing – roughness – information depth) model [40, 41] relates the parameters of the resolution function to physical properties of the sample and characteristics of the sputter process. The upslope is dominated by the information depth of the probing technique, which for SIMS can be assumed to be about one monolayer (0.4 nm). The width of the resolution function is correlated to the roughness of the surface, which can be either initial roughness or sputter induced topography (cf. 2.1). If the sputter conditions are chosen well, only the initial roughness of the sample occurs.

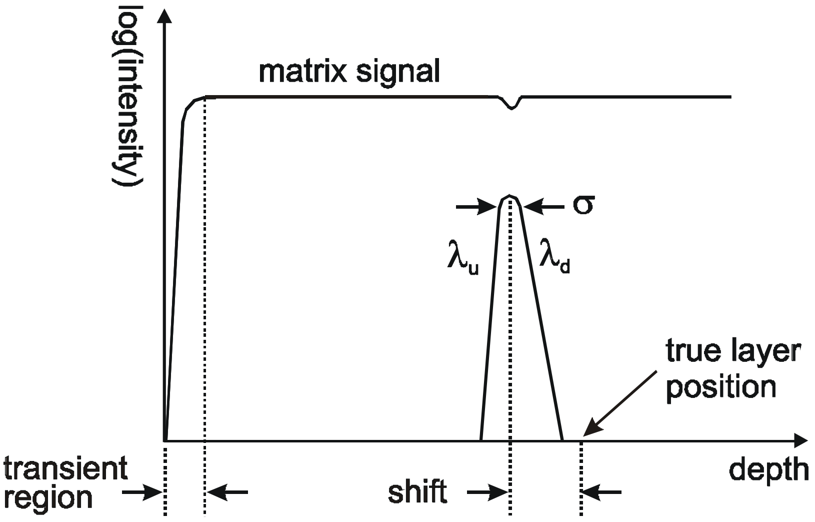

Fig. 2: Depth profile of a delta layer, illustrating the shape of the resolution function typically observed in SIMS depth profiling.

Different to other sputter profiling techniques, the width cannot be regarded as a good parameter for the depth resolution, because the dynamic range of SIMS is extremely high. The width of the resolution function at 50 % of the maximum intensity is not a measure for the width at 1 % or 0.1 %, so the FWHM cannot give a comprehensive number for the width of the profile with a dynamic range of several orders of magnitude. Therefore, the decay length, which additionally is the only parameter really available for optimization in SIMS, is widely accepted as a measure for the depth resolution. It is strongly dependent on sputter energy, sputter species and angle of incidence since it is associated to the atomic mixing. λ_d can be determined as the depth over which the intensity decays by a factor of 1/e when a delta structure or a sharp interface is profiled ($z_{1/e}$).

Some authors give numbers for the depth over which the intensity decays by a factor of ten ($z_{1/10}$),

$$\lambda_d = z_{1/e} = z_{1/10} / \ln 10 \approx z_{1/10} / 2.3$$

According to the sputter theory and experimental results, λ_d is related to the sputter energy by a power law:

$$\lambda_d = k \cdot E^S$$

The exponent S is in the range 0.15 – 0.85 [42, 16] measured for a variety of different substances, k is material dependent.

Modern depth profiling instruments operate with energies down to a few hundred eV, resulting in a decay length of well below 1 nm for materials not suffering from segregation.

3 TOF-SIMS: Basics and Instrumentation

In the two sections of this chapter, very general remarks on TOF-SIMS will be made, before the particular instrument on which the instrumental and analytical work of this study was carried out is described.

3.1 Principles of TOF-SIMS

After two decades [43], TOF-SIMS is now widely available with about 200 commercial instruments installed worldwide and a number of laboratories offering analytical service ([44] and references therein). Although it is now a mature surface analytical technique, only one comprehensive book describes the principles and applications [2], and only a few, not very recent, review papers are available [45, 46, 47].

The basic information gathered by a TOF-SIMS instrument is the mass spectrum of the secondary ions generated from a single ion pulse. The mass m of each ion with charge q is measured via its time-of-flight

$$t = L \cdot \sqrt{\frac{m}{2qU_e}}$$

through an analyzer of length L after an acceleration voltage U_e has been applied. The mass resolution of the analyzer is defined by the primary pulse width Δt_{start}, the energy distribution leading to a flight time difference Δt_{drift} for different ions of the same mass and the precision of the registration system Δt_{stop}:

$$R = \frac{m}{\Delta m} = \frac{t}{2\Delta t} = \frac{t}{2 \cdot \sqrt{\Delta t_{start}^2 + \Delta t_{drift}^2 + \Delta t_{stop}^2}}$$

Since the secondary ion generation leads to an energy distribution of some eV width, Δt_{drift} dominates the mass resolution if no means of energy focussing is applied. A widely used type of energy focussing device is a reflectron [48]. The common reflectron is a single stage electrostatic mirror, combined with two linear drift regions. Ions with higher kinetic energy penetrate further into the retarding electrostatic field of the mirror, consequently travelling on a longer trajectory. This compensates for their higher velocity compared to other ions of the same mass, but with smaller kinetic energy. If the length of the linear drift regions is chosen appropriately, ions with different energy reach the detector simultaneously. The single stage reflectron is capable of energy focussing to a first order. For higher order energy focussing, improving the mass resolution especially if the energy spread of the secondary ions is large, requires a two stage reflectron or other energy focussing devices [49].

Parallel Detection of all Masses

Each pulse of primary ions generates a full mass spectrum of the surface, although the intensity in a single pulse spectrum is very low. Usually, only a few secondary ions are generated per primary pulse, but secondary ions of all masses are collected in parallel and the spectrum is accumulated from many primary pulses. This feature of TOF-SIMS together with the high transmission of the analyzer and the low background due to the single ion counting allows very high sensitivity for surface species.

Surface Imaging

If the ion gun delivers laterally focussed ion pulses, the spectral information can be combined with the spatial origin of the secondary ions, resulting in a mass resolved image of the region of interest. To generate it, the primary beam is scanned over a square region of the sample and the intensity of selected mass intervals is color-coded into an intensity map for this mass range [50].

Depth Profiling

Usually, TOF-SIMS needs only to remove a sub-monolayer amount of material from the sample (*static SIMS* [51]) because of its high sensitivity. In this case, the total area that is damaged by the ion beam after the analysis, which is the sum of the microscopic areas damaged by each ion, is below 1 % of the irradiated area. If an additional, high current ion beam is applied together with the pulsed ion beam generating the secondary ions, the sample is continuously eroded and the intensity of the masses of interest can be displayed as a function of the depth in a depth profile.

For several years, the performance of conventional computers has been sufficient to store the time-of-flight for each secondary ion detected, together with the lateral coordinates of the corresponding primary pulse, in a raw data file. This file stores the full information of the measurement and opens up a wide variety of post-measurement data treatment routines to be applied in order to retrieve the maximum amount of information from the data (*retrospective analysis*).

3.2 Dual Beam Technique for Depth Profiling

As described in the last section, TOF-SIMS is using a pulsed ion beam with a very low duty cycle[14] for the analysis and is consequently causing only little sample erosion, in contrast to the classical dynamic SIMS instruments (magnetic sector, quadrupole). As a result, TOF-SIMS was not considered as a depth profiling tool for a long time. The crucial step forward was the introduction of the dual beam mode in the mid-90's [52, 53, 54]. Here, the erosion of the sample is performed by a low energy sputter ion source, while the analysis of the receding surface is accomplished with the high energy, pulsed analysis beam in the center of the sputter crater.

This is in strict contrast to the set-up of the classical dynamic SIMS instruments, where only one ion beam is rastered over the sample and forms the sputter crater. Here, secondary ions generated by the DC beam are extracted and transferred to the analyzer which is working as a mass filter, i. e. only the mass of interest is transmitted to the detector.

The magnetic sector instruments have the advantage of high mass resolution, but they suffer from a strong extraction field of ~ 10^3 V·mm^{-1} necessary to get high transmission. This extraction field influences the primary ions hitting the target, making it difficult if not

---

[14] The duty cycle is the fraction of the time during which the ion beam is switched on. For example, pulses with a width of 20 ns at a repetition rate of 10 kHz correspond to a duty cycle of 2E-4.

impossible to choose energy and impact angle of the ions independently. Only recently, floating columns and shielded extraction lenses made the low energy profiling with magnetic sector instruments possible without too much coupling between primary beam and extraction field.

In quadrupole instruments only low extraction fields of ~ 10 $V \cdot mm^{-1}$ are applied, allowing the primary beam parameters to be completely independent from the analyzer setup. But the analyzer is not capable of high mass resolution, limiting the sensitivity for some species suffering from mass interferences (like P in Si, interference of ^{31}P and ^{30}SiH) and complicating the interpretation of data from sample systems with high chemical complexity.

TOF-SIMS combines essential advantages of both principles: On the one hand, it provides high mass resolution and transmission. On the other hand, the extraction field only has to be high during the short time of secondary ion extraction after the primary ion pulse has hit the sample, and can be switched off during the sputter phase, allowing easy reach of the sample with very low energy sputter ions at any desired angle of incidence. In addition, since the analyzer is not a mass filter, the ions are detected in parallel, which overcomes the need to identify the masses of interest prior to the analysis and switch the analyzer between those masses.

The disadvantage of TOF-SIMS, the pulsed operation, can be overcome and to some extent converted into an advantage by applying efficient timing modes and high performance ion guns for low energy sputtering and efficient analysis.

An overview of the characteristics of the different types of SIMS depth profiling instruments is given in Tab. 1.

SIMS instrument	time-of-flight	magnetic sector	quadrupole
mass resolution	10^4	10^4	10^3
extraction field[15]	10 $V \cdot mm^{-1}$	10^3 $V \cdot mm^{-1}$	10 $V \cdot mm^{-1}$
transmission	10^{-1}	10^{-2}	10^{-3}

Tab. 1: Overview over the typical characteristics of the different types of SIMS depth profiling instruments [54, 55].

The decoupling of sample erosion and secondary ion generation in TOF-SIMS makes it the ideal tool for laterally resolved depth profiling (3D micro analysis). Ion optical considerations imply that high lateral resolution can only be achieved with high energy ion beams. If, as in classical dynamic SIMS, only one beam is applied, this has to be used at energies of 10 keV or more in order to realize a lateral resolution of some 100 nm with

---

[15] Extraction field during sputter phase. For TOF-SIMS, the extraction is pulsed to 10^3 $V \cdot mm^{-1}$ during the analysis phase

acceptable current density [56, 57]. Although this can also be achieved with reactive ions like O_2 and Cs, the yield improvement is limited, since the high beam energy results in a high sputter yield and therefore a low concentration of the reactive ions in the matrix even at normal incidence (cf. 2.2). Additionally, the transient width, the depth interval over which the steady state conditions are reached, is comparatively large due to the large projected range of the primary ions, and of course the energy dependent depth resolution is also restricted (cf. 2.1).

In TOF-SIMS, the analysis beam is used in a laterally high resolved mode to image the receding surface while the sputter beam is eroding the sample. Both beams operate in their optimal energy range: the analysis beam at high energy, providing good lateral and mass resolution, while the sputter beam is operated at low energy, as in a normal depth profiling mode, to optimize depth resolution and ionization yield. The parameters of the two beams can be set individually, allowing maximum flexibility according to the analytical task.

As discussed before, the depth resolution in dual beam depth profiling is only influenced by the sputter beam. This statement is based on the assumption that the atomic mixing is dominated by the low energy beam and that the amount of mixing introduced by the analysis beam is negligible. In this case, the damage caused by the high energy beam is continuously removed while the sputter beam proceeds to greater depth.

Up to now, there is only little knowledge about the transition from sputter beam dominated dual beam depth profiling to a situation where both beams have comparable influence on the atomic mixing in the temporary surface region [58, 59, 60]. The depth resolution deteriorates once the high energy beam is becoming noticeable and in the extreme case, when the erosion is dominated by the high energy beam, the depth resolution will be limited by the atomic mixing caused by the analysis beam. For micro analysis, this is of special interest due to the large current densities applied by the focussed high energy analysis beam. A more detailed investigation of this transition will be presented in section 5.1.

3.3 Instrumentation

3.3.1 Description of the TOF-SIMS IV

All experiments presented in this work have been performed on instruments of the TOF-SIMS IV type. This chapter describes the status of the instrument at the beginning of this work. The instrument is based on a design developed in the Department of Physics at the

University of Muenster [61], which is now continued by ION-TOF GmbH [62]. It is very versatile with respect to possible configurations and to the samples which can be analyzed.

General Layout of the Instrument

The TOF-SIMS IV is usually equipped with two ion guns, one for analysis, producing very short, intense ion pulses of less than 1 ns for high mass resolution, and a low energy sputter gun for sample erosion (Fig. 3). Both guns are mounted at an angle of 45° to the sample. The sample is located on a 5-axis motorized manipulator with a horizontal travel range of 155 x 105 mm and 360° rotation to be able to reach every position of a sample of up to 200 mm diameter.

The secondary ions are analyzed by a vertical time-of-flight analyzer of the reflectron type [48, 49, 63] with 2 m drift path and a channelplate/scintillator/photomultiplier detector arrangement. The analyzer has a typical mass resolution *m/Δm* of 9000 at mass 29 u, which is more than sufficient for all applications discussed here.

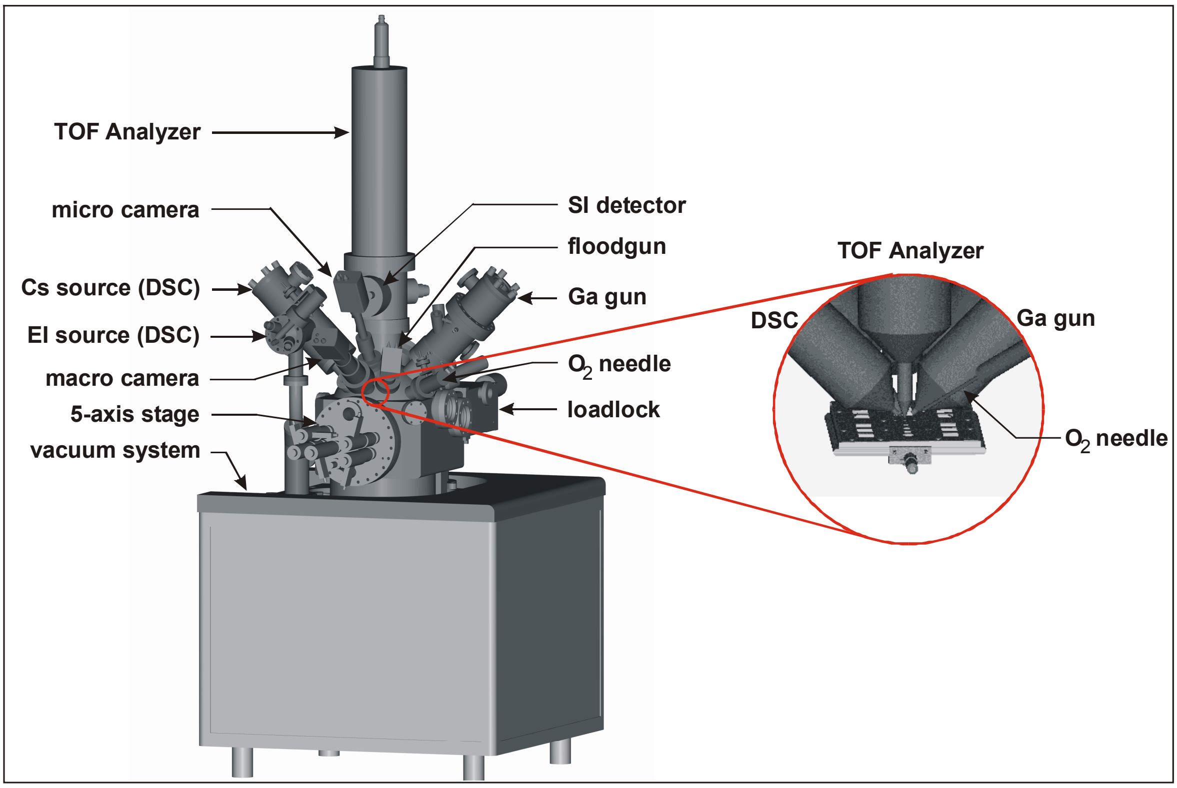

Fig. 3: Layout of the instrument. The inset on the right shows the 100 mm sample holder inside the main chamber and the arrangement of the guns (dual source column (DSC) for sputtering and Ga gun for analysis) and the TOF analyzer above the sample.

In the ultra-high vacuum analysis chamber, a working pressure of $5 \cdot 10^{-10} – 5 \cdot 10^{-9}$ mbar is obtained. Navigation on the sample is software controlled and supported by two CCD cameras.

Additional accessories are a pulsed low energy electron gun for charge compensation and an electronically regulated leak valve with a capillary reaching to the analyzed area, allowing the controlled increase of the partial pressure of a gas of choice in the vicinity of the sample, e. g. oxygen.

The complete vacuum system and all electronic devices are computer controlled by a Windows^{TM} based PC. This computer is also equipped with a time-to-digital converter (TDC) and timing generator. The latter controls all pulsed procedures of the instrument, while the TDC performs the actual time-of-flight measurement of the secondary ions with a time resolution of up to 50 ps and count rates of up to 10^6 Hz.

Analysis Gun

Due to the time-of-flight principle, the primary beam generating the secondary ions has to produce short pulses of high intensity, and it should be possible to focus the beam down to small areas for localized secondary ion generation. All of these requirements can only be satisfied by an ion source of high brightness.

The standard analysis gun of the TOF-SIMS IV is a 25 keV liquid metal ion gun (LMIG) [64] emitting isotopically enriched ^{69}Ga [65]. The Ga gun can be operated in different modes displayed in Tab. 2 which define compromises between pulse width (mass resolution), spot size (lateral resolution) and beam current (data rates) [66].

mode	pulse width	spot size	DC current
bunched	600 ps	5 µm	25 nA
burst-alignment	1 – 300 ns	250 nm	1.5 nA
burst	1.5 ns	300 nm	1.5 nA
collimated	1 – 300 ns	100 nm	50 pA

Tab. 2: Modes of the Ga gun.

For depth profiling, the gun is usually operated in bunched mode [65, 67] at reduced energy of 15 keV, since the lateral resolution of a few µm is fully sufficient to localize the beam in the enter of the sputter crater, but high mass resolution is mandatory. In this mode, the gun produces 15 – 25 ns pulses that are compressed to a pulse width of 600 ps by electrodynamic bunching. The bunching increases the energy width of the beam to 3 - 5 % of the beam energy, which leads to a high chromatic aberration of the target lens and limits the minimal spot size to several µm. On the other hand, it increases the current density during the pulse by about a factor of 30, consequently increasing the number of secondary ions generated per pulse compared to an non-bunched pulse of the same width.

Another mode applied in this study is the burst-alignment mode, used because of its good lateral resolution at a reasonable DC current. The pulse width can be chosen depending on the mass resolution required. The longer the pulse, the smaller is the mass range resolved with better than nominal mass resolution[16]. Typically, the pulse width is set to 200 ns, giving nominal mass resolution up to 100 u.

The disadvantage of not being able to obtain high mass resolution simultaneously to sub-µm lateral resolution can be overcome by applying the burst mode [68], which, apart from the pulse generation, is similar to the burst-alignment mode. In this mode an additional pulsing unit is used to cut a sequence of 1.5 ns pulses with a period of 25 ns from the long pulses, leading to a series of spectra separated by this period. The maximum number of pulses applied has to be set to a value which avoids overlapping of the spectra up to the mass of interest. By summing the series of spectra, the intensity can be increased by a factor of 4 – 10 while reaching a mass resolution $m/\Delta m$ of about 6000 at mass 29 u.

Dual Source Column (DSC)

For sample erosion, the instrument is equipped with a low energy ion gun with an energy range of 1 keV to 10 keV, carrying two different ion sources. This setup allows easy switching between a thermal ionization cesium source for profiling electronegative secondary ions or for MCs^+ clusters and an electron impact (EI) gas ion source for noble and reactive gas operation. The standard gas used in the EI source is oxygen for profiling electropositive elements in positive SIMS. The Cs source is arranged on the ionoptical axis of the gun, but the EI source is mounted at 90° to this axis and its ion beam is deflected into the axis by a 90° pulsing unit, which can also generate short pulses. Mass filtering of the sputter beam is performed by a Wien filter which can separate the other alkali metals from Cs, and doubly charged and monoatomic gas ions from the main species.

A second application of this ion column is the generation of short pulses in order to use it as an analysis gun. Cs is interesting as a primary ion due to its high mass and the high current density that can be reached in pulsed mode, and the EI source can produce a wide variety of primary ions (e. g. Ar^+, Xe^+, SF_5^+) making it the ideal tool for basic studies on secondary ion generation [69] and for the analysis of organic materials using molecular

---

[16] Nominal mass resolution means that species of different nominal mass can be distinguished (e. g. ^{28}Si and ^{29}Si), in contrast to species with the same nominal mass (e. g. ^{29}Si and C_2H_5). The higher the mass, the smaller is the difference in flight time between two adjacent nominal masses and therefore the primary pulse width has to be chosen accordingly.

primary ions [70, 71]. To support the analysis option, the dual source column for both sputtering and analysis (high energy sputter gun) is equipped with a bunching unit and apertures designed for the operation at energies of up to 10 keV, compromising the target current in sputter mode. The voltage range of the electronics is 1 – 10 kV, the operation at energies down to 500 eV is possible with special electronics.

Typical performance data of the DSC in sputtering mode are given in Tab. 3, a more detailed description of the column itself will be given in section 4.1 together with the improvements in performance that could be achieved during the optimization and specialization of the column for lower beam energies, sacrificing the analysis option.

energy	Cs	O_2	spot size
500 eV	6 nA	8 nA	50 µm
1 keV	14 nA	16 nA	50 µm
3 keV	30 nA	60 nA	50 µm
10 keV	70 nA	100 nA	50 µm

Tab. 3: Typical performance data of the dual source column.

3.3.2 Implementation of the Dual Beam Mode

The typical operational mode for depth profiling with the TOF-SIMS IV is the interlaced mode, where the flight time of the secondary ions in the analyzer between the pulses of the analysis beam is used to erode the sample. The timing scheme in Fig. 4 explains the course of events. After the sub-ns pulse of the analysis gun has hit the target, the secondary ions are extracted into the analyzer during a period of time of up to 10 µs. While the ions are travelling towards the detector, the extraction is switched off, and an extraction bias is applied to prevent ions generated during the sputter phase from entering the analyzer.

While the extraction voltage is off, the sputter gun and – if necessary – the electron flood gun for charge compensation are switched on until the end of the timing cycle. The whole timing cycle is repeated with a frequency of typically 10 kHz, corresponding to a cycle time of 100 µs.

Instead of the extraction bias, the secondary beam blanking in the time-of-flight analyzer can be applied in order to preclude ions generated during the sputter phase from reaching the detector. This allows the extraction bias to be used for example to optimize the charge compensation. In the interlaced mode for dual beam depth profiling, the sputter gun is operating at a duty cycle of 75 – 95 %, depending on the width of the extraction pulse relative to the cycle time.

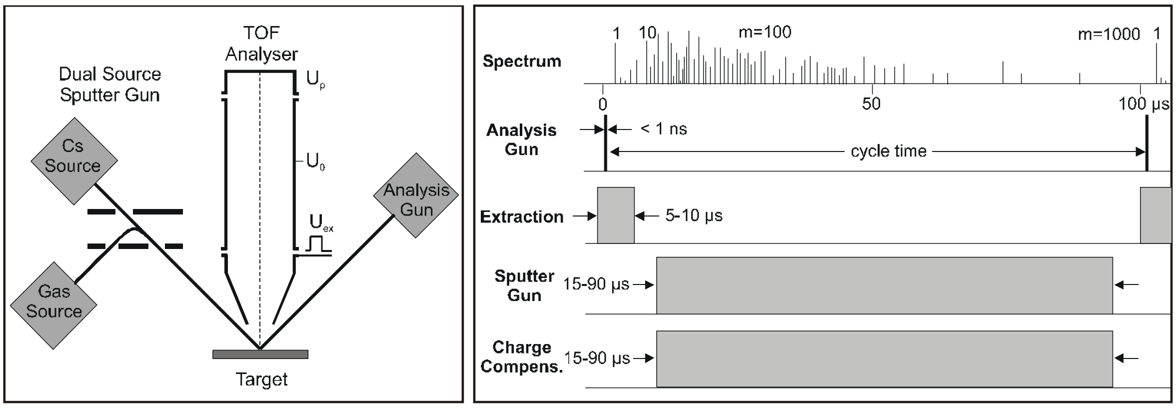

Fig. 4: Instrumental layout and timing diagram for depth profiling in interlaced mode.

In some cases, especially on bulk insulators, the charge applied by the sputter beam within one cycle is not fully compensated by the simultaneous operation of the electron flood gun. This results in an unstable sample potential and therefore a large integral energy spread of the secondary ions, reducing mass resolution (see 3.1) and transmission. In these cases, the non-interlaced mode is a solution, allowing the insertion of a phase where the charge compensation is working solely to remove the charge of the last sputter phase before an analysis phase begins.

In the non-interlaced mode, the sample erosion and analysis are sequentially organized. The sputter gun is used to remove a certain amount of material, typically for some seconds. During this sputter phase, the analysis gun is blanked. Afterwards, one or more scans over the center of the sputter crater are acquired with the analysis gun, while the sputter gun is blanked. The duration of sputter and analysis phase are similar, and the charge compensation can be operated in both phases. The non-interlaced mode avoids the fast switching of the extraction voltage (if no charge compensation is applied during the analysis phase), since the change between sputtering and analysis phase takes place only every few seconds. But it also reduces the duty cycle of the sputter beam to 40 – 50 % which corresponds to an increase in measurement time by a factor of two. Additionally, the sputtering is not continuous but interrupted by the analysis phase, increasing e. g. the influence of the residual gas on the chemical state of the surface during the analysis phase. In the interlaced mode, as opposed to the non-interlaced mode, the two beams operate quasi-simultaneously and quasi-continuously.

All data shown in this work have been acquired using the interlaced mode. Only for one example in the following chapter, the non-interlaced mode was used because of the very strong charging.

4 Instrumental Developments

As a first chapter of results, this section describes the instrumental enhancements obtained during this work, which are mainly related to the depth profiling and imaging capabilities of the TOF-SIMS technique. The following demands for improvements were addressed and could be met:

- Higher speed of erosion both for low and high energy sputtering while allowing a further decrease in beam energy for ultimate depth resolution.
- Improving the low energy MCs^+-cluster profiling by reducing the Cs surface concentration and making it adjustable independently from the sputter yield and beam energy.
- Increase of the data rates to reduce the measurement time or to increase the dynamic range.
- Making molecular primary ions with high lateral resolution routinely available, mostly for the analysis of organic systems[17], but also to study the mixing contribution of the analysis beam for different ion species.

Meeting these demands opens up new application fields or amends the capabilities in already existing applications. Fundamental and analytical results that were achieved using the developments presented in this chapter will be discussed in chapter 5.

---

[17] The application to organic samples is not part of this work

4.1 Low Energy Sputter Source

The dual source column described in section 3.3.1 is capable of both low energy sputtering and operation as an analysis gun. This broad application led to a design of the source that was not fully optimized for one of the operational modes, but was a compromise. With the gaining importance of TOF-SIMS depth profiling and the demand for better depth resolution, both the energy range of 1 – 10 keV and the target current, especially at the lower end of the energy range, were not appropriate anymore.

The objective of the development of a new dual source column was to design a dedicated low energy sputter gun. It should operate with Cs and O_2 in the energy range of 0.2 – 2 keV with optimum stability and increased target current at any energy. To achieve this, the ion optical transfer system was adapted, while the ion sources remained unchanged to a large extent.

Keeping the principle of the ion generation also means keeping the brightness of the ion sources constant for a given energy. The brightness of an ion source is defined as the current density per steradian. As long as this value is constant, the total current that can be transported to the target is mainly a function of the beam angle that is accepted by the column. Unfortunately, decreasing the beam energy increases the relative energy spread and consequently decreases the brightness of the source proportionally to the kinetic energy. In order to raise the target current at a given energy or to keep the target current at lower energy, the angular acceptance of the transport optics has to be increased.

The following features of the high energy sputter column limit the angular acceptance, but were mandatory for the analysis mode:

- Small entrance slit for 90° pulsing unit to give small pulse width [75].
- Small blanking aperture at target lens for good mass filtering and acceptable spot size limited by spherical aberration of target lens.
- Relatively small apertures at source and crossover lens matched to the angular acceptance given by the two features above.

The most critical part is the aperture of the target lens. To compensate for the required increase in diameter, the spherical aberrations had to be addressed in order to keep the focus of the beam at a reasonable value. Since the diameter of a spherical limited beam

$$r_{sp} = -M \cdot \alpha^3 \cdot C_{sp}(M)$$

is strongly dependent on the angle α, the coefficient of the spherical aberration $C_{sp}(M)$ has to be decreased by a factor of eight if – as in this case – the angle is doubled and the magnification *M* is maintained. Therefore, a completely new target lens was developed, which was optimized for low spherical aberration and still fits geometrically into the limited space available. Since the maximum beam energy is limited to 2 keV, it is possible to work with an accelerating lens which made it easier to achieve low spherical aberrations

For the design of a new lens, we used a combination of *Mathematica 4.0* [72], a mathematical software that can handle analytical expressions and formulas, and SIMION 3D [73, 74], an ionoptical simulation tool.

To start, a generalized parametrical function was created that represents the axial potential of the new lens. This function already included the restriction to negative lens voltages and the fact that the lens should have only one electrode that is not grounded. In *Mathematica*, the flight path for ions through the axial potential was solved, the focus was determined, and the position of the focal distance adjusted by scaling the potential. For this potential, the coefficient of the spherical aberration $C_{sp}(M)$ was calculated and fed into an optimization algorithm (three dimensional simplex with simulated annealing) that varied the parameters of the function representing the axial potential.

After the convergence of the optimization, a radial expansion of the potential function was used to calculate equipotential planes that could be manufactured as electrode surfaces. These planes were simplified to make it possible to produce them, the axial potential of several of these representation was calculated with SIMION 3D and again compared via $C_{sp}(M)$.

The result of this optimization was an accelerating lens that uses a lens voltage of about 3.8 times the value of the beam energy (2 keV beam energy: - 7.5 keV lens voltage), making operation at substantially higher energies difficult due to a relatively small gap between the electrodes in the design. The same lens design, but in decelerating mode, is used as a transport lens after the 90° deflection. Here, the spherical error of the lens is not too crucial, so the loss in quality by operating it at positive voltage is negligible.

With the new target lens, the aperture diameter could be increased by a factor of about two, increasing its area and therefore the transmitted current by a factor of four. At the same time, the angular acceptance is doubled, but the spherical error increases only slightly, because the larger angle is nearly compensated by the reduced coefficient $C_{sp}(M)$.

The revised design of the ion optical column is shown in Fig. 5. All apertures were adjusted according to the angular acceptance defined by the aperture of the target lens and positioned to ensure optimum transmission of the whole ionoptical column.

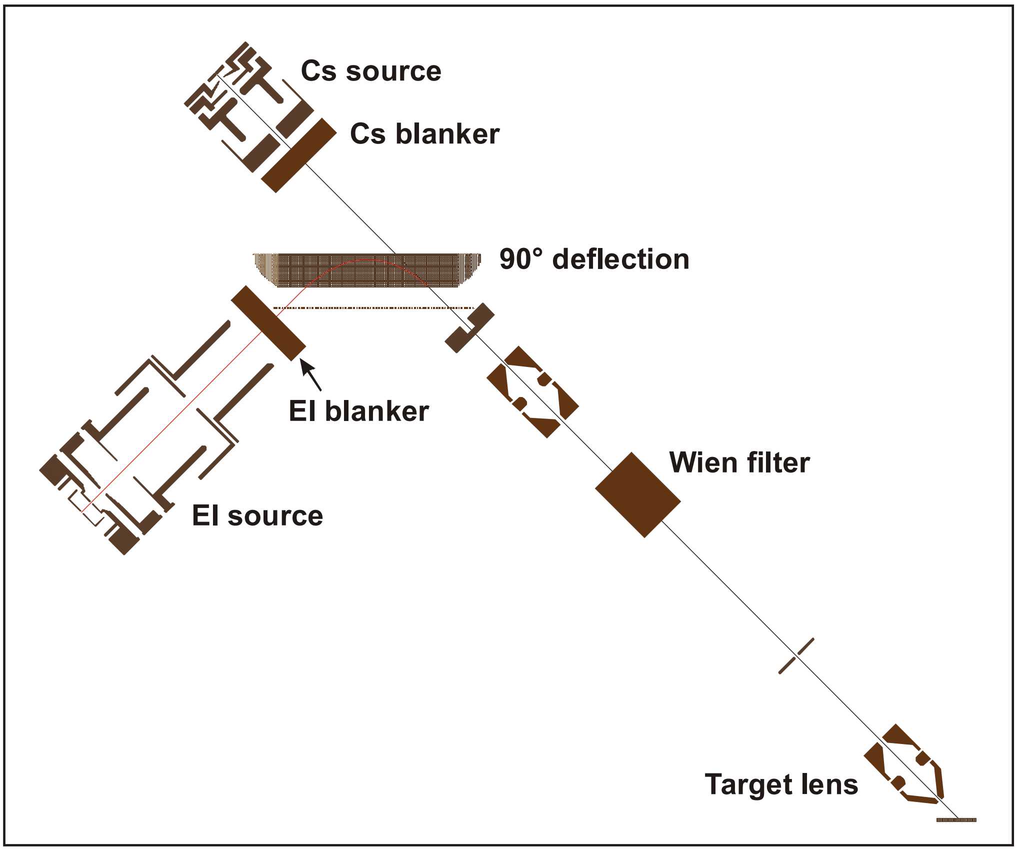

Fig. 5: Schematics of the new low energy sputter column equipped with both sources (not to scale).

Several changes compared to the high energy dual source column were possible in addition:

- In the analysis mode of the DSC, the pulsed 90° deflection was performing the mass filtering of the ion beam [61, 75]. This is now solely done by the Wien filter, allowing the static operation of the 90° deflection unit which greatly improves the electronic stability. The pulsing of the EI source is performed by an additional blanking unit.

- The Wien filter must have the required mass resolution even in combination with the enlarged target aperture to ensure a chemically pure sputter beam. Therefore, it has been re-designed to transmit larger beam diameters and to mass filter the beam at all available beam energies without unnecessary loss in target current.

- In order to increase the performance of the electronics, all high-voltage power supplies were replaced by 0 –2 keV boards optimized for stability. Also, the resolution of the most critical voltages was improved, making the adjustment easier, since smaller changes of the digitally controlled voltages are possible.

- The source lenses of both ion sources were adapted to transmit ions with larger angular distribution, delivering a higher total current to the ion optical column. For the gas ion source, the current values achieved were expected to be only possible with a duoplasmatron source [76]. However the EI source avoids the relatively large energy spread of the duoplasmatron type sources [77]. It also maintains the ability to easily and reliably switch from O_2 to noble gas operation, which is hardly possible with a duoplasmatron due to the missing passivation of the anode, leading to a very short lifetime. Especially at the low energies achievable, the small energy spread of below 1 eV of the EI source is extremely helpful to limit current loss at the 90° deflection, which acts like an energy-analyzer. With a duoplasmatron source, the amount of current lost at the 90° deflection would become unacceptable with lower beam energies.

- The emitter of the Cs source was optimized for higher total current, which is noticeable especially at high beam energies where the transmission of the new column for this type of source is close to 100 % because of its small virtual source compared to the EI source. At low energies, the target current is limited by the brightness of the Cs source, which is independent of the total beam current. The brightness could not be improved by the new design, but even at constant brightness, the larger apertures of the column improve the Cs current.

The sum of the improvements results in a strongly enhanced performance of the source-column combination. The performance of the new low energy sputter gun is shown in Tab. 4, and an example of the excellent stability gives Fig. 6.

energy	Cs	O_2	spot size
500 eV	40 nA	100 nA	75 µm
1 keV	75 nA	250 nA	75 µm
2 keV	150 nA	600 nA	75 µm

Tab. 4: Performance data of the dedicated low energy sputter gun.

The slight increase in spot size compared to the data in Tab. 3 is acceptable. The flat region on the bottom of a typical 300 x 300 µm crater is still large enough to safely position a 100 x 100 µm analysis area without suffering from crater edge effects. Since in TOF-SIMS the selection of the analyzed area within the crater is performed via the positioning of the area irradiated by the analysis beam (spot size: 5 µm), this area is very well defined. This is in contrast to quadrupole and magnetic sector instruments, where the selection of the analysis area is performed via the blanking of the analyzer dependent on the sputter beam position on the target (*electronic gating*). Here, the analysis area is only defined with a precision that is given by the spot size of the sputter beam[18].

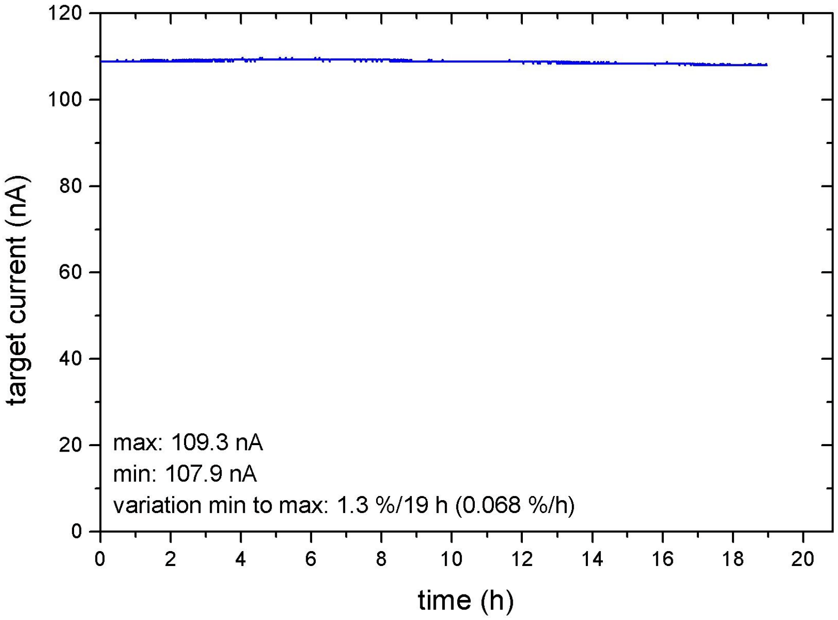

Fig. 6: Target current stability of the low energy sputter column operated with O_2 at 500 eV. This stability of 1.3 % from minimum to maximum over 19 h was obtained after allowing electronics and source to reach equilibrium conditions for about 30 min.

To be able to produce smaller craters which are sometimes necessary on structured samples, the spot size of the low energy sputter column can be reduced by sacrificing a portion of the beam current.

As an example that this development in practice opens new application fields, Fig. 7 shows a depth profile reaching a depth of several µm. A piece of the reflector of a halogen lamp [78] with a concave surface was profiled until the glass substrate was reached. The strong charging and difficult sample geometry were easy to handle in non-interlaced mode, since the pulsed extraction of the TOF-SIMS analyzer makes the charge compensation easy to adjust.

Ten double layers of Ti and SiO_2 can be identified, covered with a B containing glass layer. The substrate is also a B containing glass. The increase in layer thickness from 100 to 200 nm is not an artifact or indication of roughness formation, but a feature of the sample. If the broadening of the layers were an effect of reduced depth resolution, the

---

[18] Magnetic sector instruments can also limit the angular acceptance of the analyzer and therefore the lateral acceptance by an aperture in the analyzer. This technique is also independent of the sputter beam focus.

integral of the signal originating from each layer would stay the same, which is not the case, since the intensity level within the layers stays constant while the width of the layers increases. Nevertheless, the depth resolution decreases slightly with depth as can be seen from the slopes of the layers. This could be an effect of the concave surface leading to some curvature of the crater bottom.

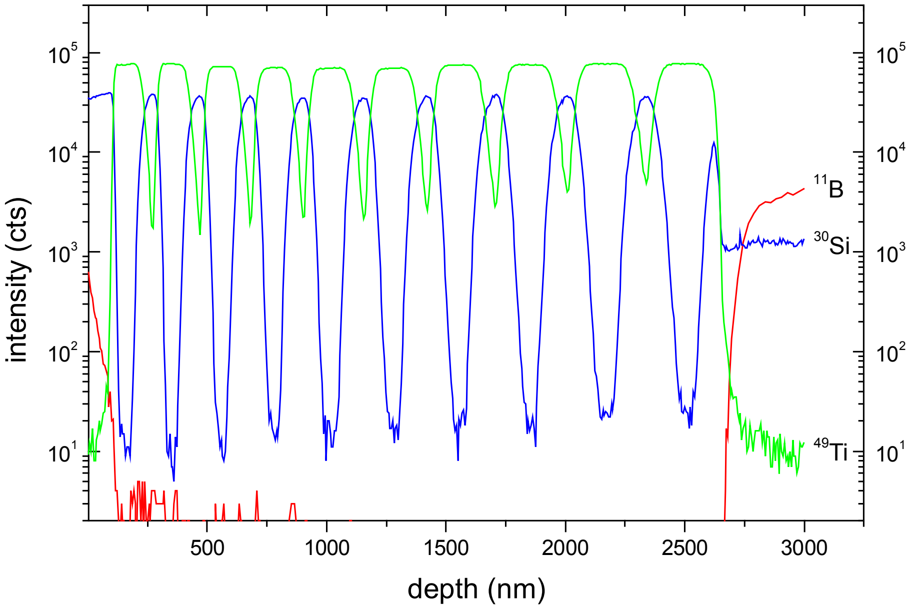

Fig. 7: Wavelength sensitive reflective coating (metal-oxide multilayers) on glass. The thickness of the layers is actually increasing with depth. Sputtering: 2 keV O_2, 540 nA, O_2 flooding. Analysis: 15 keV Ga, 2 pA, with charge compensation, non-interlaced mode.

This example shows that TOF-SIMS depth profiling with the development of the new low energy sputter column enters the field of films with a thickness of up to 10 µm. Simultaneously, the increased performance of the dual source column at low energies also enhances the potential in ultra shallow depth profiling with ultimate depth resolution at energies down to 200 eV.

4.2 Cs-Xe Co-Sputtering

Based on the consideration in section 2.2.3 about the formation of MCs$^+$ cluster ions and the dependence of the surface concentration of the primary ions on the sputter yield, the difficulties of MCs$^+$ cluster profiling at low energies (lower than about 1 keV) become evident. The sputter yield decreases with energy, inducing an increasing surface concentration of Cs under Cs bombardment. For Si, the Cs surface concentration is rather high anyway due to the small sputter yield of Si, but at lower energies, all materials will act similarly. Since the work function of the surface is lowered already for sub-monolayers of Cs by 2 – 3 eV [79], the ionization of the Cs secondary ions becomes ineffective. As explained by the electron tunneling model (section 2.2.1), the ionization is driven by the difference of work function and ionization potential of the secondary ion. If the work function of the surface is lowered, the ionization probability is reduced as well and the fraction of neutral Cs emitted becomes noticeable. At this point, the formation probability of the MCs^+ clusters is reduced proportionally (see 2.2.3), and therefore the MCs^+ yield will decrease the higher the Cs surface concentration becomes.

Reducing the surface coverage is possible by increasing the sputter yield at a given energy. Usually, this is done by changing the angle of incidence to more grazing angles. Especially with quadrupole SIMS angles of up to 80° to the surface normal are reported [80, 81, 82] to give reasonable results. Unfortunately, they suffer from the increased tendency of Si and other target materials to form sputter induced roughness at angles greater than approx. 60° (depending on energy [83]), extended transient effects [84, 85, 86] and from the technical difficulties such as bad crater shape and problems with tilting large samples.

Experiments with Cs evaporation together with noble gas sputtering in order to adjust the Cs concentration have not reached the status of standard application [87] and potentially have difficulties to control the surface coverage precisely with a beam of neutral Cs.

A novel way to reduce the Cs concentration [88] is to dilute the Cs beam by Xe ions, which have the same mass but are chemically inert, in a well defined manner. In contrast to experiments with a Cs and a Ga ion source to remove part of the Cs on the surface by the Ga beam [89], both ion species are transported through one ion optical column, ensuring the same beam position on the target, the same spot size and the same beam energy. To realize this, the EI and the Cs source on the low energy dual source column are operated simultaneously.

There are several reasons for choosing Xe as the operating gas for the EI source. Using the same mass as Cs is important, since the sputter process and the altered layer of the sample should not be changed by the reduction of the Cs concentration except for the chemical influence of the Cs. Although many elements have no or only a small effect on the ionization probability, a noble gas is the safest choice to ensure that there is no additional chemical effect.

But employing Xe has also technical advantages; the EI source needs a gaseous element to ionize[19], and the gas should not influence the highly reactive thermal ionization Cs

---

[19] Working with high vapor pressure liquids evaporated into the vacuum is also possible, but less comfortable.

source which is operating in the same vacuum chamber at elevated temperatures. Besides this, the Wien filter in the sputter column should transmit ions from both sources at the same energy.

In contrast to the normal operation of the sputter column, the 90° deflection unit is pulsed in Cs-Xe co-sputtering mode. The 90° deflection unit acts as a switch between the two species: if the deflection unit is grounded, the Cs ions are transmitted while the Xe ions go straight through the deflection unit and hit a Faraday cup (Fig. 8 *left*). When the deflection is pulsed to about 63 % of the beam energy, the Xe beam is bent by 90° into the ion optical column, while the Cs ions are deflected from the axis and cannot pass the following aperture (Fig. 8 *right*).

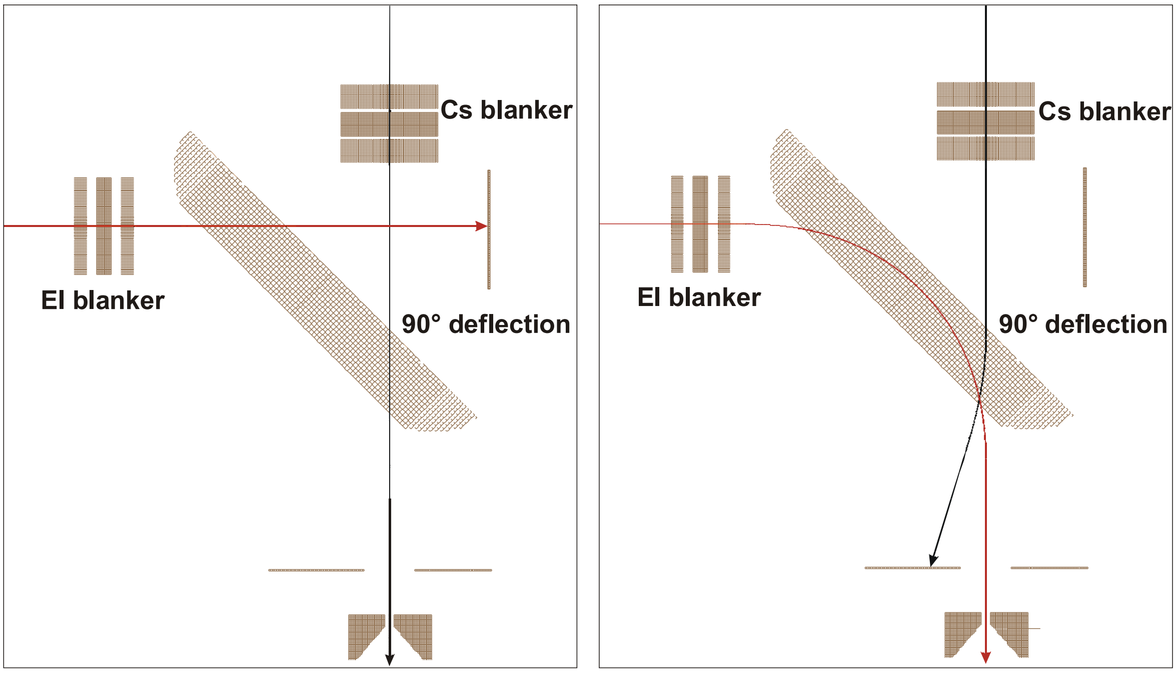

Fig. 8: SIMION 3D [73, 74] simulations of the two states of the 90° deflection The figures show cross sections of the 90° deflection unit of the low energy sputter column. Not shown are the EI source to the left, the Cs source at the top, and the ion optical column at the bottom leading towards the sample.
***left*: grounded 90° deflection allows the Cs beam (black line) to enter the column, while the Xe beam (red line) is hitting a beam stop.**
***right*: activated deflection blanks the Cs beam while the Xe ions are transmitted into the column.**

The total duration of a sputter cycle is determined by the blanking units of both sources which are controlled by the same voltage. Switched to transmission, both beams enter the 90° deflection, but only the Cs beam is transmitted into the column. After an adjustable fraction of the sputter cycle, the 90° deflection is pulsed to high voltage and switches from Cs to Xe transmission. This fraction is called the ‘*Cs fraction*’ R_{Cs}. At the end of the sputter cycle both beams are blanked again.

The *Cs fraction* timing parameter is the only parameter necessary to adjust in order to select the composition of the sputter beam. Fig. 9 shows the measured target current for both species as a function of R_{Cs}. Over a wide range, the target current for both species changes linearly with R_{Cs}, only at the extreme values below 5 % and above 95 %, the different flight times in the pulsing unit lead to deviations from linearity. For precise measurements, the target currents have to be measured individually at the given *Cs fraction*. In most cases, the exact ratio of the target currents is not very critical, so the timing parameter is accurate enough to reproduce the ratio for a given measurement protocol, as long as the DC currents of both sources are known.

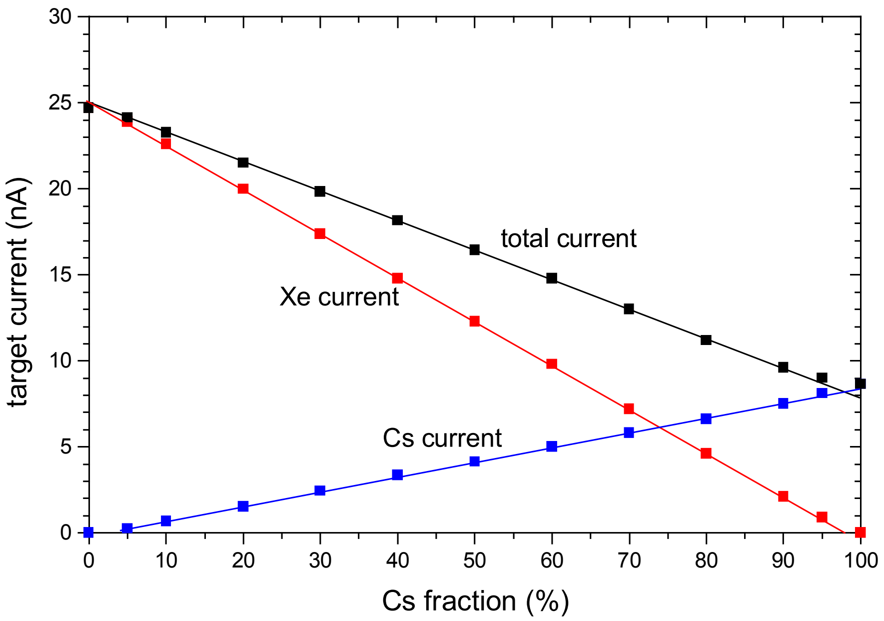

Fig. 9: Target current of Cs and Xe vs. the timing parameter *Cs fraction* (see text). The data are representative for 300 eV operation. The straight lines are linear fits to the data in the range from 10 % to 90 % Cs fraction. Within this range, no significant deviations from the linearity are visible.

The sputter yield difference between the two species is not very large ($Y_{Xe} \approx 1.5\ Y_{Cs}$, measured at 500 eV), and the nuclear stopping power of both species is very similar since they have the same mass. Probably, the difference in sputter yield is mainly due to the build-up of a cover layer of Cs on the surface that partially hides the first layer of the target. Xe is not bound and is therefore either implanted into the matrix or evaporated into the vacuum. As a result, the sputter yield should vary linearly with R_{Cs}, since the coverage should also be linearly dependent on the Cs fraction. Measurements of the sputter yield as a function of R_{Cs} show this linearity, which means that also the Cs coverage is varying linearly with R_{Cs}.

A more general parameter for the adjustment of the Cs-Xe co-sputtering than the Cs fraction, a timing parameter which does not contain any information about the currents of the two ion sources, is the relative Cs concentration c_{Cs}^{rel}. This value is the relative Cs target current I_{Cs} with respect to the total sputter current I_{sp}. In terms of surface concentration, c_{Cs}^{rel} is equal to the Cs concentration relative to the value obtained for pure Cs sputtering. It can be calculated in two ways:

1. Measuring the target currents of Cs and Xe (I_{Cs} and I_{Xe}, respectively) at a given value of the *Cs fraction* gives the exact value of c_{Cs}^{rel}:

$$c_{Cs}^{rel} = \frac{I_{Cs}}{I_{Cs} + I_{Xe}}$$

2. If the accuracy is less important, the relative Cs concentration can also be determined by once measuring the target currents $I_{Xe}^{\max}$ and $I_{Cs}^{\max}$ for 0 % and 100 % *Cs fraction* and using the expression

$$c_{Cs}^{rel} = \frac{R_{Cs} \cdot I_{Cs}^{\max}}{R_{Cs} \cdot I_{Cs}^{\max} + (1 - R_{Cs}) \cdot I_{Xe}^{\max}}$$

where R_{Cs} is the *Cs fraction* timing parameter.

The *Cs fraction* timing parameter R_{Cs} of the Cs-Xe co-sputtering allows easy choice of the Cs surface concentration independently from the beam energy, angle of incidence or other bombardment parameters. c_{Cs}^{rel} can be adjusted from zero up to the steady state value which is true in sputter equilibrium for a pure Cs beam of the same energy and angle.

4.3 High Repetition Rates

The single ion detection in TOF-SIMS limits the count rate for a single nominal mass to the number of primary pulses per second (*repetition rate*), since the dead time of the detection system is always longer than the width of a peak in the mass spectrum. If two secondary ions arrive within the dead time of the detection system, they are counted as only one ion, leading to an underestimation of the true count rate at high secondary ion intensities. To a certain extent, the statistical treatment of the data according to Poisson's statistics can be used to correct this underestimation up to a factor of two or three with only minor uncertainty [90]. The uncertainty is minimized if the number of primary pulses which is taken into account for correction is high enough, and if the number of events detected is at about 80 % of the number of primary pulses. Larger corrections are still relatively accurate, as calculated from the Poisson statistics, but the detector saturation leads to some non-linearity at these extremely high count rates.

An increase in repetition rate is therefore desirable, since it is directly proportional to the maximum dynamic range of a depth profile. It is defined as the number of counts per depth interval at the highest concentration of the analyte divided by the number of counts per depth interval with the analyte absent[20]. One way to improve the dynamic range is to increase the integration time per depth interval, increasing the number of detected secondary ions, but also increasing the measurement time.

When the repetition rate is increased, its reciprocal – the cycle time T – is decreased, which defines the maximum available flight time for the secondary ions, corresponding to the highest detectable mass (m_{max}). If the flux of secondary ions contains ions of higher mass, these are detected in the next timing cycle. Their measured flight time however is wrong by the duration of one or several timing cycles and they appear at too low mass in the spectrum (*wrap-around effect*). In order to avoid this effect, the analyzer is equipped with secondary beam blanking. At a position in the flight path where the dispersion of the secondary ion pulse did not already cause an overlapping of the secondary ions generated by two adjacent primary pulses, a blanking unit removes the ions with a mass higher than the mass detectable at the chosen cycle time. For example, at 2 keV secondary ion energy and 10 kHz repetition rate, the highest detectable mass is around 930 u. For higher repetition rates, the mass range is reduced according to $m_{max} \sim T^2$, limiting the practical repetition rates to < 100 kHz.

The design objective for the increase of the repetition rates was to achieve 50 kHz, which also defines the maximum rate that gives a reasonable mass range (slightly higher than Si) and to implement a strategy to improve the practical value of high repetition rates with respect to mass range limitations.

In the electronics, the increase in power consumption of the high voltage switches proportional to the pulse frequency made the development of new pulsing units for bunching of the analysis gun, pulsed 90° deflection for Cs-Xe co-sputtering and pulsed extraction of the analyzer necessary. All devices attached directly to the instrument had to be designed without fans to avoid vibration, making the task of cooling the switching transistors floated to up to 3 keV challenging. The new pulsing units made improved

---

[20] This is the maximum dynamic range achievable as determined by the counting statistics. Other effects, especially a background that is proportional to the primary current or memory effects, can further reduce the dynamic range of the profile.

power supply boards unavoidable, increasing the number of devices that had to be modified.

As stated above, the maximum detectable mass decreases strongly with the decrease of the cycle time. Tab. 5 gives an overview over the mass range for a number of different cycle times.

cycle time	repetition rate	mass range
20 µs	50 kHz	0 – 37 u
25 µs	40 kHz	0 – 58 u
30 µs	33 kHz	0 – 83 u
40 µs	25 kHz	0 – 147 u
50 µs	20 kHz	0 – 227 u
70 µs	14 kHz	0 – 430 u
100 µs	10 kHz	0 – 930 u

Tab. 5: Mass range as a function of cycle time from 20 – 100 µs (50 – 10 kHz repetition rate).

To overcome this strong limitation, especially at very low cycle times, the timing scheme controlling the secondary beam blanking and the registration system was also re-designed. A new timing parameter called *start delay* was introduced. This parameter is used to shift the start of the registration of the secondary ions, which is normally at mass 0 u, towards higher masses. The *start delay* is scaled in per cent of the cycle time and can have values of up to one cycle time. When it is used, the maximum mass registered is also increased by the same flight time as the minimum mass, virtually shifting a window of constant width over the mass range. Due to the square root dependence of the time-of-flight on the mass, this not only shifts but simultaneously increases the range of masses being transmitted and registered (Fig. 10).

In order to avoid secondary ions generated by different primary ion pulses hitting the detector simultaneously, the secondary beam blanking is switched according to the actual value of the *start delay*. This is possible, since the blanking unit is located much closer to the target than the detector, so the secondary ions originating from one primary pulse are still relatively close together. Only as they travel further through the analyzer does the dispersion of the different masses lead to an overlapping of the ion packages. The analyzer blanker is used to limit the width of the secondary ion package to avoid interference at the detector.

Fig. 10 shows how the registration period is shifted over the mass range and how this results in an increase in the number of nominal masses registered. Especially the time period between the masses 0 u and 1 u can always be used, already increasing the mass range considerably. If, for example, the flight time of H is 3 µs, a *start delay* of 2.9 µs still allows the detection of H. At a cycle time of 20 µs, this increases the maximum detectable mass from 37 u to 49 u. If the H, H_2 and H_3 can be blanked because they are not of analytical interest, a start delay of 9 µs gives all masses from 10 u (^{10}B) up to about mass 73 u, including the most important Si_xO_y clusters.

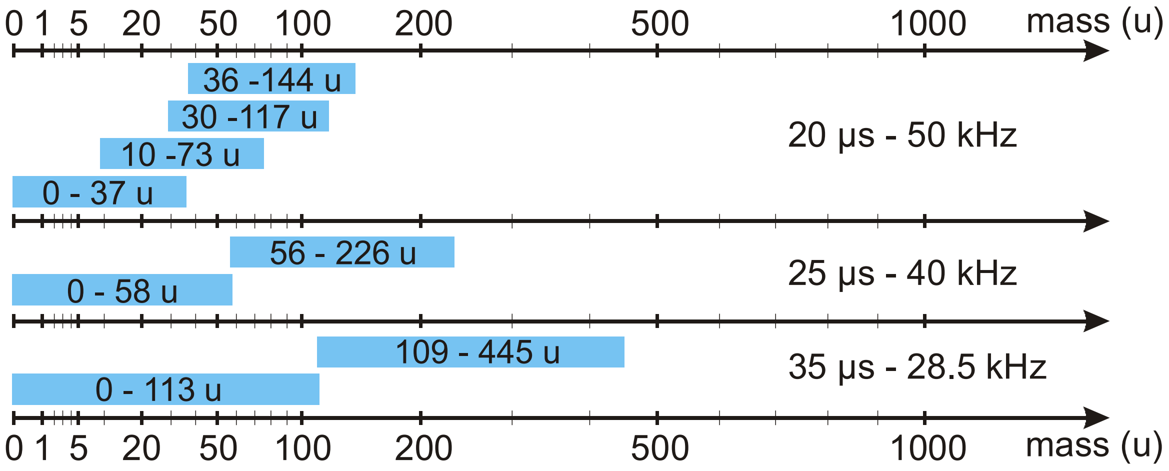

Fig. 10: Mass range possible at 20, 25 and 35 µs cycle time and shift of this interval over the mass scale using the *start delay* parameter. The position and the width on the mass scale changes due to the square root dependence of the mass on the time-of-flight.

The capability of using the *start delay* to select the mass range of interest to some extend independently from the cycle time substantially increases the practical benefit of the high repetition rates. Tab. 6 gives some examples of analytically interesting mass ranges at the highest possible repetition rate and the repetition rate that would be possible at most without *start delay*.

analytical application	mass range	repetition rate w/o start delay	start delay	repetition rate with start delay
B in Si	10 – 70 u	33 kHz	40 %	50 kHz
As in Si	30 – 110 u	28 kHz	79 %	50 kHz
MCs^+	56 – 226 u	20 kHz	100 %	40 kHz
MCs_2^+	109 – 445 u	14 kHz	100 %	28 kHz

Tab. 6: Selected mass ranges at the highest possible repetition rate without *start delay* compared to the repetition rate possible using the *start delay*. The increase in data rate using the *start delay* for a given application is up to a factor of two without loss in analytical information.

Utilizing the changes in the electronics and the timing scheme made the 50 kHz operation feasible, but the timing protocol of the sputter gun was still optimized for lower repetition rates and had to be reorganized to serve the needs that became obvious:

- At 50 kHz (corresponding to 20 µs cycle time), the extraction pulse width of 10 µs plus some small delays reduced the duty cycle of the sputter gun to less than 50 %. To avoid this, the extraction pulsing unit was changed to variable pulse width and is operated with 5 µs at repetition rates faster than 10 kHz, where the maximum mass and hence the time necessary to extract the secondary ions is reduced anyway. When the mass range above 2000 u has to be extracted as well, the extraction pulse width has to be 10 µs, which is the case at repetition rates which allow the detection of these high masses.

- When the energy of the sputter ions is reduced to only a few hundred eV, their velocity is becoming very low and their flight time from the blanking unit of the dual source column to the target makes it necessary to switch the beam off several µs before the extraction is switched on. This loss in duty cycle is noticeable if the cycle time is only a few ten µs. To compensate this, the blanker of the low energy column has to be switched to transmission while the extraction is still on or even before the primary pulse to let the sputter ions travel towards the target. They hit the target just after the extraction has been switched off to start the next sputter cycle. The timing control software now calculates the flight times of the sputter ions to the target depending on beam energy and species. It generates a pulse of the maximum possible duration at a time that lets the ions hit the target just during the *off*-phase of the extraction.

With these changes, the sputter timing is optimized and gives high duty cycles of at least 75 % at 50 kHz, increasing with decreasing repetition rate. Only during the extraction pulse of the analyzer it is necessary to switch the sputter beam off. The duration of this pulse has to be chosen long enough to ensure that all ions which can be detected at a given cycle time enter the analyzer before the extraction is turned off again.

An outcome of the development of the high repetition rates, in this case in combination with the higher sputter currents, is the improved dynamic range in ultra shallow implant profiling. In Fig. 11, a 700 eV BF_2 implant is shown. While the sputter energy can be reduced to 250 eV, the 50 kHz operation of the Ga gun allows a dynamic range which is five times larger than possible with 10 kHz.

The data show the excellent depth resolution, visible at the ^{10}B surface contamination with a decay length λ_d = 0.4 nm; It allows to resolve the shape of the F implant originating from the BF_2 bombardment. The inset, which shows the first 3 nm of the ^{11}B distribution on a linear scale, documents the high density of data points, avoiding any quantification artifacts that could be caused by under-sampling of the very sharp spike of the implant.

Because this example is a very high dose and low energy implant with a B peak concentration of 20 at. %, the detection limit is rather high, since the dynamic range is fixed by the counting statistics. Lower dose or higher energy implants show even lower detection limits for B in Si of 1E16 atoms/cm^3.

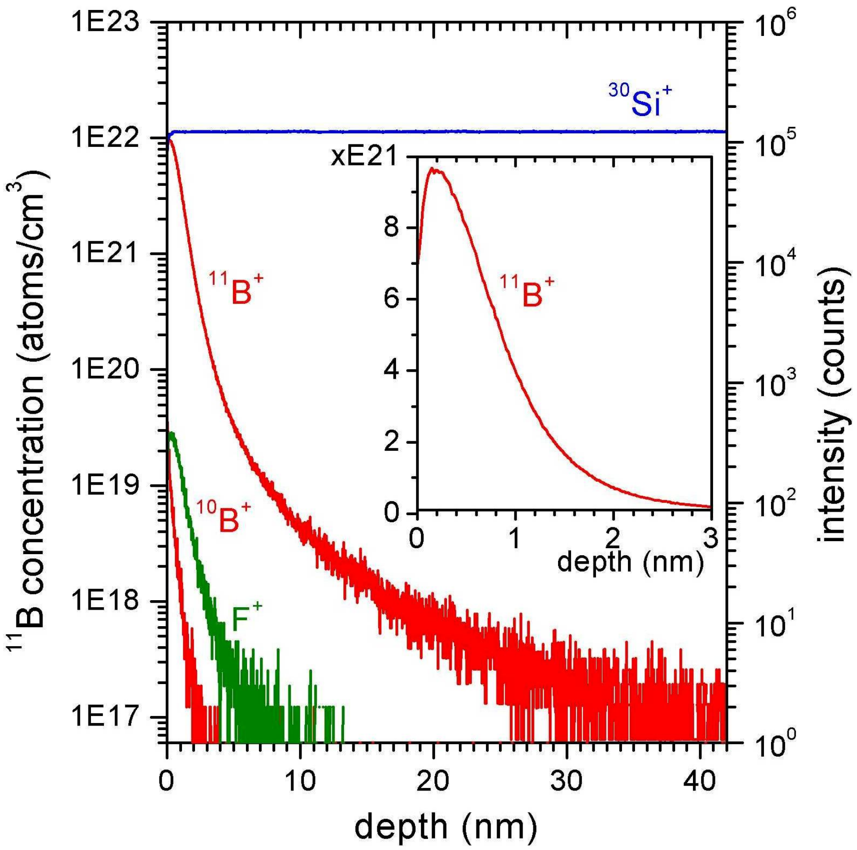

Fig. 11: **Depth profile of a 700 eV BF_2 implant with a dynamic range of five orders of magnitude. Sputtering: 250 eV O_2, 45°, O_2 flooding. Analysis: 15 keV Ga.**

4.4 Au Cluster Ion Source

In recent years, a large number of investigations on the use of polyatomic primary ions in SIMS have revealed their advantages. Using polyatomic ions increases the yield especially for organic molecules without increasing the damaged area per primary ion to the same extend. The strong interest becomes evident in the increasing number of publications on this subject [e. g. 70, 91, 92, 93, 94]. Furthermore, the efforts in modeling the primary ion impact with molecular dynamics (MD) simulations starts to reveal some insights into the physical effects taking place [95, 96].

Besides the use for the analysis of organic materials, the Au source is also important for fundamental studies on the mixing of the analysis beam in dual beam depth profiling, since it can be operated in a similar fashion to conventional Ga sources, but offers several heavier ion species (see 5.1).

A stable, easy to use ion source is necessary to make the use of polyatomic primary ions possible not only in research labs, but also in routine analytical applications. A few years ago, SF_5^+ was the polyatomic ion species attracting the biggest attention [97], but the ion sources were found to have a short maintenance cycle and are only useful for spectroscopy, since they have a spot size of about 50 µm. Other exotic ion sources were and are being used in some groups [98, 99], but they are neither capable of high lateral resolution, nor do they work with good reliability.

In order to achieve better lateral resolution and higher stability, the Au liquid metal ion gun (Au LMIG) has been identified as the source type with the most promising characteristics. It is reasonably stable, has a strong Au_2 and Au_3 cluster emission, and since it is of the LMIG type, has a high brightness making it feasible to focus it down to a few hundred nm.

Due to the high melting point of gold (> 1000 °C), it is not possible to use the pure metal with reasonable lifetime, since the high vapor pressure at the melting point lets the material vaporize into the vacuum very quickly. Instead, eutectic alloys of Au with different other elements (Si, Be, Ge, Sb etc.) are used, reducing the melting point to 300 – 600 °C and giving a lifetime that is equivalent to that of the established Ga LMIGs ([100] and references therein).

When a Au LMIG is to be integrated into a TOF-SIMS instrument, the main task is to develop a mass filter that allows the choice from the different cluster sizes and eliminates the ions of the other alloy constituents. The most obvious choice is a Wien-Filter as used in the dual source column described in section 4.1, but the high mass resolving power required, the small space available and – most critical – the risk of introducing aberrations which limit the target spot size make it difficult to realize.

Since the pulsing technology is available in a TOF-SIMS instrument anyway, the second possibility was technically straightforward to realize: a time-of-flight filter using the different velocities of the cluster pulses between two blanking units to select the cluster of interest.

For the mass filtering, an additional blanking unit (*pre-chopper*) was introduced into the LMIG column (Ga gun) which forms ion pulses of a width slightly larger than the width being finally used (Fig. 12). On their way to the second beam blanker (*chopper*) which usually forms the pulses in Ga operation, the pulses of different ion species separate due to their difference in mass and therefore in velocity. When the species of interest reaches the *chopper*, it cuts it out of the now mass separated ion packages, and the other masses are not transmitted. The parameter used to choose the mass is the delay between the *pre-chopper* and *chopper*, while the width of the pulses is set according to the mode of the gun.

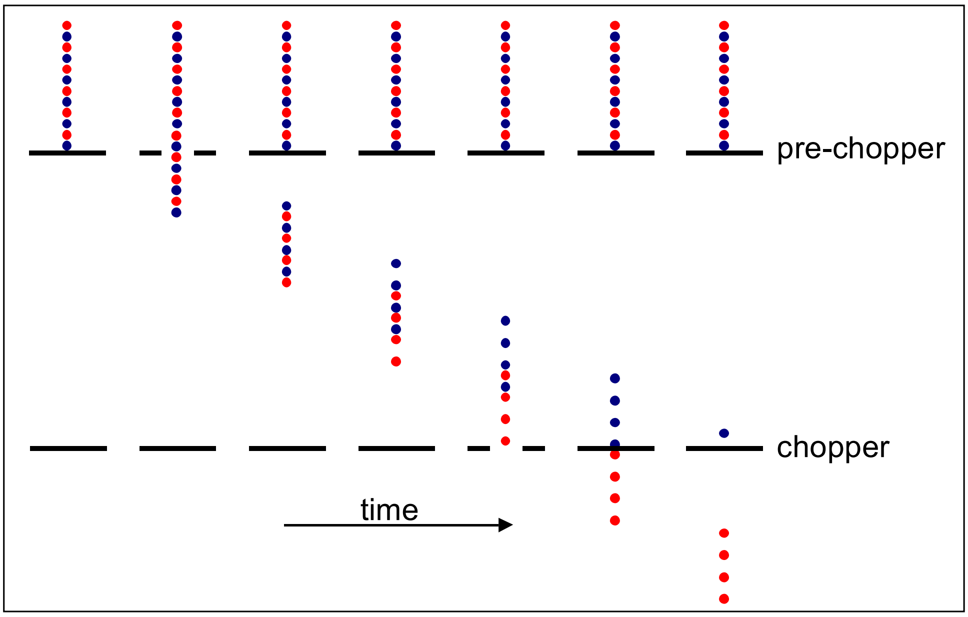

Fig. 12: Time-of-flight mass filter of the Au cluster ion source. The figure shows successive snapshots of the pulse formation from a 2-component ion beam. After the *pre-chopper* has formed an ion package, the ions of different mass (light ions: ●, heavy ions: ●) separate due to the different velocities and only one package is transmitted through the *chopper* towards the target.

The mass resolving power of this mass filter is mainly dependent on the pulse width used. Pulses can be separated as long as the difference in velocity and the distance they travel are large enough to let the pulses diverge completely. In the Au cluster source used here, the *pre-chopper* is located directly behind the source lens. Thus, the flight time between *pre-chopper* and *chopper* is maximized, leading to a high mass resolution of the filter. As a result, the maximum pulse width allowing mass filtering from all parasitic masses for Au, Au_2 and Au_3 is large enough for all analytical applications, both in bunched mode and in long pulse operation for imaging.

Together with the control for the *pre-chopper*, the flight time correction for the primary ions was introduced into the timing protocol, analogue to the time-of-flight correction for low energy sputtering in the dual source column (section 4.1). This ensures that the primary ions, independent of their individual mass, hit the target synchronous to the start of the secondary ion registration, defining the mass 0 u. With this protocol, the timing of the secondary system (e. g. secondary ion blanking) is independent of the primary species, making it very convenient to switch between the Au_n species without adjusting the analyzer setting or the mass scale of the spectrum.

This mass filter was extensively characterized after implementation and is found to be free of any aberrations which limit the spot size on the target. The possible pulse widths are sufficient even at 25 keV and do not limit the use for spectra, mass resolved images, or depth profiles. A possible contamination of the Au^+ beam by Au_2^{++} (probably with very low intensity) cannot be avoided, but also a Wien filter would not be able to distinguish between these species.

The only hindrance of a time-of-flight mass filter is the inability to generate mass filtered DC beams. Due to the differences in the energy distributions of the emitted Au_n clusters [101], the achievable lateral resolution of a DC beam for secondary electron imaging is given by the combination of the lateral resolutions of all species, scaled with their respective fraction of the beam current. Depending on the energy distributions, the chromatic error for the species is different. Since Au_1 is by far the most intense species, the lateral resolution is dominated by the Au monomer and therefore not strongly limited by the other masses.

5 Application and Fundamental Results

The three sections of this chapter will describe analytical results which are based on the instrumental developments described above. The section 5.1 will be focussed on a fundamental aspect of dual beam depth profiling, the contribution of the analysis beam to the atomic mixing and the depth resolution. In section 5.2, the ion formation under varying Cs surface concentrations will be discussed, one way in order to increase the sensitivity of TOF-SIMS especially for MCs^+ cluster profiling.

Section 5.3 deals with a more practical aspect, 3D micro analysis, which is to some extent the ultimate application of dual beam depth profiling, where both ion beams contribute considerably to the sample erosion, and the stabilization of the matrix plays an important role.

5.1 Atomic Mixing in the Dual Beam Mode

As depicted in section 3.1, atomic mixing in the dual beam mode is assumed to be dominated by the mixing caused by the low energy sputter beam. This assumption is valid as long as the sample erosion of the analysis beam can be neglected compared to that of the sputter beam.

In applications with a demand for high dynamic range, for example profiles of shallow implants, or in 3D micro analysis, this assumption may not hold anymore.

To evaluate the transition from a classical dual beam setup, where the removal of material is dominated by the sputter beam, to the erosion of material approximately equally with both beams, a number of experiments on model samples have been performed.

The sample mainly used in these investigations is a boron delta layer structure provided by SEMATECH [102]. The sample consists of 15 MBE-grown[21] ^{11}B layers with a nominal dose of 5E13 atoms·cm^{-2} (corresponding to approx. 0.04 monolayers) which can be considered as infinitely thin, separated by Si layers of nominally 5, 10 and 15 nm thickness (Fig. 13). In this study, only the first 5 delta layers were investigated, and especially the trailing edge of the 5th delta which could be quantified very well due to its relatively large separation of 15 nm from the next B layer.

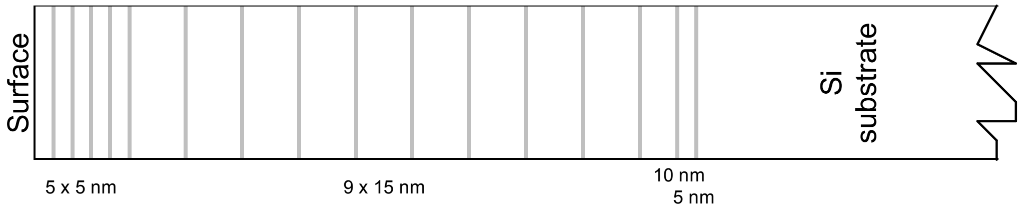

Fig. 13: Representation of the B delta layer sample, indicating the nominal thickness of the Si spacers (gray lines represent B layers). The true depth of the 5th B layer is 22.4 nm [103].

A comparison of depth profile data on this sample with different types of SIMS instrumentation is presented in a paper by Bennett [103], who used the sample in a round robin study to evaluate the depth resolution, precision of depth measurement and concentration determination of different laboratories. This study revealed a true depth of the 5th delta of 22.4 nm which was taken as an internal depth calibration marker for the profiles acquired in this study. Fig. 14 shows an example of the depth profiles taken from this sample. The intensity modulation on the deltas is not an artifact of the SIMS measurement, but a property of the sample. The actual dose scatters around the nominal dose leading to a scatter in the peak heights, but as the B dose per layer is low enough, the resulting scatter in the thickness is negligible.

Some of the data in this chapter was measured with a SiGe delta layer sample provided by Philips [104], consisting of a Si substrate with 6 very thin SiGe layers separated by nominally 30 nm. Here, the trailing edge of the 1st layer located at a depth of 38.4 nm was taken as a measure of the depth resolution. The true depth of the 1st layer was calibrated by profiling the sample and measuring the physical crater depth with a stylus profilometer [105], assuming constant sputter rate throughout the profile.

---

[21] MBE: molecular beam epitaxy

In both cases, the decay length was determined at a depth larger than about 2x the projected range of any of the primary ions, assuring the complete evolution of the altered layer. Therefore, the measured depth resolution is a result of the combination of both ion beams in steady state and not influenced by the transient region of the profile. For a depth smaller than this, the incomplete build-up of the altered layer may lead to an overestimation of the depth resolution. The surface contamination, for example, always shows an excellent depth resolution only correlated to the sputter beam energy, regardless of the analysis beam parameters. Because the projected range of low energy ions and therefore the transient regime is only a few nm, the surface contamination can be probed with only minor transient effects. The large projected range of the high energy ions perceptibly reduces their mixing contribution on the first few nm.

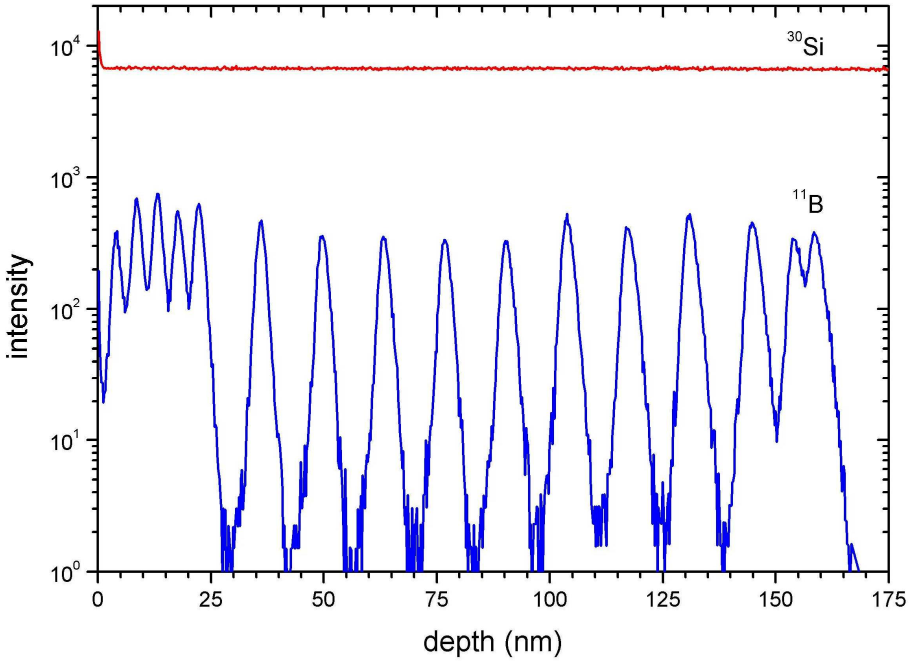

Fig. 14: Depth profile of the B delta layer sample. Sputtering: 500 eV O_2, 45°, O_2 flooding. Analysis: 15 keV Ga.

In order to define a quantity that reflects the relative influence of both ion beams, the sputter and the analysis ion beam, the sputter rate ratio R was chosen.

$$R = \frac{R_{sp}}{R_{an}} \propto \frac{I_{sp}}{I_{an}} \cdot \frac{Y_{sp}}{Y_{an}} \cdot \frac{A_{an}}{A_{sp}}$$

R is given by the sputter rate of the sputter beam R_{sp}, divided by the sputter rate of the analysis beam R_{an}. It is proportional to the ratios of the sputter and analysis current (I_{sp}, I_{an}) and the respective sputter yields (Y_{sp}, Y_{an}) and conversely proportional to the ratio of the irradiated areas (A_{sp}, A_{an}). It expresses the ratio of the amount of materials which is sputtered by the two beams. If, for example, $R = 100$, the low energy sputter beam removes 100 times more material than the analysis beam. The larger R is, the lower is the fraction of material being removed by the analysis beam, and the lower is the damage caused by the high energy irradiation. Typical values of R for dual beam depth profiling range from some 100 to several 1000. A very typical set of parameters for a depth profile of a B implant on a non-structured wafer is: 500 eV O_2 sputter beam, 45°, 100 nA, 300 x 300 µm^2, O_2 flooding, $Y_{sp} = 0.3$ and 15 keV Ga analysis beam, 45°, 3 pA, 100 x 100 µm^2, $Y_{an} = 1.7$. These conditions result in a value of ~ 650 for the sputter rate ratio.

Previously, instead of the sputter rate ratio R, the current density ratio was taken as a criterion to ensure that the erosion is dominated by the low energy beam. A common opinion was that with the low duty cycle of the analysis beam (10^{-4} or lower), the mixing is not significant [106, 52]. But the duty cycle ignores the differences in current density and sputter yield of the two ion beams, which become more important as the sputter energy and, as a result, the sputter yield Y_{sp}, is reduced. If the current density ratio for a given set of bombardment parameters is 1000, a sputter yield difference of 10 between the low and the high energy beam – e. g. for 250 eV O_2 and 15 keV Ga – results in a sputter rate ratio R of only 100, which is comparatively low.

The experiments discussed in this chapter were only possible using both the low energy sputter gun and the high repetition rates, because variations in the sputter rate ratio of more than three orders of magnitude had to be applied. The high repetition rates allowed the application of high analysis beam currents without leaving the single ion counting regime, while the high sputter currents gave an erosion speed sufficient to reach the necessary depth at all energies within a reasonable time.

In order to calculate the sputter rate ratio, the sputter yield Y_{an} of the analysis beam has to be determined. A direct method is to generate a sputter crater and measure its dimensions with a stylus profilometer. From the volume of the crater and the dose applied by the Ga gun, the sputter yield can be calculated and should be a good approximation for the yield under the conditions used during the depth profile.

One has to keep in mind that Y_{an} is strongly dependent on the oxidation state (changes in sputter yield by a factor of 2 – 4.5 [16, 17]) and the crystal structure (changes in sputter yield by a factor of 2 or more [3, 107, 108, 109]) of the matrix. Thus, it has to be measured under the same conditions which are used during the depth profile, while the oxygen sputter beam is simultaneously eroding (and oxidizing) the sample.

An approximation of these conditions was used for 10, 15 and 25 keV Ga in order to measure the sputter yield of Si directly. The sample was bombarded with a Ga beam of high current density and with long pulses, and the flux of secondary ions was measured using the pulsed extraction mode of the TOF analyzer. The secondary ion signal was maximized by adjusting the O_2 flooding pressure, ensuring full oxidation of the matrix. The secondary beam blanking and the detector were adjusted for operation with the extremely high count rates under these conditions.

The values determined from these experiments are given in Tab. 7. Obviously, the difference in sputter yield caused by the oxidation is relatively pronounced (reduction by a factor of ≈ 2.5), and is in the same range as the data Iltgen [16] measured for the change in sputter yield with oxidation state, although he worked with Ar, O_2 and SF_5 beams and below 1 keV energy.

Additionally, the table gives simulated data generated with SRIM2000 [110, 111], a software based on the widely used TRIM Monte-Carlo code for simulating ion-solid interaction, using the *'monolayer collision steps'* mode for precise modeling of the near-surface cascades that mostly contribute to sputtering. The values for both the oxidized and non-oxidized case agree quite well, supporting the validity of the measured data.

	not oxidized		**oxidized**	
Ga energy	**measured**	**simulated**	**measured**	**simulated**
10 keV	4.4	4.7	1.6	1.8
15 keV	4.6	5.4	1.7	2.0
25 keV	4.9	5.8	1.9	2.1

Tab. 7: Sputter yield of Si under Ga bombardment. Measured and simulated [110] with and without O_2 flooding for oxidized and non-oxidized Si.

A second method to determine the sputter yield Y_{an} is to use the depth profile data itself. Here, the fact that the sputter rates S_{sp}, S_{an} of the sputter and analysis beam add to an effective sputter rate S_{eff} is used. The effective sputter rate

$$S_{eff} = \frac{z_m}{T_m} = S_{sp} + S_{an}$$

can be determined by the known depth z_m of a marker in the sample and the time T_m necessary to sputter to this marker.

The sputter rates of the two beams are given by the expressions

$$S_{sp} = \frac{I_{sp} \cdot Y_{sp}}{A_{sp} \cdot \rho_{Si}^{n} \cdot e} \qquad S_{an} = \frac{I_{an} \cdot Y_{an}}{A_{an} \cdot \rho_{Si}^{n} \cdot e}$$

where I_{sp}, I_{an} are the target currents, A_{sp}, A_{an} the irradiated areas and Y_{sp}, Y_{an} the sputter yields, respectively. The particle density of silicon is given by ρ_{Si}^{n} and has a value of

$5{\cdot}10^{22}$ atoms·cm^{-2}, *e* is the elementary charge. Resolving the formulas give an expression for the sputter yield of the analysis beam:

$$Y_{an} = \frac{A_{an} \cdot \rho_{Si}^{n} \cdot e}{I_{an}} \cdot \left(\frac{z_m}{T_m} - \frac{I_{sp} \cdot Y_{sp}}{A_{sp} \cdot \rho_{Si}^{n} \cdot e} \right)$$

The main source of error for the determination of Y_{an} is the small difference of large numbers resulting from the terms in the bracket of the formula above. Small errors in the value of the sputter current I_{sp} or the sputter yield of the sputter beam Y_{sp} lead to a large error in the sputter yield of the analysis beam Y_{an}.

Y_{sp} was calculated from the profiles with a large sputter rate ratio, where the analysis beam can be disregarded. Profiles with a small sputter rate ratio were taken to calculate an average Y_{an}, because here the influence of the analysis beam is most pronounced and the error from the term in brackets minimized.

Fig. 15[22] shows the decay length of the B delta as a function of the sputter rate ratio *R*. For large values of the sputter rate ratio, the decay length is constant and only influenced by the atomic mixing of the sputter beam. The value of 0.75 nm is similar or better compared to the reported values for single beam profiles at this energy [112, 113, 114, 115] (often normal incidence).

The decay length increases with decreasing sputter rate ratio and becomes significant in the range of $R \approx 500$ and below, indicating the increasing contribution of the high energy beam to the atomic mixing. This is also confirmed by the comparison of the data for 500 eV and 1000 eV sputtering with 15 keV analysis (Fig. 16). At the higher sputter beam energy, the depth resolution for high sputter rate ratios is about 1.2 nm, which is also consistent with literature data [112], and the influence of the analysis beam becomes obvious at slightly smaller values of *R*. Extrapolating the decay length to $R \rightarrow 0$, the decay length should reach the value that corresponds to sputtering solely with the high energy beam.

The increase in decay length for a given sputter rate ratio is larger for a higher analysis beam energy (Fig. 15), as expected. The decay length for the *pure* high energy beam (corresponding to R = 0) increases roughly proportional to the square root of the beam energy [16]. For sputter rate ratios in the range observed here, the dependence of the decay length increase on the analysis beam energy is slightly stronger than a square root law, but the statistics of the data do not allow a detailed analysis of the correlation.

---

[22] In all graphs, the lines are straight connections of the measured data points in order to guide the eye (unless not stated otherwise)

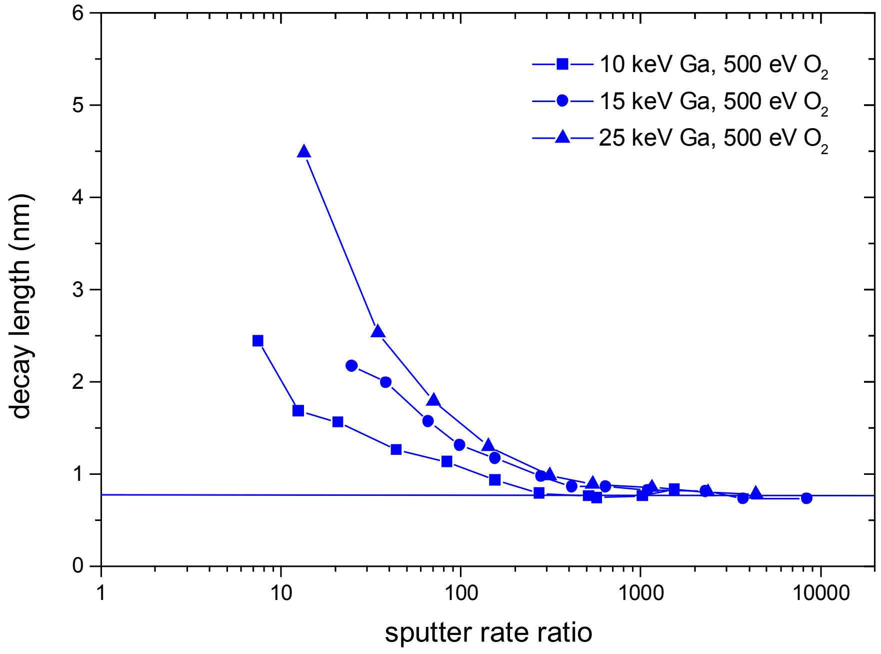

Fig. 15: **Decay length of B in Si as a function of the sputter rate ratio for three different analysis beam energies. Sputtering: 500 eV O_2, 45°, O_2 flooding. Analysis: 10, 15 and 25 keV Ga.**

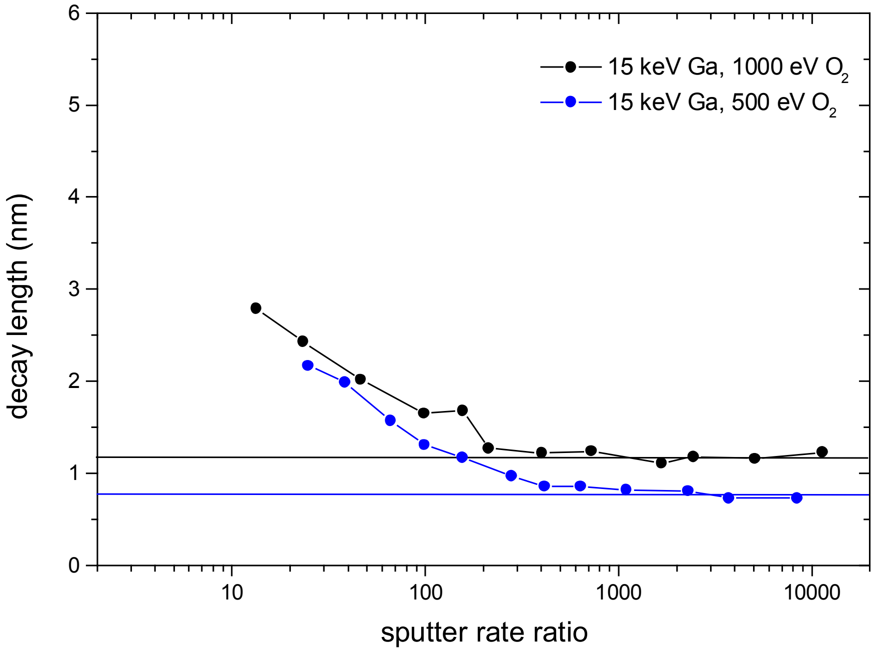

Fig. 16: **Decay length of B in Si as a function of the sputter rate ratio, for two different sputter beam energies. Sputtering: 500 and 1000 eV O_2, 45°, O_2 flooding. Analysis: 15 keV Ga.**

With lower sputter rate ratios, the influence of the sputter beam diminishes and the atomic mixing of the analysis beam becomes dominant. This becomes evident in Fig. 16, where at low sputter rate ratios the decay length difference between the two sputter energies becomes very small.

To ensure that these observations are not limited to B in Si, similar experiments have been performed on SiGe delta layers in Si. The results show a similar behavior of decay length as a function of the sputter rate ratio (cf. Fig. 17). Although the absolute value of the decay length for high sputter rate ratios is larger (approx. 1.25 nm) at the same sputter energy, which is due to the different material properties of Ge under irradiation compared to B [116], the decay length increases also with decreasing sputter rate ratio and increasing analysis energy. To illustrate that the depth resolution is not limited by the sample itself, one result for 250 eV bombardment is also presented, showing a significantly better depth resolution. For the B delta layer sample, lowering the sputter beam energy did not lead to a significant improvement in depth resolution, implying a limitation of the depth resolution by the sample. This proves that the concurrent behavior of sputter and analysis beam is not dependent on the intrinsic depth resolution of the sample.

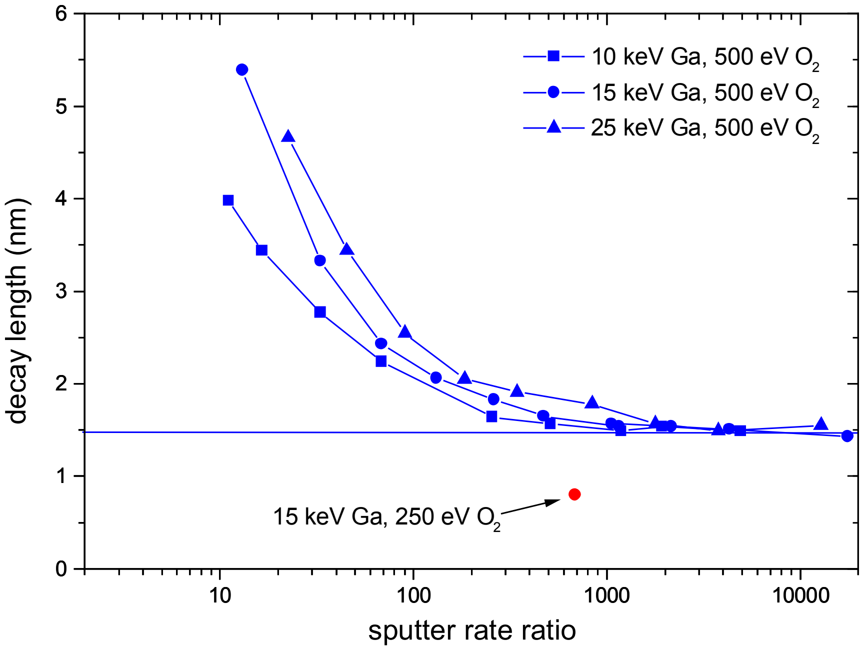

Fig. 17: Decay length of Ge in Si as a function of the sputter rate ratio. Analysis with varied primary ion energy. Sputtering: 500 eV O_2, 45°, O_2 flooding. Analysis: 10, 15 and 25 keV Ga.

From the theory of sputtering processes, it is a valid assumption that the use of heavier primary ions at a given sputter energy will reduce the mixing effect of the analysis beam, because the range of the primary ions in the target is reduced. Some authors confirm this assumption [16], some do not [117]. Especially when cluster ions are used, the reduced mixing compared to monoatomic primary ions in undisputed. Molecular dynamic simulations indicated that the collision cascade is much more closely confined to the surface region for cluster ion bombardment [118]. To test these statements with respect to heavy and cluster ion beams as analysis species, the same experiments as discussed above have been repeated with Au, Au_2 and Au_3 as analysis ions, applying the newly developed Au cluster ion source. The results are displayed in Fig. 18, together with the data for Ga which were already shown in Fig. 15. For all primary species, the energy was 15 keV, and the sputtering was performed under identical conditions (500 eV O_2 bombardment, O_2 flooding).

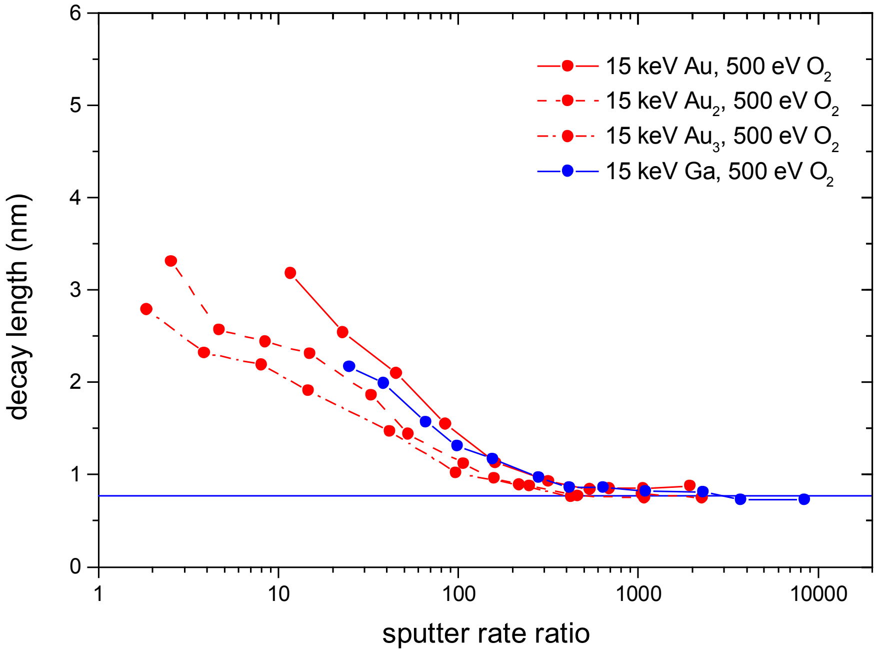

Fig. 18: **Decay length of B in Si as a function of the sputter rate ratio. Analysis was performed with varied Au cluster size and Ga for comparison. Sputtering: 500 eV O_2, 45°, O_2 flooding. Analysis: 15 keV Ga, Au, Au_2 and Au_3.**

In general, the trend for the Au_n (n = 1 - 3) species is as expected: the decay length increases with decreasing sputter rate ratio as for Ga bombardment. The larger the Au cluster, the lower the atomic mixing at the same sputter rate ratio. In other words, at a given level of additional atomic mixing by the analysis beam, the sputter yield of the Au clusters and consequently the amount of material sputtered for analysis increases with the Au cluster size.

Closer examination reveals some details of interest. The decay length for Ga and Au_1 are very similar, and in contradiction to the theoretical prediction, the mixing of the Ga primary ions is slightly smaller than Au_1. However, the method of determining Y_{an} and its sources of error suggest that this small difference may not be significant.

The second interesting observation is the extrapolation of the decay length towards $R \to 0$. As opposed to Ga, the depth resolution for Au_2 and Au_3 is not that severely reduced at very low sputter rate ratios, which will be useful for applications for which low values of *R* are unavoidable.

The following table (Tab. 8) gives the Si sputter yield of the primary beam as measured in this study at full oxidation. Note that the values for Ga have been measured by sputtering craters as described above. It should be mentioned that, although the oxidation state can be adjusted by the oxygen pressure, the sputter yield of the primary beam may be different when it is applied simultaneously with a low energy sputter beam of high current density, because the formation of the altered layer is influenced by both beams.

Also, the very low sputter rate ratios applied in some of the experiments, especially for Au_2 and Au_3, can result in a oxygen depletion of the surface by the analysis beam. In this case, higher sputter yields compared to fully oxidized Si would be measured when the additional sputter rate by the analysis beam is used for the calculation.

		sputter yield	
species	energy	measured	simulated
Ga	10 keV	1.6	1.8
	15 keV	1.7	2.0
	25 keV	1.9	2.1
Au	15 keV	3.0	2.8
Au_2	15 keV	10	3.8[23]
Au_3	15 keV	31	4.7[23]

Tab. 8: Si sputter yield of primary species at full oxidation of Si matrix during O_2 sputtering. Calculated from additional sputter rate of B delta layer sample at high current density of analysis beam. Data from SRIM 2000 [110] simulation for comparison.

Obviously, there is a non-linear effect exceeding the increase in sputter yield with the number of constituents. It has been observed on other sample systems as well during this investigation. A direct simulation of the sputtering with Au_2 and Au_3 is not possible with the TRIM code, because cluster bombardment is not implemented, so only a simplified simulation was possible[23]. The non linearity is in contrast to MD simulations which predict an increase in sputter yield more or less proportional to the number of constituents [119]. These simulations were carried out at much lower energies because of calculation time restraints, but as yet the discrepancy between them and the experimental results has not been explained.

The Ga data, however, agree very well when measured by both methods. Also, the agreement between Monte-Carlo simulation [110] and experiment for the mono atomic

---

[23] The simulations for Au cluster sputtering were carried out under the assumption of single ion sputtering with the kinetic energy divided between the constituents (e. g. Au_3, 15 keV was simulated as 3 x Au_1, 5 keV).

primary ions is quite good. In general, some uncertainty of the values in Tab. 8 remains due to the sources of error in the determination as described above, but the agreement is reasonably good.

The sputter rate ratio *R* was introduced in the beginning of this chapter as a means of characterization of the relative material removal of both beams. *R* includes all parameters that are of interest when talking about sputtering theory, the current densities of both beams and their sputter yields. For the practical work, this quantity is also valuable since it is easy to calculate before a profile is started and indicates if the depth resolution will be affected by the atomic mixing of the analysis beam.

However, in order to judge the quality of the results, there is one important parameter missing which quantifies the amount of information which can be gathered from the sample. For a depth profile, the information has to be normalized to a certain depth interval, because the relevant information arises from a limited volume. This volume is given by the analysis area (the raster area of the analysis beam) and the depth over which the structure is distributed. Hence, the useful yield Y_u is given by the expression

$$Y_u = \frac{\text{\# of detected secondary ions}}{\text{amount of sputtered material}} = \frac{I(^{30}Si)/A(^{30}Si)}{\left(PIDD_{sp} \cdot Y_{sp} + PIDD_{an} \cdot Y_{an}\right) \cdot A_{an}}$$

where $I(^{30}Si)$ is the intensity of the least abundant Si isotope[24], $A(^{30}Si)$ its abundance, $PIDD_{sp,\,an}$ the primary ion dose densities of the two beams, $Y_{sp,\,an}$ their sputter yield, respectively, and A_{an} the area irradiated by the analysis beam. In this study, the useful yield of Si was determined, optimized by adjusting the O_2 flooding to maximum ^{30}Si intensity. For other secondary ions, the relation between the useful yields for diverse experimental conditions is assumed to be comparable to the useful yield of ^{30}Si.

Taking Y_u to re-plot the Ga data reveals nothing surprising: the useful yield changes only very moderate when changing the beam energy, which leaves the relative position of the curves nearly untouched (Fig. 19). Up to a useful yield of approx. 10^{-5}, the depth resolution is not affected by the analysis beam. However, at higher useful yields, the decay length shows the already discussed dependence on analysis beam energy and intensity.

---

[24] In TOF-SIMS, the count rates of the matrix species are often so high, that a minor instead of the main isotope is followed.

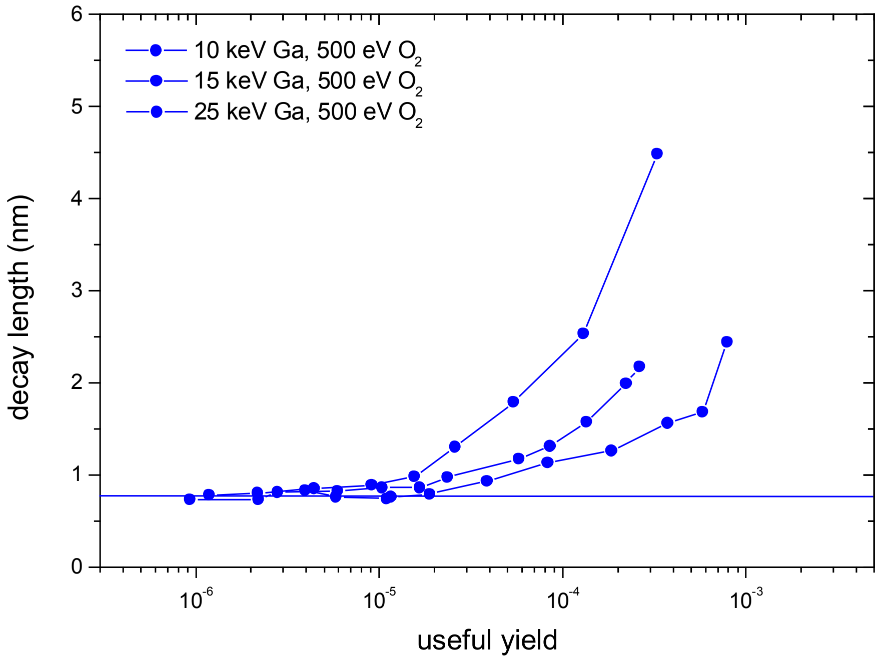

Fig. 19: **Decay length as a function of useful yield for different Ga energies. Sputtering: 500eV O_2, 45°, O_2 flooding. Analysis: 10, 15 and 25 keV Ga.**

In the case of Au bombardment, the position of the curves undergoes a significant change if the data is plotted against the useful yield (Fig. 20). The relative position of the data for the Au_n changes and the curves move closer together. The difference between 15 keV Ga and Au_1 is also becoming very small compared to Fig. 18.

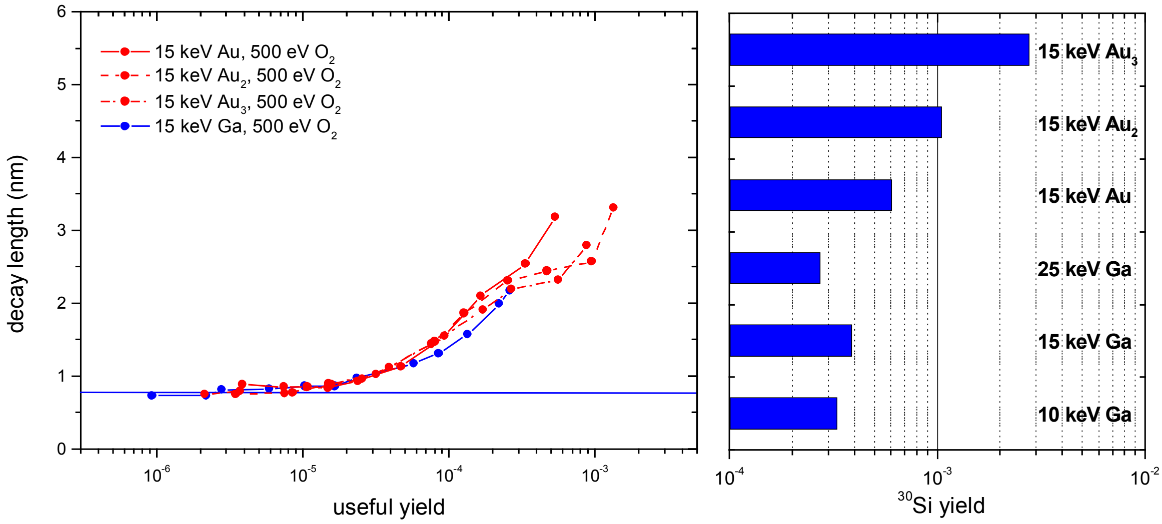

Fig. 20: ***left*: Decay length as a function of useful yield for different analysis ions. Sputtering: 500eV O_2, 45°, O_2 flooding. Analysis: 15 keV Ga, Au, Au_2 and Au_3.**
***right*: ^{30}Si yield of the different primary ion species and energies. The Ga data do not vary much with energy, but the higher Au clusters show a pronounced increase in yield.**

This observation is explained by the following consideration: the additional sputter yield of the Au_2 and Au_3 primary ions does not lead to the same extend to a higher number of secondary ions per primary ion. The sputter yield of Au_3 is a factor of about 18 higher than the sputter yield of Ga (both at 15 keV and measured with simultaneous O_2 sputtering and O_2 flooding, Tab. 8), but the number of secondary ions generated per primary ion only increases by a factor of 7 (Fig. 20). At the same sputter rate ratio, the useful yield for Au_3 is about a factor of 2.5 smaller than for Ga. The same holds true for Au_2, the useful yield is about a factor of 2.2 smaller than for Ga at the same value of R. Only for the monomer Au, the useful yield compared to Ga is the same if the sputter rate ratio for both species is equal.

Since the useful yield is the quantity best describing the amount of information gathered per depth interval, the comparison of the Au clusters to Ga at 15 keV leads to the conclusion that Au clusters as analysis species do not reduce the amount of additional atomic mixing. The higher sputter yield of the Au clusters with limited increase in mixing cannot be converted into an advantage, since the ionization – at least on this sample system – is less and cancels the advantage out. Only if the ionization stays at the same level as with Ga, Au clusters may be the better choice on certain samples.

As a result of the experimental data reported above, it is possible to suggest ways of avoiding the mixing contributions from the analysis beam to the resolution of a depth profile. The easiest way to check the influence of the primary beam is to reduce the repetition rate or target current of the analysis gun by a factor of two and repeat the profile to check whether an improved depth resolution results. If this is not feasible, the calculation of the sputter rate ratio from the experimental parameters (if necessary, with estimated values for the sputter yield of the analysis gun) gives an indication of the relative influence of the two beams.

In general, the analysis area should always be as large as possible for the given sputter area. If the crater shape is limiting the depth resolution, because the analysis area chosen was to large, retrospective analysis can in most cases eliminate this problem without too much loss in dynamic range.

But even if the sputter rate ratio chosen was too small, the relationship between the decay length and sputter rate ratio is very smooth, with a small slope for a wide range of sputter rate ratios. If the ultimate depth resolution is not required, which is often the case since only a few samples are so well prepared, a too small sputter rate ratio has no disastrous effect, at least for the sample systems evaluated in this study.

For 3D micro analysis, the mixing of the high energy beam will definitely play an important role, but the depth resolution is still in the range of a few nm as long as the low energy beam sputters the majority of the sample atoms. For extreme cases, Au cluster ion sources may be an interesting alternative to Ga, since there are indications that the mixing in the regime of sputter rate ratios around and below 10 is significantly lower with cluster ions.

5.2 Yield optimization under Cs Bombardment

Cs-Xe co-sputtering was already introduced in section 4.2, where the considerations resulting in this approach – the decrease of the MCs^+ yields with decreasing Cs sputter energy due to the surplus in Cs coverage – are explained as a motivation for the development of this special technique. In the following chapter, some fundamental results gathered using the Cs-Xe co-sputtering will be presented and discussed to shed some more light on the formation of MCs^+ cluster ions.

As already depicted in section 2.2.1, the formation of negative secondary ions described by the electron tunneling model is expected to increase exponentially with the work function. The work function of the surface is reduced by the build up of the Cs concentration until it is lowered to the minimum value. At higher Cs concentrations, the work function cannot be decreased any more, and the yield should stabilize.

This is the first model that was tested using the Cs-Xe co-sputtering. A Si wafer was analyzed with the Ga gun while the Cs concentration was defined by bombardment with Cs and Xe. The yield for several secondary ions was measured as a function of the *Cs fraction*, and plotted vs. the relative Cs concentration (Fig. 21).

The figure clearly shows the expected behavior: the linear increase in the semi-logarithmic plot corresponding to an exponential yield increase at low Cs concentrations and the stabilization for high Cs concentrations. For all secondary species taken into account, the transition from increasing to stable yields is slightly different on the Cs concentration scale, but nearly all reach the plateau well below a relative Cs concentration of 1. Interestingly enough, even the Cs follows this trend, although it does not reach the plateau at the maximum Cs concentration available at this sputter energy. But the fact that the Cs concentration does influence the emission of Cs^- ions indicates that the emission of Cs^+ may not be independent of the Cs concentration either.

From an application point of view, the Cs concentration at the surface for maximum yield of negative secondary ions should be as high as possible. With the trend towards lower beam energies and therefore low sputter yields and consequently high Cs concentrations, the yields will almost always be in the plateau region, which also makes the yield less sensitive to small changes in the Cs concentration at interfaces. No care has to be taken in order to reduce the Cs concentration in this mode.

One example for an artifact caused by varying Cs concentration at an interface is the Si^- spike at the SiO_2/Si interface of thin oxides [120] that is a segregation effect of the Cs. The accumulation of Cs at the interface increases the Si^- yield further than in the Si bulk. The spike disappears when the Cs concentration in the bulk is high enough that an increase in Cs concentration does not increase the negative secondary ion yield further.

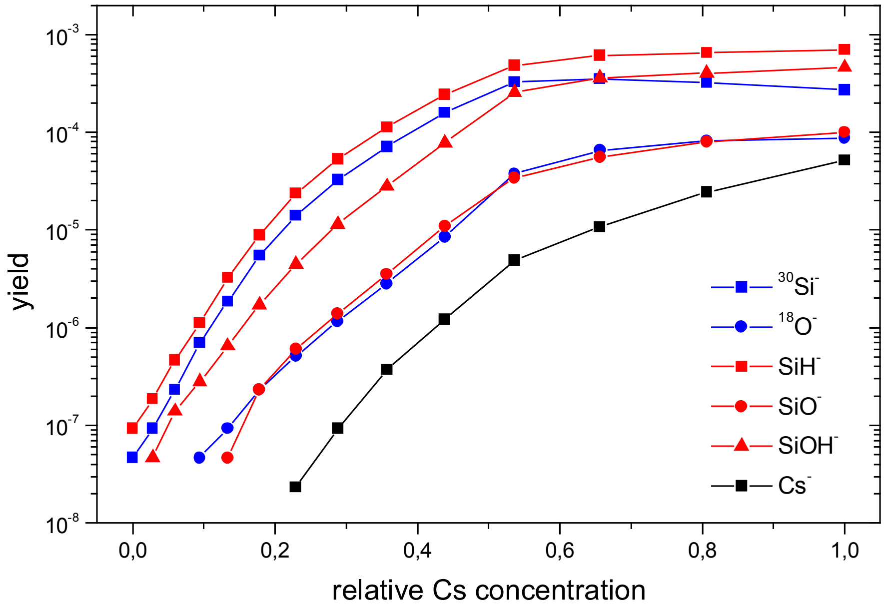

Fig. 21: Secondary ion yield for different species measured on a Si wafer as a function of the relative Cs concentration. Sputtering: 350 eV Cs-Xe co-sputtering, 45°. Analysis: 15 keV Ga.

But for the detection of MCs^+ cluster ions in positive mode, the situation is completely different. A similar experiment as the one shown above has been conducted to measure the MCs^+ yield as a function of the relative Cs concentration (Fig. 22). As can be seen easily, the yield increases sharply and reaches a maximum below 20 % relative Cs concentration. Although the energy in this experiment was rather high (500 eV), the amount of Cs which is present at the surface if a pure Cs beam is used is more than 5 times larger than the optimum amount. The difference in $SiCs^+$ yield between these two concentrations is about a factor of 40.

Fig. 22 shows also the yield for Si^+ which decreases over the whole range of Cs concentrations by about a factor of 5. Two effects play a role in this variation. The partial sputter yield of silicon linearly decreases with increasing Cs coverage by about 30 % (also measured by [121]). Secondly, the probability for a Si^+ ion leaving the surface to be re-neutralized due to the lowered work function increases exponentially with the amount of Cs present. The latter is the more pronounced effect, leading to a nearly exponential decrease of the Si^+ yield with Cs concentration.

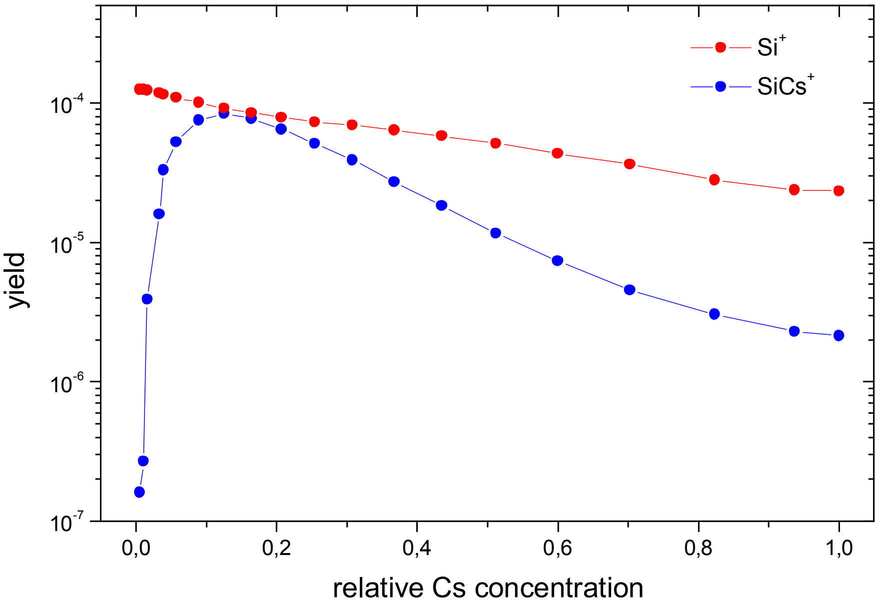

Fig. 22: Positive ion yields from a Si wafer under Cs-Xe bombardment as a function of the relative Cs concentration. Sputtering: 500 eV Cs-Xe co-sputtering, 45°. Analysis: 15 keV Ga.

With GaAs instead of Si, the same experiment gives similar results, displayed on the left hand side of Fig. 23. Again, the MCs$^+$ cluster yield goes through a maximum after a steep increase at a low Cs concentration and then decays again, this time only by a factor of three. The Cs signal behaves much the same, but with a shifted maximum and a stronger decrease towards high Cs concentrations. Both, the higher value of the optimum Cs concentration of the MCs$^+$ clusters compared to Si and the less pronounced decrease for pure Cs sputtering can be explained by the fact that the sputter yield for GaAs is much higher than for Si. This keeps the Cs concentration lower at the same bombardment conditions. For this matrix, the detrimental effect of a Cs overload are less pronounced at 500 eV bombardment, but principally the same.

Usually, the MCs$^+$ cluster intensity is normalized to the Cs$^+$ intensity and then quantified using an RSF. As discussed in 2.2.3, this expresses the assumption that the MCs$^+$ yield is proportional to the sputter yield of species M. In order to test this theory, the right part of Fig. 23 shows different yield ratios of the data from GaAs. For all relative Cs concentrations, the sputter yield of Cs is approximately the same and varies only by about 50 % over the whole range of concentrations.

In spite of this, the ratio of the MCs$^+$ cluster yields and the Cs$^+$ yield varies over several orders of magnitude. The strongest variation occurs for Cs concentrations lower than the optimum for Cs$^+$, but for higher values the variation is still about a factor of 3 – 4 for GaCs$^+$ and AsCs$^+$, respectively. One reason for this strong variation is the fact that the optimum Cs$^+$ yield is reached at a higher Cs concentration than the optimum MCs$^+$ yield. One possible explanation: At low Cs concentrations, the Cs$^+$ is already available for cluster formation, and the sputter yield for the matrix species is still high. At higher Cs concentration, the excess Cs$^+$ available is useful for the cluster formation, but there is less neutral Ga and As available, because the sputter yield for these species decreases due to the covering of the surface with Cs. Additionally, the fraction being emitted as negative secondary ions increases. Whether or not the ionized fraction is high enough to really reduce the amount of neutral Ga and As emitted is in question. Here, investigations of the MCs$_2^+$ clusters may reveal some information in the future.

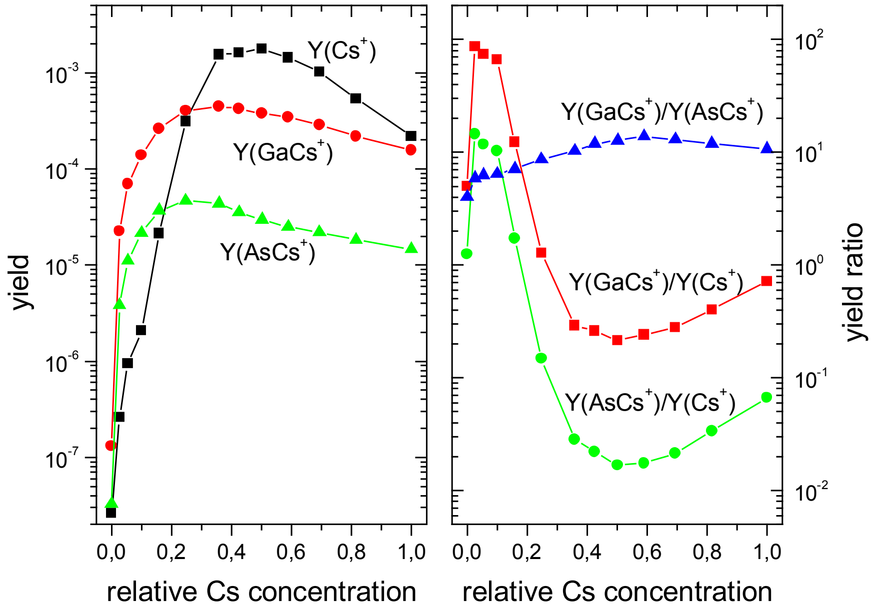

Fig. 23: ***left***: **Positive ion yields from a GaAs wafer under Cs-Xe co-sputtering as a function of the relative Cs concentration. Sputtering: 500 eV Cs-Xe co-sputtering, 45°. Analysis: 15 keV Ga.** ***right***: **Yield ratios for different species vs. the relative Cs concentration.**

Probably there is another, yet unknown effect causing yield ratio variations of this magnitude at relative Cs concentrations below the optimum for Cs$^+$ formation, which is not compatible with the recombination model, or in other words, the recombination model is not valid for all Cs concentrations.

For higher Cs concentrations, the variation is much lower, but still evident. Except for Cs concentrations around the optimum for Cs$^+$, small variations in the Cs concentration, e. g. due to sputter yield variations, lead to strong variations in the yield ratio and consequently in the RSF. An explanation for this variation is again not consistent with the recombination model; although less neutral Ga and As is available due to increased Cs coverage and higher emission of negative secondary ions, the normalized yield of the MCs$^+$ clusters increases. This could be explained if the Cs$^+$ emission is more strongly influenced by the low work function and overcompensates the decreased number of neutral matrix atoms being sputtered.

Interesting is the comparatively low variation of the ratio of the GaCs$^+$ and AsCs$^+$ yields over the whole range of Cs concentrations, even at very low Cs coverage, while the absolute yields vary over orders of magnitude. This prompts an investigation of the formation of MCs$^+$ cluster ions in more detail, since they seem to still have the potential to be relatively insensitive to matrix variations. Unfortunately, the trust in the *simple* quantification of the MCs$^+$ cluster approach has to be restricted.

A practical application of the Cs-Xe co-sputtering is illustrated by Fig. 24, a depth profile of a 6 nm gate oxide with some per cent nitrogen distributed within the oxide layer. Profiled at 350 eV and 45° with pure Cs (Fig. 24 *left*)[25], the MCs$^+$ yields are very poor and react more on the changes in Cs concentration at the interface than on the stoichiometry.

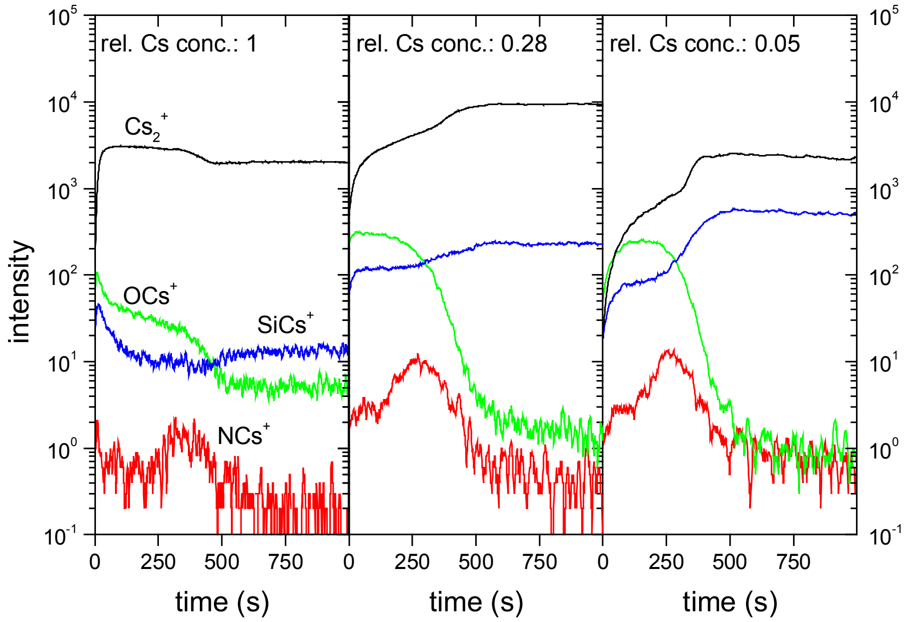

Fig. 24: Cs cluster profile of a 6 nm gate oxide at different relative Cs concentrations. With pure Cs sputtering (*left*), the intensities are very poor and do not reflect the stoichiometry at all. At lower relative Cs concentration (*middle, right*), the profile quality improves (see text). Sputtering: 350 eV Cs-Xe co-sputtering, 45°. Analysis: 15 keV Ga.

At reduced Cs concentration, the signals are much stronger and allow better quantification, although the best value for the Cs concentration has to be determined. From Fig. 23, it is obvious that at the maximum MCs$^+$ intensity, the variation of sensitivity with Cs concentration at interfaces is minimized. For this sample, the profile in the middle

---

[25] Note that the profile was measured before the large improvements in sputter current and high repetition rates were available, so the sputter time is unnecessarily long

is measured at optimized intensity, and the $SiCs^+$ signal does show the expected increase at the interface from SiO_2 to Si by a factor of 1.5.

At even lower Cs concentration, segregation of Cs in the oxide and variations of the Cs concentration at the interface lead to an artificial increase of the $SiCs^+$ signal at the interface of nearly one decade.

Cs-Xe co-sputtering permits the analysis of thin layers at very low energy and angles of incidence which do not cause roughening, with good sensitivity while using MCs^+ clusters for quantification. The accuracy of the quantification, however, has to be carefully revised as illustrated above. The applicability for thinner and more complex gate dielectrics has to be investigated in more detail in the future.

5.3 3D Micro Analysis

The term micro analysis refers to the three dimensional characterization of a sample volume. Lateral dimensions from 10 µm up to a few 100 µm and a depth of up to some µm specify this volume, and a technique which is to be used to analyze such a volume needs sufficient lateral and depth resolution.

Considering a relatively small volume of 10 x 10 μm^2 area and 1 µm depth, the number of atoms available for analysis is approximately $5{\cdot}10^{12}$. Assuming a medium useful secondary ion yield of 10^{-3}, this results in a number of detectable ions of $5{\cdot}10^9$. If the element of interest is present at a concentration of 0.1 %, $5{\cdot}10^6$ ions of this species can be detected, which would result in an average of 500 counts in a pixel of 100 nm size, if all counts over the total depth are integrated. If the volume is divided into 500 scans (according to a depth interval of 2 nm), only 1 count per pixel remains in each scan, which would hardly be sufficient to show the spatial distribution of the analyte with good dynamic range.

The only way to improve the statistics of a given set of data is to increase the size of the voxels[26] (e. g. from 100 x 100 x 2 nm^3 to 200 x 200 x 4 nm^3, resulting in an average of 8 counts per voxel), simultaneously reducing the sampling in all dimensions. This example illustrates the necessity to collect as many counts originating from the analyzed volume as possible, since the useful lateral and depth resolution (or voxel size) can be strongly limited by the amount of data collected. The adjustment of the matrix conditions by the low energy sputter beam for optimized ionization probability and the high transmission of the

---

[26] In two dimension, the smallest image unit is called *pixel*, in three dimension it is called *voxel*.

TOF analyzer are extremely helpful in this respect. One could even think of reducing the sputter beam energy to values that result in nearly no sputtering, optimizing the ionization probability while consuming the sample completely with the analysis beam.

One commercial instrument dedicated to the micro analysis and small area imaging is available at the moment [56, 57, 122], but all SIMS instruments have this option in principle, although it is limited to large volumes in the case of standard dynamic SIMS instruments due to the relatively large spot size of the ion gun. The single and dual beam instruments are compared in the following section, before the analytical results obtained in this work are discussed.

5.3.1 Dual Beam Approach for 3D Micro Analysis

Compared to single beam SIMS techniques, a number of advantages of the dual beam approach can be identified for the analysis of small volumes, originating from the use of two ion beams and mass separation by time-of-flight analysis:

1. *Lateral resolution of liquid metal ion gun*

   In the dual beam approach, the secondary ion generation and the sample erosion are decoupled. Therefore, the chemical effects of the analysis beam do not have an impact on the sensitivity, allowing the use of liquid metal ion guns for the high brightness and good lateral resolution without the need to compromise for the matrix optimization with respect to secondary ion formation.

   As already discussed above, the lateral resolution of the instrument used in this study is 100 – 200 nm, with high mass resolution possible at 250 nm spot size employing the “burst mode” [68]. If the area is large enough, also the bunched mode with higher intensity and better mass resolution can be applied, giving a spatial resolution of 1 – 5 µm.

2. *Optimization of matrix without compromise*

   The application of a low energy sputter source which does not need to meet any lateral resolution requirements gives a lot of flexibility in optimizing the matrix composition for best sensitivity. Matrix optimization plays a dominant role, since the amount of material available for analysis is very limited, making an effective secondary ion generation mandatory to achieve good sensitivity. With the dual beam approach, the sputter gun can be run at an energy and angle of incidence chosen for best depth resolution and sensitivity, not with the energy necessary to reach the lateral resolution.

3. *Short transient due to low energy reactive ions*

   Since the reactive ions originate from a low energy beam, the transient width can be very short – it is proportional to $E^{2/3}$ (cf. 2.1). A short transient allows the sensitive analysis of very shallow volumes and the inclusion of the outermost layers of the sample with the same sensitivity. Compared to the 15 keV beam of a single beam SIMS instrument for micro analysis, using a 250 eV beam results in a reduction of the transient width by about a factor of 15.

4. *Parallel detection: easy survey of unknown samples and retrospective analysis of unique samples*

   TOF-SIMS with its ability to detect all masses in parallel offers the advantage of using retrospective analysis to extract the maximum amount of information from one single experiment, which is especially helpful for unique samples or sample zones.

   But the parallel detection also increases the effective useful yield for samples of unknown composition. With a dynamic SIMS tool, the mass analyzer is a filter which has to be switched sequentially to the masses of interest, limiting the number of masses being detected and reducing the useful yield proportional to the number of masses which are recorded. Practically, only about 10 masses can be analyzed without the risk of reducing the sampling rate too much for a single mass, which would effectively limit the depth resolution. For some instruments, the use of multi-detector arrangement to some extent overcomes this limitation, but more than seven masses in parallel are still not feasible [56].

   These restraints mean that unknown samples can in many cases only be analyzed after a test run in which the interesting masses are identified and selected for the second measurement, increasing the actual measurement time on the instrument. With TOF-SIMS, retrospective analysis can be performed off-line and with much higher speed and flexibility than a second measurement.

5. *Better depth resolution*

   Obviously, the mixing of a single high energy beam limits the depth resolution to a larger extent than the combination of a low dose high energy analysis beam with a high dose low energy sputter beam, even if the sputter rate ratio in the dual beam mode becomes smaller than 10 (refer to section 5.1). In the worst case, the analysis beam limits the depth resolution to the same value as the high energy sputter beam in the single beam approach.

6. *Flexibility with respect to sensitivity, depth resolution and lateral resolution*

   By the choice of the sputter rate ratio, the analyst can influence the sensitivity via the fraction of material being removed by the analysis beam. Increased sensitivity at some point limits the depth resolution due to the mixing contribution of the analysis beam, so conditions can be selected to optimize both depth resolution and sensitivity according to the specific sample.

   Additionally, the mode and energy of the analysis beam can be chosen to give up some lateral resolution and gain depth resolution (by reducing the energy and therefore the mixing contribution) without changing the sensitivity.

   At a given sputter rate ratio (or sensitivity, respectively), the speed of erosion and therefore the measurement time can be very large, if a high lateral resolution is chosen. The intensity of the analysis gun limits the possible intensity of the sputter gun to keep the sputter rate ratio that is necessary for the sensitivity aimed at. In this case, reduced lateral resolution can increase the sample throughput, because the higher current of the analysis beam at larger spot size allows a faster sputtering at the same sputter rate ratio.

   These examples illustrate the flexibility that is offered by the decoupling of analysis and sputtering, and there are more examples where a specific mode is chosen to optimize a certain aspect of the experiment in a trade-off that would not be possible with a smaller number of independent parameters to choose from.

The six arguments show the advantages of the dual beam approach over the single beam techniques. Nevertheless, a number of applications exist where the single beam techniques are still more sensitive, especially if the sample is known very well and the number of masses being analyzed is very small.

An analytical example showing some of the advantages and demonstrating the performance of TOF-SIMS with the instrumental developments described in chapter 4 will be shown in the next section.

Before the experimental data are discussed, one remark concerning the display of 3D results; in most cases, the depth is in the order of several 100 nm, while the lateral extension of the analyzed volume is several 10 µm or larger. The aspect ratio is about 0.01, which is typically also the case for the ratio of depth resolution to lateral resolution.

The minimum useful voxel size results from this resolution limit, and it is therefore not cubic, but strongly compressed in vertical direction. To be able to resolve these voxels in printed images, they are stretched to appear approximately cubic, leading to an exaggeration of the depth by about a factor of 100, which should be kept in mind when visualizing or analyzing three dimensional SIMS data.

5.3.2 Applications of the Dual Beam Mode for 3D Micro Analysis

One example which is in generally well suited for 3D analysis using TOF-SIMS is a thin film transistor (TFT) of an active matrix liquid crystal display (LCD) [123]. These devices are located at each pixel of such a display and are utilized to switch the transmission of this pixel. Their thickness of several hundred nm requires high sputter currents available now with the low energy dual source column to keep the measurement time reasonable.

While the drain contacts of all TFTs in a display are connected, the gates of one column/row of TFTs and the source contacts of one row/column are connected to the driving circuits. To switch an individual pixel on, the respective source and gate line are switched. The whole column of transistors connected to this gate line is switched on, but only the one transistor connected to the active source line is active and switches the liquid crystal to transmission (Fig. 25).

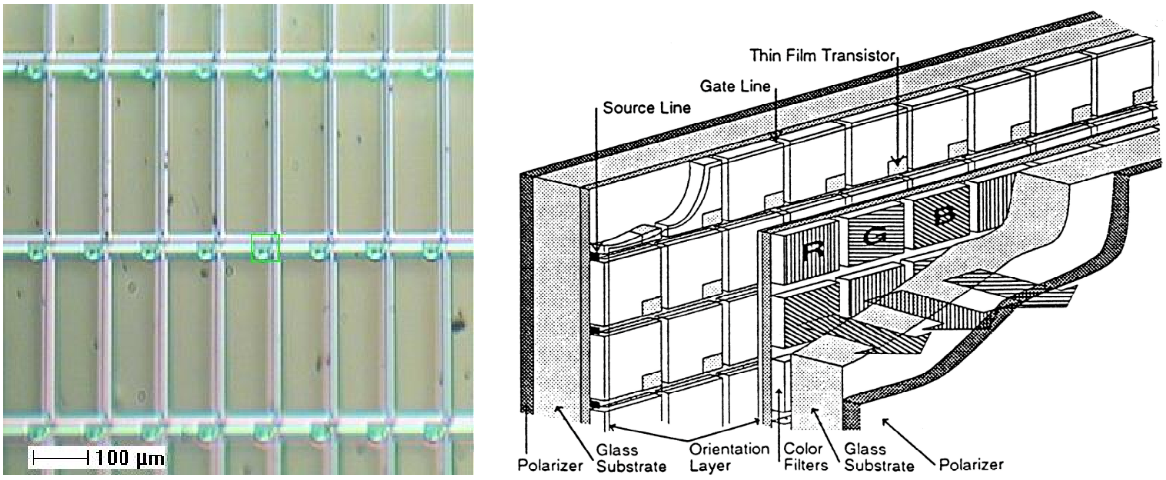

Fig. 25: Optical image of the TFT display within the instrument (*left*) and schematics of the TFT display (*right*, from [123]). The individual pixels can be seen in the optical image as small rectangles of about 110 x 330 µm^2. In the upper right corner of each pixel the transistors, which are only some 10 µm large, are located and marked with a green square of 50 µm size (in the center of the image).

For the experiments of this chapter, a commercially available TFT display was disassembled and the glass substrate of the transistors was cut into smaller pieces.

Hexane was used to wash off the liquid crystal solution and to remove organic material from the transistors.

On this sample, depth profiles with high lateral resolution were performed in order to investigate the possibilities and limitations of the technique. An overview over the structure gives Fig. 26, showing the transistor in the upper right corner of one pixel and parts of three neighboring pixels. The transparent electrodes forming the pixels itself are made of ITO (indium tin oxide) and can be identified in the InO^- image. In this image, the black areas show the electrical connections (source and gate lines).

In the upper right corner of the lower left pixel, the transistor itself is visible. It consists of two electrical connections (the source contact connected to the vertical line and the drain contact connected to the pixel electrode via a circular structure) and a buried gate electrode connected to the horizontal line that is not visible in this view. Between the source and drain electrodes, the active channel region is located.

A particle can be seen on one of the pixel electrodes. From the carbon distribution, it can be assumed to be an organic residue from the cleaning procedure prior to analysis, but it shows the capabilities of the technique for failure analysis in a production environment. Since the images have been collected during a depth profile and already contain the information integrated over approx. 1.27 µm of depth, this particle could also be identified if it were located within the structure.

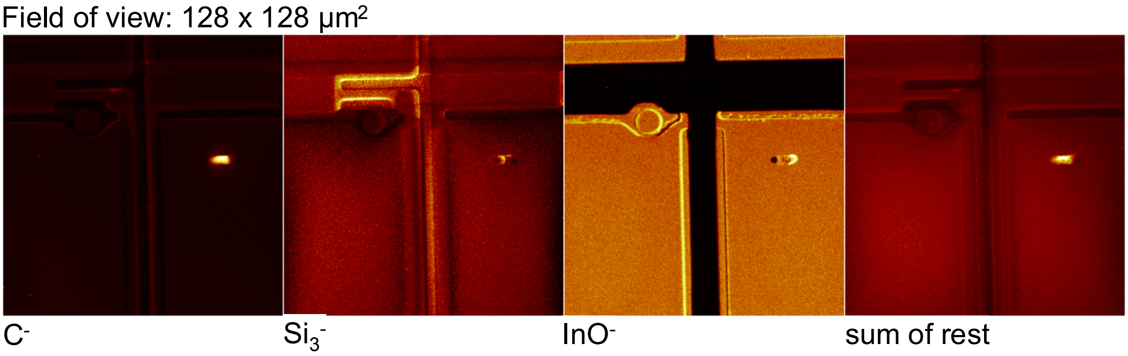

Fig. 26: Overview over the TFT (see text). Sputtering: 2 keV Cs, 300 x 300 µm², 45°. Analysis: 25 keV Ga, 128 x 128 µm².

The three dimensional structure of the transistor can be revealed by this analysis, which is illustrated with the following example. The Si_3^- images shows a bright rectangular area just at the source and drain contacts of the transistor. Additionally, a homogenous distribution of Si_3^- is visible, which is due to Si present at other locations (mainly in form of Si_xN_y as isolating material). Since these data were acquired with nominal mass resolution, hydrocarbons and elements cannot be distinguished, but under the Cs bombardment applied, hydrocarbons are removed very quickly. The same distribution with slightly less contrast is visible at mass 56 u (Si_2^-), while the distribution of Si^- is much more homogenous, because it is present in Si_xN_y nearly everywhere in the device and the Si density only varies by about a factor of two. The contrast of the Si_x^- signals is mainly due to a matrix effect of the silicon. Their emission probability is dependent on the number density of Si. The higher the number of atoms per cluster, the more sensitive the generation of this cluster is to the number of neighboring Si atoms in the bulk.

In Fig. 27, the upper left image shows the Si_3^- image in the usual way accumulated over many individual scans at different depth. The lower two images are vertical sections through the stack of images and have been calculated by 'cutting' the stack along the green lines. They can be visualized as vertical sections through the analyzed volume. As already mentioned in 5.3.1, the extension of these sections in z direction is typically one to two orders of magnitude smaller than in x and y direction, although they are often displayed as squares.

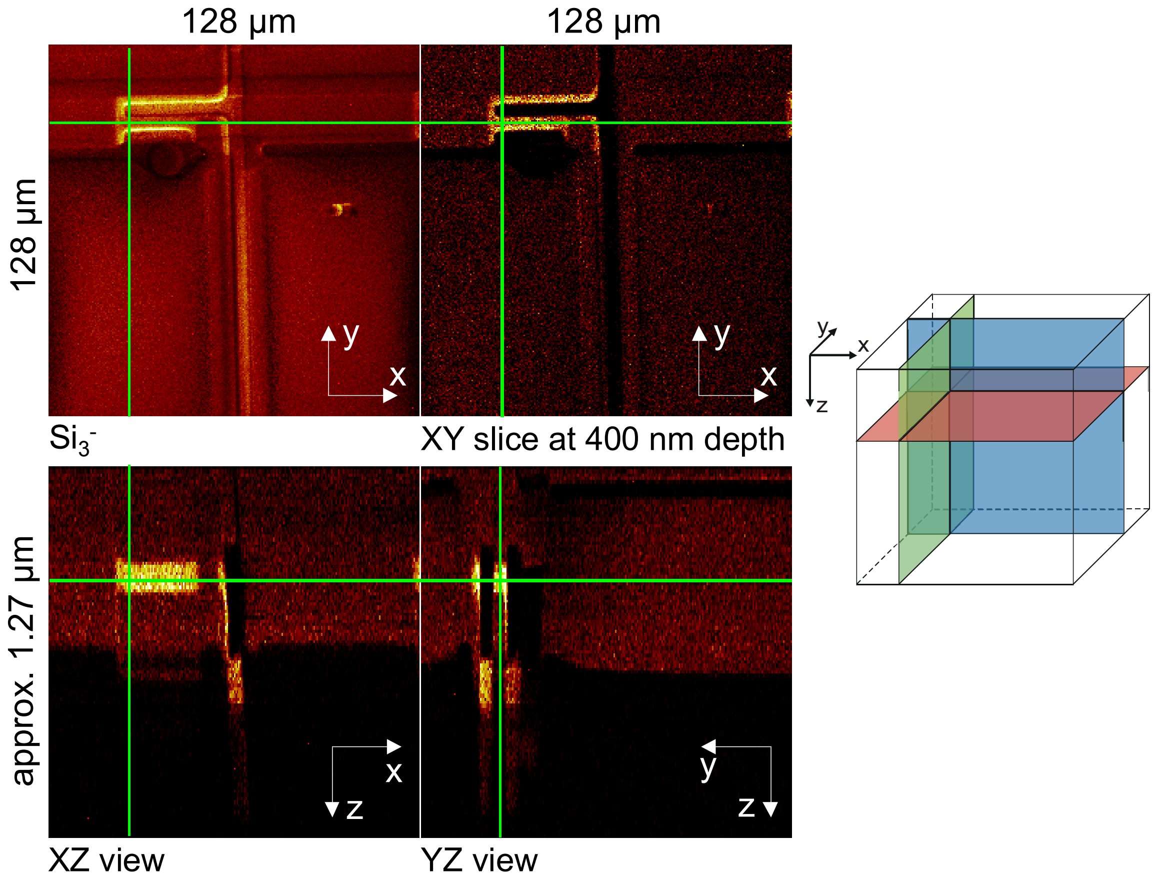
Si_3^-

XY slice at 400 nm depth

XZ view

YZ view

Fig. 27: **3D reconstruction of the TFT using the Si_3^- image stack. The data is taken from the experiment shown in Fig. 26. The green lines indicate the position of the vertical sections (XZ and YZ) and the depth where the XY slice is located.**

Since the material covering the Si layer under the Ta lines is thicker than between the contacts, the time necessary to sputter to the Si layer is longer, causing the impression of separated Si layers at different depths. In order to correct for this topography effect, the initial surface topography needs to be known.

Another effect causing local shifts in the z direction are different sputter rates. One would have to apply a pixel-by-pixel depth calibration to correct for this, which at this state is impossible due to the high complexity of the device and the lack of knowledge about the sputter yields of the different materials.

From the location of the Si layer, it is clear that this region must be the active channel of the transistor. From several XY slices at different (apparent) depths, the whole lateral distribution of the Si can be derived. It is also present under the vertical source line, but not below the horizontal gate line.

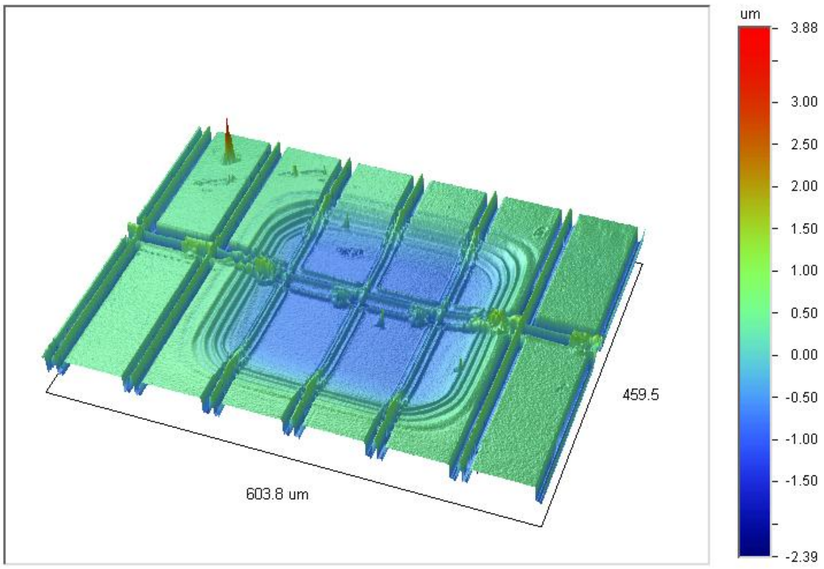

Fig. 28: Optical profilometer measurement of the TFT device. The initial topography is clearly visible, and some of the topographic features remain at the bottom of the sputter crater.

For the conditions applied during the analysis, a sputter rate ratio of ≈ 1400 is calculated, assuring that the depth resolution is solely determined by the sputter conditions. Nevertheless, the vertical sections through the analyzed volume show a limited depth resolution, and reconstructed profiles from some areas support this observation. The depth resolution is several times worse than the values one would expect from 2 keV Cs bombardment.

This illustrates that a number of other factors such as initial topography limit the depth resolution. Even if the area analyzed is reduced to 40 x 40 µm^2, the sputter rate ratio would be larger than 130, still in the range of moderate reduction in depth resolution.

The reconstruction of the Si_3^- intensity shown here demonstrates the ability to resolve the structure of an unknown device, although some knowledge about the principles of the structure design is useful. With some other masses – especially the metals – it would be easy to use the three dimensional data for reverse engineering of the TFT structure. For quality control, organic and inorganic particles, only a few µm large, can be detected and analyzed.

The possibilities of the new sputter source and the knowledge about the mixing contribution of the analysis beam makes the application of 3D micro analysis for devices on the µm depth scale feasible in a reasonable measurement time.

Compared to magnetic sector of quadrupole instruments using a mass filter, the parallel detection increases the useful detection sensitivity proportional to the number of masses that are found, often 20 to 50 for such complex samples.

6 Summary and Outlook

TOF-SIMS is very successfully applied both as an analytical technique (e. g. depth profiling of thin layers, molecular imaging of surfaces) and as a tool for fundamental investigations (e. g. atomic mixing, secondary ion formation). Nevertheless, instrumental restraints and insufficient performance still limit the technique in some cases.

In depth profiling, high sputter currents at lower beam energy, extremely stable ion sources, optimized secondary ion yields and high repetition rates are necessary, while the imaging of molecular species requires polyatomic primary ions with high lateral resolution. For fundamental studies on the secondary ion formation, the surface chemistry (e. g. the Cs surface concentration) has to be controlled independently from other experimental parameters, and for investigation of the atomic mixing in TOF-SIMS depth profiling, variation of the sputter and analysis beam energy and species at a large range of current density ratios has to be possible.

Improvements in the analytical application and of the possibilities for fundamental research can be realized by the same instrumental developments. Resulting from this work, several new instrumental features for TOF-SIMS are now available, each of them satisfying several of the demands mentioned above in one way or the other.

The sputter energy regime has been extended to smaller energies with the new low energy sputter gun. Energies down to 200 eV are now available, while at higher energies up to 2 keV the sputter rates have been increased by nearly one order of magnitude. Both for ultra shallow profiling and for several µm thick samples the sputter beam can be optimized with respect to energy and speed of erosion.

Higher repetition rates are not only helpful for depth profiling to increase the dynamic range, but also in imaging. Especially if only low masses are of interest (elemental mapping), the data rates are considerably higher, allowing a shorter acquisition time for the same data quality or improved counting statistics in the images with a reasonable duration of the experiment.

Both developments, the low energy sputter source and the capability for high repetition rates, can be considered as especially useful when combined. They allow the measurement of depth profiles a factor of five faster than previously possible, while keeping the dynamic range constant. Alternatively, the dynamic range can be increased by a factor of five while keeping the measurement time unchanged. In the first case, the sputter rate can be increased because the sputter gun is now capable of delivering enough current. The erosion can keep up with the analysis, which is performed by the analysis gun operated at the higher rate. In the second case, the sputter rate is kept constant, while the analysis gun collects five times more data at the same time, improving the counting statistics. Besides this, the sputter energy can often be reduced to improve the depth resolution.

These possibilities further decrease or even overcome the gap between TOF-SIMS and the classical dynamic SIMS instruments (magnetic sector and quadrupole instruments) with respect to detection limits for shallow and ultra-shallow implants. Nowadays, TOF-SIMS can be regarded as a mature depth profiling technique, still requiring development for some applications (e. g. high energy implants), but also offering a number of superior features for non-standard tasks (e. g. survey of unknown samples, complex multilayer systems).

The other two instrumental topics, the method of Cs-Xe co-sputtering and the Au cluster ion source, allow the study of the ion formation process, and both of them have also strong analytical impact. Cs-Xe co-sputtering is the only way of adjusting the Cs concentration during Cs sputtering without any influence on the other experimental parameters. This makes it ideally suited for studies of the formation process of negative secondary ions from cesium covered surfaces and of MCs^+ clusters. One application arising from this is the optimization of MCs^+ cluster emission at very low sputter energy, improving the quantitative analysis of ultra-thin layers.

Extensive studies on the molecular emission of organic molecules will be possible with the Au cluster ion source, but have not been addressed in this work. These studies and the application of the source to the analysis of materials like polymers, pharmaceuticals, or biological tissue will be the main exploitation of the Au source, but it is also beneficial for studies on atomic mixing as performed in this work.

In addition to the instrumental developments, which represent the first part of results obtained in this work (chapter 4), the analytical and fundamental results which were obtained employing the new possibilities are covered in chapter 5. While the studies on the mixing contribution of the analysis beam in dual beam mode and the emission of MCs^+

clusters at varying Cs concentration are fundamentally orientated, the very profile of a very shallow implant with extended dynamic range and the work on 3D micro analysis show the new capabilities with respect to analytical application.

Since TOF-SIMS is, especially with the new ion guns and the high repetition rates, becoming a widely used depth profiling technique, there is really a need to understand the specific differences between dual beam and classical – single beam – depth profiling in SIMS. The mixing contribution of the analysis beam is one of those aspects and has been studied under different bombarding conditions. It has become evident that the mixing of both the sputter and the analysis beam add to a total atomic mixing, and that for most current applications the mixing of the analysis beam can be ignored. Over a wide range of bombardment conditions, the negative influence of the high energy analysis beam rises slowly. Only in some cases it becomes noticeable, and this work also gives some hints how to avoid detrimental effects in analytical applications by choosing the bombardment conditions appropriately or at least predict the magnitude of the additional atomic mixing.

Some work will have to be done in order to forecast the sputter rate ratio at which the mixing of the analysis beam for a given target material becomes significant. The theoretical understanding together with some more experimental work on different sample systems will give us a comprehensive picture in the future.

The second basic investigation in this work addresses the special case of ion formation from surfaces with a Cs overlayer. Using the new Cs-Xe co-sputtering technique, it once again confirms the predictions of the electron tunneling model with respect to the negative ion formation and the formation probability as a function of the Cs coverage. As a result, it becomes evident that in negative SIMS depth profiling a surplus Cs at the surface does not affect the ion formation even at the lowest possible sputter energies. In some cases, the reduction of the sputter yield caused by the covering Cs layer may be worth to be avoided by reducing the Cs surface concentration. Also, in a few cases, the segregation of excess Cs requires a reduction of the amount of Cs in order to avoid artifacts.

For MCs^+ cluster ions however, the strong decrease in the formation probability at low sputter energies can be avoided by adding an experimental parameter, the Cs fraction of the sputter beam, to optimize the profile conditions. Effectively, the formation probability can be increased by up to a factor of 10, or even more in special cases.

The ion formation mechanisms can be empirically described, but they are not understood on a microscopic scale. Experiments focussing on some details of the ion formation are likely to reveal refinements of the electron tunneling and recombination model, and the Cs-Xe co-sputtering may be one way of experimental realization. Here, the differentiation between the sputtering and ionization processes, which can be ideally explored with SNMS, should be one aspect of further work.

From the application point of view, more experience with the variation of the Cs surface concentration is necessary to make the new approach a routinely applied technique. But the demand for shallower profiles of more complex layer systems in several technological fields and the lack of alternatives to SIMS suggest that it will be worth to continue in this direction.

In the final chapter, an example for the possibilities of TOF-SIMS depth profiling in combination with high lateral resolution is presented. Making use of the technical improvements achieved in this work, a thin film transistor (TFT) is analyzed and the power of the 3D micro analysis is shown. The prerequisites for the broad application are met by modern instrumentation; now the users of TOF-SIMS have to employ the 3D analysis to their problems and start to gain experiences. If this approach is successful from an application point of view, a number of further developments, especially in the data treatment to correct for initial surface topography and locally different sputter rates, can further improve the usability.

7 Acknowledgement

I gratefully acknowledge

- Prof. Benninghoven and ION-TOF for giving me the opportunity to complete this work in an industrial environment that gave me excellent possibilities with respect to equipment and resources.

- Ewald Niehuis for sparing the time for discussion, offering scientific advice and supporting this work in all of its stages.

- TASCON for analytical support and sharing experiences with all kinds of analytical questions.

- All of the ION-TOF staff including all departments – especially mechanical assembly, software and electronics – for advice, assistance and support in solving all the small (and large) problems I came across.

- Rudolf Möllers, Felix Kollmer, Peter Hörster, Thomas Heller and Martin Krehl for intense collaboration especially during the instrumental development.

- J. Bennett (SEMATECH) and J. v. Berkum (Philips) for providing very well defined model samples that enabled the fundamental studies on mixing of the analysis beam.

- Nicola for everything.

8 References

[1] A. Benninghoven, F. G. Rüdenauer, H. W. Werner: *Secondary ion mass spectrometry - basic concepts, instrumental aspects, applications and trends*. Elektor-Verlag, Chichester, New York, Weinheim (1987).

[2] J. C. Vickerman, D. Briggs: *TOF-SIMS surface analysis by mass spectrometry*. Surface Spectra/IM Publications (2001).

[3] H. Gnaser: *Low-energy ion irradiation of solid surfaces*. Springer tracts in modern physics, Springer (1999).

[4] S. Hofmann: Compositional depth profiling by sputtering. *Progr. Surf. Sci.* **36**, 35 (1991).

[5] S. Hofmann: Sputter depth profile analysis of interfaces. *Rep. Progr. Phys.*, **61**, 827 (1998).

[6] P. C. Zalm: Ultra shallow doping profiling with SIMS. *Rep. Progr. Phys.*, **58**, 1321 (1995).

[7] N. Matsunami, Y. Yamamura, Y. Itikawa, N. Itoh, Y. Kazumata, S. Miyagawa, K. Morita, R. Shimizu, H. Tawara: Energy dependence of the ion-induced sputtering yields of monatomic solids. *Atomic data and nuclear data tables* **31**, 1, 1 – 80 (1984).

[8] Y. Yamamura, H. Tawara: Energy dependence of ion-induced sputtering yields from monatomic solids at normal incidence. *Atomic data and nuclear data tables* **62**, 2, 149 – 253 (1984).

[9] C. Garcia-Rosales, W. Eckstein, J. Roth: Revised formulae for sputtering data. *J. Nucl. Mater.* **218**, 8 (1994).

[10] Y. Yamamura, Y. Itikawa, N. Itoh: *Angular dependence of sputtering yields of monatomic solids*. Institute of plasma physics, Nagoya University, Japan (1983).

[11] H. H. Anderson, H. L. Bay: Sputtering yield measurements. In: R. Behrisch (Ed.): *Sputtering by particle bombardment I. Physical sputtering of single-element solids.* Springer (1981).

[12] C. F. McConville, S. H. Al-Harthi, M. G. Dowsett, F. S. Gard, T. J. Ormsby, B. Guzman, T. C. Q. Noakes, P. Bailey: Determination of the erosion rate in the transient region of an ultralow energy secondary ion mass spectrometry profile using medium energy ion scattering. *J. Vac. Sci. Technol.* **B20**, 4, 1690 (2002).

[13] Z. X. Jiang, P. F. A. Alkemade: Erosion rate change and surface roughening in Si during oblique O_2 bombardment with oxygen flooding. In: G. Gillen, R. Lareau, J. Bennett, F. A. Stevie (Eds.): *Secondary ion mass spectrometry XI*, Wiley (1998).

[14] M. R. Bradley, J. M. E. Harper: Theory of ripple topography induced by ion bombardment. *J. Vac. Sci. Technol* **A6**, 4, 2390 (1987).

[15] A. Zalar: Improved depth resolution by sample rotation during Auger electron spectroscopy depth profiling. *Thin solid films* **124**, 223 (1984).

[16] K. Iltgen: *Application of time-of-flight secondary ion mass spectrometry (TOF-SIMS) for high performance depth profiling of semiconductor materials*. Thesis, Münster, Germany (1997).

[17] K. Wittmaack: Sputtering yield changes, surface movement and apparent profile shifts in SIMS depth analyses of silicon using oxygen primary ions. *Surf. Interf. Anal.* **24**, 389 (1996).

[18] M. L. Yu: Charged and excited states of sputtered atoms. In: R. Behrisch, K. Wittmaack (Eds.): *Sputtering by particle bombardment III.* Springer (1991).

[19] M. L. Yu, N. D. Lang: Mechanisms of atomic ion emission during sputtering. *Nucl. Instrum. Methods* **B14**, 403 (1986).

[20] M. L. Yu: Work-function dependence of negative-ion production during sputtering. *Phys. Rev. Lett.* **40**, 9, 574 (1978).

[21] M. L. Yu, N. D. Lang: Direct evidence of electron tunneling in the ionization of sputtered atoms. *Phys. Rev. Lett.* **50**, 2, 127 (1983).

[22] M. L. Yu: Anomalous coverage dependence of secondary-ion emission from overlayers. *Phys. Rev.* **B29**, 4, 2311 (1983).

[23] H. Gnaser: Ion-yield and work function changes during transient cesium concentration. In: G. Gillen, R. Lareau, J. Bennett, F. A. Stevie (Eds.): *Secondary ion mass spectrometry XI*, Wiley (1998).

[24] G. Slodzian: Some problems encountered in secondary ion emission applied to elementary analysis. *Surf. Sci.* **48**, 161 (1975).

[25] P. Williams: The sputtering process and sputtered ion emission. *Surf. Sci.* **90**, 588 (1979).

[26] C. J. Vriezema, K. T. F. Janssen, P. R. Boudewijn: Field-induced segregation effects during secondary-ion mass spectrometry depth profiling of Cu and Na implanted in silicon. *Appl. Phys. Lett.* **54**, 20, 1988 (1989).

[27] J. Giber, L. Z. Mezey, D. Marton: The influence of oxygen on the segregation state of metal/oxygen and Si/SiO2 interfaces. In: A. Benninghoven (Ed.): *Secondary ion mass spectrometry VI*, Elektor-Verlag/Wiley (1987).

[28] J. J. Vajo: Effects of sample cooling on depth profiling of Na in SiO_2 thin films. *Surf. Interf. Anal.* **25**, 295 (1997).

[29] J. E. Ortega, E. M. Oellig, J. Ferron, R. Miranda: Cs and O adsorption on Si(100) 2x1: A model system for promoted oxidation of semiconductors. *Phys. Rev.* **B36**, 11, 6213 (1987).

[30] H. A. Storms, K. F. Brown, J. D. Stein: Evaluation of a cesium positive ion source for secondary ion mass spectrometry. *Anal. Chem.* **49**, 13, 2023 (1977).

[31] M. A. Ray, J. E. Baxter, C. M. Loxton, J. E. Greene: Quantitative analysis and depth profiling of rare gases in solids by secondary-ion mass spectrometry: Detection of $(CsR)^+$ molecular ions (R = rare gas). *J. Vac. Sci. Technol.* **A6**, 1, 44 (1988).

[32] Y. Gao: A new secondary ion mass spectrometry technique for III-V semiconductor compounds using the molecular ions CsM^+. *J. Appl. Phys.* **64**, 7, 3760 (1988).

[33] C. W. Magee, W. L. Harrington, E. M. Botnick: On the use of CsX^+ cluster ions for major element depth profiling in secondary ion mass spectrometry. *Intern. J. Mass Spectrom. Ion Proc.* **103**, 45 (1990).

[34] K. Iltgen, O. Brox, A. Benninghoven, E. Niehuis: Ultra shallow depth profiling by TOF-SIMS: Investigation of the transient region. In: G. Gillen, R. Lareau, J. Bennett, F. A. Stevie (Eds.): *Secondary ion mass spectrometry XI*, Wiley (1998).

[35] K. Wittmaack: Concentration-depth calibration and bombardment-induced impurity relocation in SIMS depth profiling of shallow through-oxide implantation distributions: a procedure for eliminating the matrix effect. *Surf. Interf. Anal.* **26**, 290 (1998).

[36] O. Brox, K. Iltgen, E. Niehuis, A. Benninghoven: Quantitative determination of oxide layer thickness and nitrogen profiles for Si gate oxides. In: A Benninghoven, P. Bertrand, H.-N. Migeon, H. W. Werner (Eds.): *Secondary ion mass spectrometry XII*, Elsevier (2000).

[37] H. De Witte: *Fundamental study of ion-substrate interactions with low energy reactive ions*. Thesis, Antwerp, Belgium (2001).

[38] S. Hofmann: Quantitative depth profiling in surface analysis: A review. *Surf. Interf. Anal.* **2**, 148 (1980).

[39] P. S. Ho, J. E. Lewis:Auger study of preferred sputtering on binary alloy surfaces. *Surf. Sci.* **55**, 335, (1976).

[40] S. Hofmann, W. Mader: Determination of the atomic mixing layer in sputter profiling of Ta/Si multilayers by TEM and AES. *Surf. Interf. Anal.* **15**, 794 (1990).

[41] S. Hofmann: Atomic mixing, surface roughness and information depth in high-resolution AES depth profiling of a GaAs/AlAs superlattice structure. *Surf. Interf. Anal.* **21**, 673 (1994).

[42] K. Wittmaack: Basic aspects of sputter depth profiling. In: D. Briggs, M. P. Seah: *Practical surface analysis. Volume 2: Ion and neutral spectroscopy*. Wiley (1996).

[43] B. T. Chait, K. G. Standing: A time-of-flight mass spectrometer for measurement of secondary ion mass spectra. *Int. J. Mass Spectrom. Ion Proc.* **40**, 185 (1981).

[44] A. Benninghoven: The history of static SIMS: A personal perspective. In: J. C. Vickerman, D. Briggs: *TOF-SIMS surface analysis by mass spectrometry*. Surface Spectra/IM Publications (2001).

[45] A. Benninghoven, B. Hagenhoff, E. Niehuis: Surface MS: Probing real-world samples. *Anal. Chem.* **65**, 630A (1993).

[46] A. Benninghoven: Chemical analysis of inorganic and organic surfaces and thin films by static time-of-flight secondary ion mass spectrometry (TOF-SIMS). *Angew. Chem. Int. Ed. Engl.* **33**, 1023 (1994).

[47] A. Benninghoven: Surface analysis by secondary ion mass spectrometry (SIMS). *Surf. Sci.* **299/300**, 246 (1994).

[48] S. G. Alikhanov: A new impulse technique for ion mass measurement. *Sov. Phys. JETP* **4**, 452 (1957).

[49] B. W. Schueler: Time-of-flight mass analyzers. In: J. C. Vickerman, D. Briggs: *TOF-SIMS surface analysis by mass spectrometry*. Surface Spectra/IM Publications (2001).

[50] M. L. Pacholski, N. Winograd: Imaging with mass spectrometry. *Chem. Rev.* **99**, 2977 (1999).

[51] A. Benninghoven: Gaede-Langmuir Lecture. Static SIMS applications – From single crystal oxidation to DNA sequencing. *J. Vac. Sci. Technol.* **A3**, 3, 451 (1985).

[52] K. Iltgen, A. Benninghoven, E. Niehuis: TOF-SIMS depth profiling with ultimate depth resolution. In: *Proceedings of the fourth international conference on measurement, characterization and modeling of ultra-shallow doping profiles in semiconductors. Research Triangle Park, NC, USA (1997).*

[53] K. Iltgen, A. Benninghoven, E. Niehuis: TOF-SIMS depth profiling with optimized depth resolution. In: G. Gillen, R. Lareau, J. Bennett, F. A. Stevie (Eds.): *Secondary ion mass spectrometry XI*, Wiley (1998).

[54] E. Niehuis, T. Grehl: Dual beam depth profiling. In: J. C. Vickerman, D. Briggs: *TOF-SIMS surface analysis by mass spectrometry*. Surface Spectra/IM Publications (2001).

[55] M. Schuhmacher, B. Rasser, E. De Chambost, F. Hillion, T. Mootz, H.-N. Migeon: Recent instrumental developments in magnetic sector SIMS. *Fresenius J. Anal. Chem.* **365**, 12 (1999).

[56] F. Hillion, B. Daigne, F. Girard, G. Slodzian, M. Schumacher: A new high performance instrument : The Cameca "Nanosims 50". In: A. Benninghoven, Y. Nihei, R. Shimizu, H. W. Werner (Eds.): *Secondary ion mass spectrometry IX*. Wiley (1993)

[57] F. Hillion, F. Horreard, F. J. Stadermann: Recent results and developments on the Cameca Nanosims 50. In: A Benninghoven, P. Bertrand, H.-N. Migeon, H. W. Werner (Eds.): *Secondary ion mass spectrometry XII*, Elsevier (2000).

[58] S Bryan, F. Reich: Optimizing Depth Resolution, Dynamic Range, and Data Density in TOF-SIMS Depth Profiling.*14th Annual workshop on secondary ion mass spectrometry*, Scottsdale, AZ, USA (2001).

[59] J. v. Berkum. *46th International symposium of the American Vacuum Society*, Baltimore, MD, USA (1998).

[60] T. Grehl, R. Möllers, E. Niehuis: Low energy dual beam depth profiling: Influence of the sputter- and analysis-beam parameters on profile performance using TOF-SIMS. *Appl. Surf. Sci.* **203 – 204**, 277 (2003).

[61] E. Niehuis, T. Heller, H. Feld, A. Benninghoven: Design and performance of a reflectron based time-of-flight secondary ion mass spectrometer with electrodynamic primary ion mass separation. *J. Vac. Sci. Technol A* **5**, 4, 1243 (1987).

[62] ION-TOF GmbH, Mendelstr. 11, 48149 Münster, Germany.

[63] E. Niehuis, T. Heller, G. Kampwerth, A. Benninghoven: A high resolution time-of-flight secondary ion mass spectrometer combined with laser postionization. In: A. Benninghoven (Ed.): *Secondary ion mass spectrometry VI*. Wiley (1987).

[64] L. W. Swanson: Liquid metal ion sources : Mechanism and applications. *Nucl. Instr. Meth. in Phys. Research*, **218**, 347 (1983).

[65] R. Hill: Primary ion systems. In: J. C. Vickerman, D. Briggs: *TOF-SIMS surface analysis by mass spectrometry*. Surface Spectra/IM Publications (2001).

[66] C. Bendel: *Hochauflösende Sekundärionen-Massenspektrometrie (TOF-SIMS) an Halbleiterstrukturen*. Thesis, Münster, Germany (1999).

[67] P. K. Dutt: Theory of 'ion-bunching' in relation to the development of an electrostatic time-of-flight mass spectrometer. *Nucl. Instr. Methods* **10**, 37 (1961).

[68] E. Niehuis, ION-TOF GmbH: Process for operating a time-of-flight secondary-ion mass spectrometer. *US Patent No. 5,633,495* (1997).

[69] I. S. Gilmore, M. P. Seah: Static SIMS: towards unfragmented mass spectra – the G-SIMS procedure. *Appl. Surf. Sci.* **161**, 465 (2000).

[70] F. Kötter, A. Benninghoven: Secondary ion emission from polymer surfaces under Ar^+, Xe^+ and SF_5^+ ion bombardment. *Appl. Surf. Sci.* **133**, 47 (1997).

[71] D. Stapel, O. Brox, A. Benninghoven: Secondary ion emission from arachidic acid LB-layers under Ar^+, Xe^+, Ga^+ and SF_5^+ primary ion bombardment. *Appl. Surf. Sci.* **140**, 156 (1999).

[72] *Mathematica 4.0*, Wolfram Research Inc., Champaign, IL, USA.

[73] D. A. Dahl: SIMION 3D 6.0. *43rd ASMS confrerence on mass specrometry and allied topics*, Atlanta, Ga, USA (1995).

[74] D. A. Dahl: SIMION 3D 7.0. Information at www.ineel.gov/env-energyscience/chemistry/simion-software.shtml.

[75] E. Niehuis: *Entwicklung und Anwendung von hochauflösenden Flugzeitspektrometern für die statische Sekundärionen-Massenspektrometrie*. Thesis, Münster, Germany (1988).

[76] J. Aubert, C. Lejeune, P. Tremelat: Beam emittance of the duoplasmatron as a function of the discharge modes. *Inst. Phys. Conf. Ser.* **38**, 6, 282 (1978).

[77] K. Volk, M. Sarstedt, H. Klein, A. Schempp: Energy spectra of ions and electrons of a duoplasmatron. *Rev. Sci. Instrum.* **61**, 1, 493 (1990).

[78] Osram Xenophot® HLX® 64634 halogen bulb with cold light reflector for photographic applications.

[79] M. L. Yu: Chemical enhancement effects in SIMS analysis. *Nucl. Instr. Methods B*, **15**, 151 (1986).

[80] Y. Kataoka, M. Shigeno, K. Wittmaack: Quantitative analysis of nitrogen in oxynitrides on silicon by MCs^+ secondary ion mass spectrometry? *J. Vac. Sci. Technol. B* **20**, 1, 441 (2001).

[81] T. Hoshi, M. Kudo: Ultra shallow depth profiling at silicon surface by means of time of flight SIMS and quadrupole SIMS. In: A Benninghoven, P. Bertrand, H.-N. Migeon, H. W. Werner (Eds.): *Secondary ion mass spectrometry XII*, Elsevier (2000).

[82] D. F. Reich, B. W. Schueler, J. Bennett: Characterization of ultra-thin oxide and oxynitride films. In: A Benninghoven, P. Bertrand, H.-N. Migeon, H. W. Werner (Eds.): *Secondary ion mass spectrometry XII*, Elsevier (2000).

[83] Y. Kataoka, M. Shigeno, K. Wittmaack: Characterization of ultra-thin oxynitrides by MCs^+ SIMS: Detailed evaluation of the dependence of ion yields and surface roughening on beam energy and impact angle. In: *Proceedings of the sixth international conference on measurement, characterization and modeling of ultra-shallow doping profiles in semiconductors*. Napa, Ca, USA (2001).

[84] P. A. W. van der Heide, J. Bennett: Transient effects noted during Cs^+ depth profile analysis of Si at high incidence angles. *Appl. Surf. Sci.* **203 – 204**, 306 (2003).

[85] Transient effects induced through ripple topography growth during Cs^+ depth profile analysis of Si at high incidence angles. *Appl. Surf. Sci.* **203 – 204**, 156 (2003).

[86] P. A. W. van der Heide: Transient effects in SIMS analysis of Si with Cs^+ at high incidence angles: Secondary ion yield variation. *Nucl. Instr. Meth.* **B194**, 489 (2002).

[87] T. Mootz, B. Rasser, S. Sudraud, E. Niehuis, T. Wirtz, W. Bieck, H.-N. Migeon: Cation Mass Spectrometer: An instrument dedicated to the analysis of MCs_x^+

clusters. Description of the instrument and preliminary results. In: A Benninghoven, P. Bertrand, H.-N. Migeon, H. W. Werner (Eds.): *Secondary ion mass spectrometry XII*, Elsevier (2000).

[88] E. Niehuis, T. Grehl: Dual beam SIMS depth profiling. In: A Benninghoven, P. Bertrand, H.-N. Migeon, H. W. Werner (Eds.): *Secondary ion mass spectrometry XII*, Elsevier (2000).

[89] T. Wirtz, H.-N. Migeon, H. Scherrer: Cation mass spectrometer: towards an otimisation of MCs_x^+ cluster analysis. *Appl Surf. Sci.* **203 – 204**, 189 (2003).

[90] T. Stephan, J. Zehnpfenning, A. Benninghoven: Correction of dead time effects in time-of-flight mass spectrometry. *J. Vac. Sci. Technol. A* **12**, 2, 405 (1994).

[91] M. Benguerba, A. Brunelle, S. Della-Negra, J. Depauw, H. Joret, Y. Le Beyec, M. G. Blain, E. A. Schweikert, G. J. Ben Assayag, P. Sudraud: Impact of slow gold clusters on various solids: nonlinear effects in secondary ion emission. *Nucl. Instr. Methods B* **62**, 8 (1991).

[92] A. V. Walker, N. Winograd: Prospects for imaging with TOF-SIMS using gold liquid metal ion sources. *Appl. Surf. Sci.* **9223**, 1-3 (2002).

[93] F. Kollmer, R. Möllers, D. Rading, B. Hagenhoff, E. Niehuis: Molecular imaging using atomic and molecular primary ions. *15th Annual workshop on secondary ion mass spectrometry*, Clearwater, FL, USA (2002).

[94] D. Stapel, M. Thiemann, B. Hagenhoff, A. Benninghoven: Secondary ion emission from LB-layers under molecular primary ion bombardment. In: A Benninghoven, P. Bertrand, H.-N. Migeon, H. W. Werner (Eds.): *Secondary ion mass spectrometry XII*, Elsevier (2000).

[95] K. D. Krantzman, R. Fenno, A. Mazingue, C. Garrick, B. J. Garrison, N. Winograd, A. Delcorte, Z. Postawa: Unraveling the puzzle: recent insights from the keV cluster bombardment of more realistic model systems of organic targets. *15th Annual workshop on secondary ion mass spectrometry*, Clearwater, FL, USA (2002).

[96] M. Medvedeva, I. Wojciechowski, B. J. Garrison: Effect of mass and incidence angle of keV energy polyatomic projectiles in silicon sputtering. *Surf. Sci.* **505**, 349 (2002).

[97] D. Rading, T. Grehl, C. Bendel, E. Niehuis, B. Hagenhoff: Basic Studies of Molecular Ion Emission under Ar, In and SF_5 Bombardment. *1st European workshop on secondary ion mass spectrometry*, Münster, Germany (1998).

[98] A. Benninghoven, D. Stapel, O. Brox, B. Burkhardt, C. Crone, M. Thiemann, H. A. Arlinghaus: Static SIMS with molecular primary ions. In: A Benninghoven, P. Bertrand, H.-N. Migeon, H. W. Werner (Eds.): *Secondary ion mass spectrometry XII*, Elsevier (2000).

[99] A. Bekkerman, B. Tsipinyuk, E. Kolodney: Negative Fullerene ion gun for SIMS applications. In: A Benninghoven, P. Bertrand, H.-N. Migeon, H. W. Werner (Eds.): *Secondary ion mass spectrometry XII*, Elsevier (2000).

[100] G. L. R. Mair: Liquid metal ion sources. In: J. Orloff (Ed.): *Handbook of charged particle optics*. CRC Press (1997).

[101] L. Bischoff, J. Teichert, S. Hausmann, T. Ganetsos, G. L. R. Mair: Investigation and optimization of the emission parameters of alloy liquid metal ion sources. *Nucl. Instr. Meth.* **B161**, 1128 (2000).

[102] International SEMATECH, 2706 Montopolis Drive; Austin, TX 78741.

[103] J. Bennett, A. C. Diebold, Round Robin Study of Ultra Shallow B Depth Profiling Experimental Conditions. In: A Benninghoven, P. Bertrand, H.-N. Migeon, H. W. Werner (Eds.): *Secondary ion mass spectrometry XII*, Elsevier (2000).

[104] Philips CFT, Prof. Holstlaan 4, 5656 AA Eindhoven, The Netherlands.

[105] KLA Tencor Alphastep 500 Surface Profiler.

[106] K. Iltgen, C. Bendel, A. Benninghoven, E. Niehuis: Optimized time-of-flight secondary ion mass spectroscopy depth profiling with a dual beam technique. *J. Vac. Sci. Technol. A* **15**, 3, 460 – 464 (1997).

[107] J. W. Burnett, M. J. Pellin, W. F. Callaway, D. M. Gruen, J. T. Jates, Jr: Ion dose dependence of the sputtering yield of Ru(0001) at very low ion fluences*. Phys. Rev. Lett.* **63**, 5, 562 (1989).

[108] G. Betz, M. J. Pellin, J. W. Burnett, D. M. Gruen: Low primary ion fluence dependence of single chrystal sputtering: a molecular dynamics study. *Nucl. Instrum. Methods B* **58**, 428 (1991).

[109] W. Eckstein, C. Garcia-Rosales, J. Roth, W. Ottenberger: *Sputtering Data. Report of the Max-Planck-Institut für Plasmaphysik (Report IPP 9/82)*. Garching/München, Germany (1993).

[110] SRIM 2000 (build 39). Available at www.srim.org

[111] J. F. Ziegler, J. P. Biersack, U. Littmark: *The stopping and range of ions in solids*. Pergamon Press (1985).

[112] K. Wittmaack, J. Griesche, H. J. Osten, S. B. Patel: In search of optimum conditions for the growth of sharp and shallow B-delta markers in Si by molecular beam epitaxy. *J. Vac. Sci. Technol.* **B18**, 1, 524 (2000).

[113] B. W. Schueler, D. F. Reich: Depth scale distortions in shallow implant secondary ion mass spectrometry profiles. *J. Vac. Sci. Technol.* **B18**, 1, 496 (2000).

[114] P. A. Ronsheim, K. L. Lee, S. B. Patel, M. Schuhmacher: A comparison of normal incidence versus oblique incidence with oxygen flood for sub 10 nm depth profiles of boron in silicon. In: G. Gillen, R. Lareau, J. Bennett, F. A. Stevie (Eds.): Secondary ion mass spectrometry XI, Wiley (1998).

[115] G. A. Cooke, T. J. Ormsby, M. G. Dowsett, C. Parry, A. Murrel, E. J. H. Collart: Use of two beam energies in secondary ion mass spectrometry analysis of shallow implants: resolution-matched profiling. *J. Vac. Sci. Technol.* **B18**, 1, 493 (2000).

[116] D. Krüger, K. Iltgen, B. Heinemann, R. Kurps, and A. Benninghoven: Ultrashallow secondary ion mass spectroscopy depth profiling of doping spikes and Si/SiGe/Si

heterostructures using different primary species. *J. Vac. Sci. Technol.* **B16**, 1, 292 (1998).

[117] K. Wittmaack: Towards the ultimate limit of depth resolution in sputter profiling: Beam induced chemical changes and the importance of sample quality. *Surf. Interf. Anal.* **21**, 323 (1994).

[118] I. Yamada, J. Matsuo, E. C. Jones: Cluster ion implantation for shallow junction formation. In: *Proceedings of the fourth international conference on measurement, characterization and modeling of ultra-shallow doping profiles in semiconductors. Research Triangle Park, NC, USA (1997).*

[119] K. Johannessen: Molecular dynamics simulation of sputtering from Au(100) with low-energy Xe ions and Xe dimers. *Nucl. Instr. Meth.* **B73**, 481 (1993).

[120] O. Brox: *Quantitative ultra shallow depth profiling time of flight secondary ion mass spectrometry*. Thesis, Münster, Germany (2000).

[121] J. Brison, L. Houssiau: A comparative study of cluster and elemental ion yields produced by co-sputtering various surfaces with Cs^+ and Xe^+ ions. *3rd European workshop on secondary ion mass spectrometry*, Münster, Germany (2002).

[122] Cameca S. A: Application note NanoSIMS 50. Available from www.cameca.fr (2002).

[123] W. C. O'Mara: *Liquid crystal flat panel displays – manufacturing science and technology*. Van Nostrand Reinhold, New York (1993).

Lebenslauf

Persönliche Daten

Name:	Thomas Grehl
Geburtsort:	Delmenhorst
Geburtsdatum:	6. September 1972
Familienstand:	ledig
Eltern	Paul und Hella Grehl, geb. Behrens

Schulbildung und Zivildienst

1979 –1983	Grundschule Marienschule, Delmenhorst
1983 –1985	Orientierungsstufe Schulzentrum Süd, Delmenhorst
1985 –1992	Gymnasium an der Max-Planck-Straße, Delmenhorst
19. Mai 1992	Allgemeine Hochschulreife
1992 –1993	Zivildienst

Hochschule

Oktober 1993	Beginn des Physikstudiums an der Westfälischen Wilhelms-Universität in Münster
März 1997	Beginn der Diplomarbeit (Prof. Dr. A. Benninghoven)
1. Oktober 1998	Hochschulabschluß: Diplom-Physiker
Oktober 1998	Beginn der Dissertation im Fach Experimentelle Physik am Physikalischen Institut der Westfälischen Wilhelms-Universität in Münster (Prof. Dr. A. Benninghoven)

Berufstätigkeit

seit Oktober 1998	ION-TOF GmbH, Münster, als Diplom-Physiker in Forschung und Entwicklung